DESIGNED CARBIDE-DERIVED CARBONS FOR AMMONIA FILTRATION

A Dissertation
Presented to
The Academic Faculty

by

Michael C. Mangarella

In Partial Fulfillment
of the Requirements for the Degree
Doctor of Philosophy in the
School of Chemical & Biomolecular Engineering

Georgia Institute of Technology
December 2015

DESIGNED CARBIDE-DERIVED CARBONS FOR AMMONIA FILTRATION

Approved by:

Dr. Krista S. Walton, Advisor
School of Chemical & Biomolecular Engineering
Georgia Institute of Technology

Dr. Christopher W. Jones
School of Chemical & Biomolecular Engineering
Georgia Institute of Technology

Dr. William J. Koros
School of Chemical & Biomolecular Engineering
Georgia Institute of Technology

Dr. Yulin Deng
School of Chemical & Biomolecular Engineering
Georgia Institute of Technology

Dr. Gleb N. Yushin
School of Material Science & Engineering
Georgia Institute of Technology

Date Approved: August, 4, 2015

To my Family

ACKNOWLEDGEMENTS

There are many people I would like to thank for their help over these past five years. First off, I greatly appreciate the guidance and support of my advisor, Dr. Krista Walton. She has been an incredible mentor over these past five years and truly a joy to work for.

I would like to thank my committee members, Dr. Deng, Dr. Jones, Dr. Koros, and Dr. Yushin for their valuable insight and suggestions that have furthered my work. I would especially like to thank all the members of the Walton Group, who have made even the most frustrating moments over these past five years still enjoyable. In particular, I would like to thank Karen Tulig, Guo Shiou Foo, and Sudhir Sharma for their many helpful suggestions. I would also like to thank Jessica Ewbank, Michael Dutzer, and Dr. Faisal Alamgir for their help with the XANES experiments seen in Chapter 3.

Most importantly, I would like to thank my family. Their endless encouragement has allowed me to achieve this important milestone in my life, and without their support this work would not have been possible.

TABLE OF CONTENTS

LIST OF TABLES

LIST OF FIGURES

SUMMARY

Porous carbon materials have long exhibited impressive performance for many catalytic and adsorptive applications, acting as catalyst supports, adsorbents, and filters. Their low cost as well as their high thermal and hydrodynamic stability allow them to be applicable in a wide variety of situations and industrial settings. Increased control over their physical and chemical properties has allowed these materials to be furthered tailored to specific applications. Carbide-derived carbons (CDCs) are a relatively new class of porous carbon materials with highly tailorable physical properties. As the name implies, these materials are produced through the selective extraction of a metal, or heteroatom, from a carbide precursor. This selective extraction is commonly accomplished via high temperature chlorination. The resulting pore space resembles the space previously occupied by the extracted heteroatom, and can be tuned through either careful choice of the carbide precursor or by adjusting the chlorination temperature. Research over the past few decades has focused on tailoring the physical properties of CDCs; this work builds on the knowledge gained from these studies by designing effective and efficient methods to include chemical specific active sites in CDC materials.

Among separations applications, the filtration of small and high vapor pressure gases greatly requires chemical specific active sites. The filtration of ammonia is a particular challenge, and also highly important due to its extreme toxicity, pervasive industrial use, and possible use as a chemical warfare agent. Current military filters composed of impregnated activated carbon, named Chemical Biological Nuclear and Radiological (CBRN) filters, provide inadequate protection against ammonia. The

applied research goal of this work was to greatly improve on current CBRN technology by designing state-of-the-art CDC filters that provide adequate respiratory protection.

To accomplish this goal, this work investigated novel methods to include metal nanoparticles within CDCs to increase sorbate-sorbent interactions. As the metal carbide precursor of a CDC already inherently contains a metal atom, a specific goal of this work was to develop novel techniques to retain a portion of these metal atoms as dispersed and tunable residual metal sites. This novel and facile synthesis method avoids some of the pitfalls of typical wet impregnation routes, namely pore blockage and poor dispersion of metal sites.

This work also investigated the addition of acidic functional groups to enhance interactions with ammonia. The high bulk porosity of CDCs allows ample space for acidic functional groups to provide targeted acid-base interactions with ammonia. In addition, the tunable pore size inherent to CDCs is ideal to systematically determine the ideal pore architecture for optimal utilization of these acid sites. Many factors, such as the type of acidic functional group and the effect of co-adsorbed water can play a factor in the adsorbent's dynamic adsorption capacity.

The overarching theme of this research was to make a direct impact on the CDC field by developing, optimizing, and validating methods to include targeted sorbate-sorbent interactions within carbide-derived carbons.

CHAPTER 1

INTRODUCTION

1.1 Need for Ammonia Filtration

Ammonia is one of the most important industrial gases. Over 195 million metric tons of ammonia are estimated to be produced annually, at a market value that exceeds US$100 billion. About 82% of produced ammonia is further converted into urea for use in fertilizer, while the rest serves essential roles within the pharmaceutical, cleaning product, refrigerant, and textile industries. However, this small, abundant gas is highly hazardous to human health. Ammonia exposure can quickly cause irritation, temporary blindness, and pulmonary edema. Both OSHA and NIOSH require limited ammonia exposure in the working environment at levels below 50 ppm and 25 ppm, respectively.[1] Effective respiratory protection is critical in any environment where ammonia exposure is possible. Ammonia is also one of the most pervasive industrial gases, creating a great need for adequate air purification methods across many industries. Besides its direct industrial use, ammonia is a key pollutant, and is most heavily emitted from the Concentrated Animal Feed Operations (CAFOs) for the cattle, swine, and poultry industries within the United States.[2] There is a growing concern over ammonia as a pollutant in CAFOs and its ability to affect animal health and growth, in addition to the well-being of contracted workers. Finally, ammonia is of particular concern to the defense industry. Due to its relative ease of acquisition, ammonia can be easily used as a chemical warfare agent (CWA).

1.2 Adsorption as a Separations Process

For these industrial and military applications, filtration of ammonia from air is most needed at ambient temperature and pressure, as well as under dry and humid conditions. For the respiratory protection of industrial workers and military personnel, this would be best accomplished through a small personal filtration device, which can quickly be outfitted in the field at the first detection of ammonia's pungent smell. An adsorptive filter would be an ideal solution. A packed filter canister is easy to use, can accommodate size and weight considerations, and adsorption is a very promising avenue for filtration of ammonia. Adsorption is the condensation of a gas, or adsorbate, on a solid surface, or adsorbent. Porous solids with accessible internal surface area have proven exceptionally useful in gas separation and purification. Gas adsorption is accomplished through two main mechanisms: physisorption, which results from attractive intermolecular forces between the adsorbate and adsorbent, and chemisorption, which involves a chemical reaction occurring between the adsorbate and a specific active site on the adsorbent framework generating new bonds between the two species. Common measures of porous materials are the accessible surface area, total pore volume, and pore size distribution. Pores can be classified into three main groups based on their diameter: micropores (< 2 nm), mesopores (2-50nm), and macropores (>50 nm).[3]

Many porous materials have been investigated for use as ammonia filters. Currently, within the defense industry, the filtration of ammonia is addressed through Chemical Biological Radiological Nuclear (CBRN) protection technology. CBRN filters are commonly made from activated carbon impregnated with a variety of metal and organic functional groups. Despite these active sites, CBRN filters have notoriously poor

performance against ammonia.[4] Due to its small size (3Å) and high vapor pressure, ammonia is difficult to adhere to the surface of an adsorbent without strong specific interactions or a reactive adsorption mechanism.[5] Though bulk porosity can play a role in the storage capacity of an adsorbent, current shortcomings in ammonia filtration technology are due to weak sorbate-sorbent interactions. Activated carbons without the addition of functional groups or metal impregnates have been shown to have poor ammonia adsorption, regardless of the specific surface area or total pore volume.[6, 7] In addition, assuming the density of adsorbed NH_3 is similar to its liquid density, only a total pore volume of 0.0856 cc g^{-1} is needed to reach the target loading of 6.9 mmol g^{-1} set by the Defense Threat Reduction Agency. The density of an adsorbate can be lower than that of the liquid density; nevertheless typical adsorbents often have total pore volumes greater than 1.0 cc g^{-1}.

To address this problem, current investigations have focused on developing novel adsorbent materials with targeted sorbate-sorbent interactions or reactive adsorption mechanisms. In addition, recent efforts have focused on predominately microporous materials. Often, small gases are more strongly adsorbed in pores with diameters similar to the kinetic diameter of the target gas. Materials such as impregnated and acidified activated carbon, graphite oxide, and metal organic frameworks (MOFs) have all been recently investigated as possible candidates.[6-24]

1.3 Ammonia Adsorbents and Current Limitations

The design of an adsorbent with strong specific sorbate-sorbent interactions must begin by understanding the unique chemical properties of the target adsorbate. For ammonia, it exhibits both Brønsted and Lewis basicity due to its lone pair of electrons.

Naturally, adsorbents with acidic sites are a good starting point for the controlled design of an ammonia adsorbent. Acid-base interactions between basic ammonia and acidic sites on the adsorbent surface are promising for retaining ammonia in porous materials. Many research groups have focused on the synthesis or impregnation of carbon adsorbents with acidic metal oxide nanoparticles.[7, 16, 21, 24] In addition to metal oxides, metal chlorides have also been investigated as possible synergistic impregnants. Many metal chlorides can interact with ammonia through the formation of stable metal ammine complexes.[14, 23, 25] Another interesting method is the acidification of activated carbon with nitric acid, sulfuric acid, peroxide, and other strong oxidative agents to graft acidic oxygen, nitrogen, and sulfur functional groups on the surface.[22, 26] Ammonia has been shown to interact with surface carboxylic acid groups, sulfonic groups, esters, and other acidic species grafted onto activated carbon. Graphite oxide, which is formed through the strong oxidative treatment of graphite, has shown very promising performance against ammonia.[15, 17-19, 27] After oxidative treatment, graphite oxide includes many acidic functional groups, such as carboxyl, hydroxyl, and epoxy groups, and has a layered structure inherited from its precursor, graphite. It is hypothesized that hydroxyl and epoxy groups are formed between graphene layers, stretching the basal spacing to between 6-11 Å in diameter, depending on environmental humidity.[28] Carboxylic groups are postulated to be located at the edges of the graphene layers. Ammonia is able to react or form hydrogen bonds with these surface groups, and can also be retained intercalated between the graphene layers.[15, 27]

Metal organic frameworks (MOFs) have also been investigated as ammonia filter materials.[8, 9, 29-31] MOFs are nanoporous, crystalline materials that consist of metal or

metal oxide nodes linked with an organic ligand to form 3-D porous networks. MOFs offer several key advantages that make them promising materials for ammonia removal. The organic ligand can be easily functionalized to tune adsorption interactions, the metal centers can be tailored towards target gases, metal nanoparticles can be impregnated to add active sorption sites, and the pore structure can be tuned through the length of the organic ligand to generate confinement effects for improved performance. Though tens of thousands of unique MOFs have been synthesized, material degradation in humid environments and the difficulty of scale-up has significantly limited the practical MOF candidates.[32-35] However, recent studies on the functionalization of UiO-66 and other water stable MOFs have shown increased performance against ammonia, mainly through the addition of carboxylic, amino, hydroxy and other acidic groups to the organic linker.[9] MOF and graphite oxide composites have also been investigated, as the oxygen functional groups present in graphite oxide provide coordination sites for the growth of MOF crystals.[10-12]

The co-adsorption of water is also an important consideration in ammonia adsorption. Ammonia has a high solubility in water and can form hydrogen bonds with co-adsorbed water films. As a result, water often plays a beneficial role in ammonia dynamic adsorption in humid conditions. Ammonia is converted to NH_4^+ and can more readily interact with surface species. In the presence of acidic functional groups, water is able to deprotonate carboxylic acids, allowing for the formation of an ammonia salt. In certain ultra-microporous structures, such as certain graphite oxides, water can hinder ammonia's accessibility to functional groups through competitive adsorption.[18]

1.4 Carbide-derived Carbons

Carbide-derived carbons (CDCs) are a relatively new class of carbon materials that have shown much promise for adsorptive applications.[36-39] As the name implies, CDCs are derived from the extraction of a heteroatom from a carbide precursor by various methods. Commonly, chlorination at high temperatures is used to convert the heteroatom to a gaseous chloride salt, which can diffuse out into the bulk gas phase, leaving behind an evolving porous carbon framework.[40] After complete extraction, CDCs have many attractive physical properties including tunable pore size, high microporosity, and high specific surface areas exceeding 2500 m^2 g^{-1}. The pore size of the resulting CDC resembles the space previously occupied by the heteroatom, allowing for a tuned microporous or mesoporous structure through careful choice of the carbide precursor. In Figure 1.1, it is clear that the original crystal structure of the carbide precursor can greatly influence the pore size distribution of the resulting CDC.

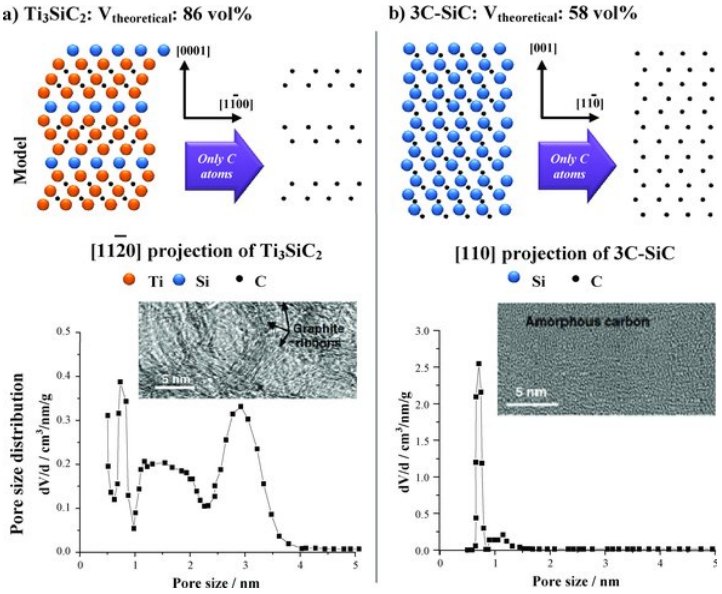

Figure 1.1 – Resulting pore spaces from Binary and Ternary Carbides, Figure adapted from [40]

The pore size can be tuned either through careful choice of the carbide precursor or by adjusting the chlorination temperature. Modification of the synthesis temperature can result in sub-angstrom control of pore size and narrow pore distributions.[36, 37, 41-47] Typically, microporous CDCs can be synthesized at low to moderate chlorination temperatures, with increased mesoporosity at higher chlorination temperatures.[42, 46, 47] The average pore size of CDCs derived from several carbide precursors increases with increasing chlorination temperature as seen in **Figure 1.2**. The carbon structure can also vary at different chlorination temperatures. At lower chlorination temperatures, many CDCs are comprised of disordered amorphous carbon. Whereas, higher chlorination temperatures allow greater mobility of the carbon, leading to increased graphitization and ordering. This in turn affects the porosity of the resulting CDC, as the distance between graphene sheets (3.4Å) leads to crystalline regions inaccessible to nitrogen or other probe molecules. The addition of a graphitization catalyst, accomplished by leeching a metal chloride into the carbide precursor, can also lead to increased graphitization.[48, 49] The formation of graphene, nano-diamond, or other crystalline or ordered structures has also been observed under certain synthesis conditions.[50]

An important secondary step in the CDC synthesis process is the annealment of the porous carbon. Commonly, trapped chlorine gas is present in CDCs after chlorination. Chlorine concentrations as high as 15 wt% have been observed and can result in substantial pore blockage.[51] These species are difficult to remove at high temperature, and need to be converted by H_2 or NH_3 treatment at high temperature to convert chlorine to HCl, which will subsequently desorb from the pore wall. This presence of physisorbed chlorine gas within CDCs is an important distinction in terms of porosity as well as

chemical interactions with guest molecules. Within this work, the distinction between unannealed CDCs, those containing chlorine species, and annealed CDCs, those subjected to an annealing treatment, will frequently be made.

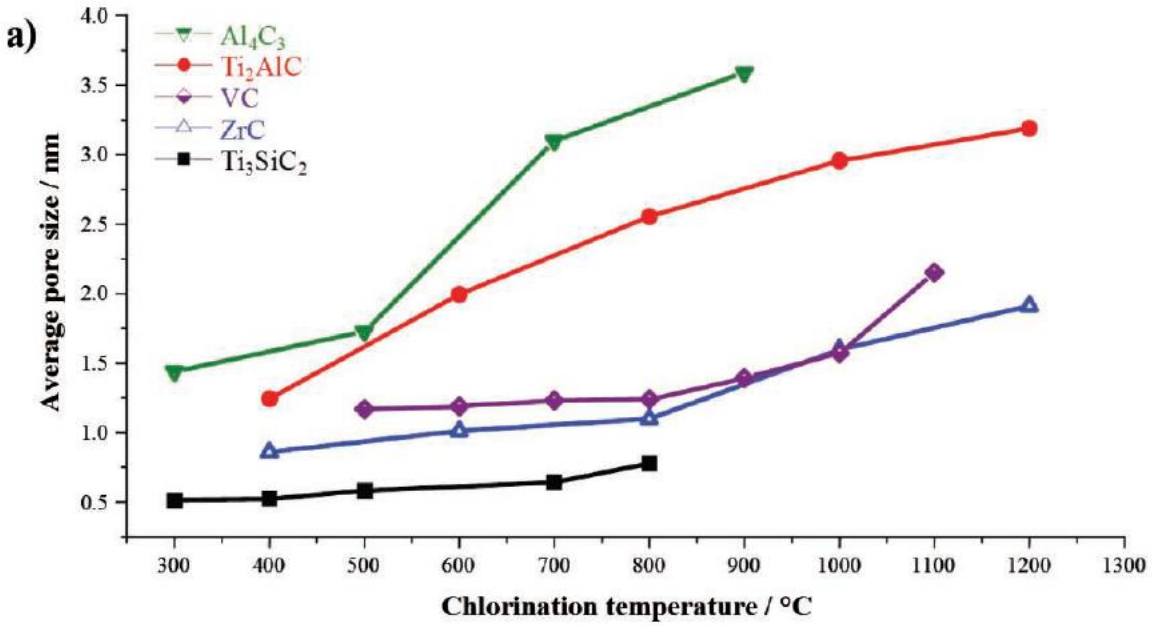

Figure 1.2 Dependence of Average Pore Size on Chlorination Temperature, Figure adapted from [40]

The synthesis of micro and mesoporous carbides has also been heavily investigated as another way to increase the bulk porosity of carbide-derived carbons.[52-58] Mesoporous carbides are usually synthesized through various soft and hard templating approaches. In a common nanocasting approach, ordered mesoporous silicas, such as SBA-15, or mesoporous carbons can be used as hard templates for the synthesis of carbides within their pore space. The template is then removed via HF or NaOH etching in the case of a silica template, or through oxidation to remove a carbon template while the carbide is kept intact. After template removal, both disordered and ordered carbides have been retained with significant porosity. Since the pores of the resulting carbide resemble the space previously occupied by the silica or carbon template, ordered

mesoporous carbides synthesized through this method allow great control of the size of the mesopore region through appropriate template selection. Combined with the tunability of pore size through the chlorination temperature, ordered mesoporous carbides allow extreme tunability of CDCs' pore size and good routes for addressing pore diffusion or pressure drop issues encountered in certain applications. In addition, upon chlorination of these carbide structures, the resulting carbide-derived carbons typically have surface areas greater than chlorination of the respective non-porous precursor.[54, 59]

1.5 Chemical Tunability of Carbide-derived Carbons

Carbide-derived carbons have proven to be exceptionally tailorable porous materials, and due to their tunable pore size and high bulk porosity, they have shown great performance in gas storage applications.[37, 39, 53, 60, 61] Recent efforts have focused on the addition of chemical functionalities in these materials to provide tailored guest-host interactions for other adsorptive and catalytic applications.[38, 62-67] Two common routes are the impregnation or incorporation of metal nanoparticles within these materials and the addition of surface functional groups through acidification or nitrogen modification.

Metal nanoparticles have been incorporated in CDCs through various methods. Traditional methods, such as wet impregnation, have been carried out on CDCs in a two step process: (1) the acidification of the CDC support to provide oxygen containing functional groups and (2) subsequent wet impregnation of the metal on functional group sites.[64, 68] However, due to the interconnectivity of the CDC pore structure, direct impregnation techniques can be susceptible to similar issues encountered by ordered mesoporous carbons, namely pore blockage and poor integration of metal. For example,

although the acidification and subsequent wet impregnation of Pt on TiC-CDC showed good dispersion of Pt, there was a sharp decrease in the specific surface area from 960 m^2 g^{-1} to 180 m^2 g^{-1}.[68] One way to circumvent this issue is the incorporation of metal within the carbide precursor before chlorination. An inverse microemulsion technique was used to add CeO_2, Pt, Pd, and Ru to polymeric polycarbosilane, which can subsequently be pyrolyzed to form a metal loaded SiC precursor.[62, 63] These catalytic metals are retained after chlorination of the SiC, and are present as well-dispersed nanoparticles within the synthesized CDC, exhibiting typically high specific surface areas (1500 – 2500 m^2 g^{-1}). Decreased pore blockage and increased dispersion can also be obtained through the use of carbides with secondary porosity before chlorination, for example the impregnation of SiC-CDC derived from commercial SiC foams.[69]

The addition of functional groups has also been explored. Nitric acid has been used to add oxygen containing functional groups on the surface of CDCs. This has been used to facilitate the impregnation of a metal on the CDC surface in previously mentioned studies, and also to increase the specific capacitance through improved wettability within electrochemical applications.[64, 67, 68] The addition of nitrogen groups through urea impregnation has also been investigated, and the addition of basic nitrogen groups on the surface drastically increases performance for H_2S filtration.[38]

Despite these initial investigations, there remain few easy and well established methods for the inclusion of metal nanoparticles and functional groups within carbide-derived carbons. Though CDCs feature extremely tunable physical characteristics, the interconnectivity of their pore structure can hinder the efficiency of common metal inclusion techniques developed for activated carbons. This need has driven current

investigations into novel methods to tailor the metal originating from the carbide precursor into a viable adsorptive site. In addition, there remain few investigations on the formation of functional groups through acidification of carbide-derived carbons. The tunability of the pore size of CDCs provides a systematic look into the formation and efficiency of these functional groups within unique pore spaces.

1.6 References

[1] Roney N, Llados F, Little S, Knaebel D. Toxicological Profile for Ammonia. In: Services DoHaH, ed. 2004, p. 101-42.

[2] Carson T, Osweiler G, Thorne P. Adverse Health Effects. Iowa Concentrated Animal Feeding Operations Air Quality Study 2002, p. 101-42.

[3] Rouquerol J, Avnir D, Fairbridge CW, Everett DH, Haynes JM, Pernicone N, et al. Recommendations for the characterization of porous solids. Pure and Applied Chemistry. 1994;66(8):1739–58.

[4] Karwacki CJ, Jones P. Toxic Industrial Chemicals Assessment of NBC Filter Performance. In: Center ECB, ed. 2000.

[5] Thompson JC. Compressibility of Metal-Ammonia Solutions. Physical Review A. 1971;4(2):802-4.

[6] Gonçalves M, Sánchez-García L, Oliveira Jardim Ed, Silvestre-Albero J, Rodríguez-Reinoso F. Ammonia Removal Using Activated Carbons: Effect of the Surface Chemistry in Dry and Moist Conditions. Environmental Science & Technology. 2011;45(24):10605-10.

[7] Le Leuch LM, Bandosz TJ. The role of water and surface acidity on the reactive adsorption of ammonia on modified activated carbons. Carbon. 2007;45(3):568-78.

[8] Grant Glover T, Peterson GW, Schindler BJ, Britt D, Yaghi O. MOF-74 building unit has a direct impact on toxic gas adsorption. Chemical Engineering Science. 2011;66(2):163-70.

[9] Jasuja H, Peterson GW, Decoste JB, Browe MA, Walton KS. Evaluation of MOFs for air purification and air quality control applications: Ammonia removal from air. Chemical Engineering Science. 2015;124(0):118-24.

[10] Petit C, Mendoza B, Bandosz TJ. Reactive Adsorption of Ammonia on Cu-Based MOF/Graphene Composites. Langmuir. 2010;26(19):15302-9.

[11] Petit C, Huang L, Jagiello J, Kenvin J, Gubbins KE, Bandosz TJ. Toward Understanding Reactive Adsorption of Ammonia on Cu-MOF/Graphite Oxide Nanocomposites. Langmuir. 2011;27(21):13043-51.

[12] Petit C, Bandosz TJ. Synthesis, Characterization, and Ammonia Adsorption Properties of Mesoporous Metal–Organic Framework (MIL(Fe))–Graphite Oxide Composites: Exploring the Limits of Materials Fabrication. Advanced Functional Materials. 2011;21(11):2108-17.

[13] Bashkova S, Bandosz TJ. Effect of surface chemical and structural heterogeneity of copper-based MOF/graphite oxide composites on the adsorption of ammonia. Journal of Colloid and Interface Science. 2014;417(0):109-14.

[14] Petit C, Karwacki C, Peterson G, Bandosz TJ. Interactions of ammonia with the surface of microporous carbon impregnated with transition metal chlorides. Journal of Physical Chemistry C. 2007;111(34):12705-14.

[15] Seredych M, Bandosz TJ. Removal of ammonia by graphite oxide via its intercalation and reactive adsorption. Carbon. 2007;45(10):2130-2.

[16] Petit C, Bandosz TJ. Removal of ammonia from air on molybdenum and tungsten oxide modified activated carbons. Environmental Science & Technology. 2008;42(8):3033-9.

[17] Seredych M, Tamashausky AV, Bandosz TJ. Graphite Oxides Obtained from Porous Graphite: The Role of Surface Chemistry and Texture in Ammonia Retention at Ambient Conditions. Advanced Functional Materials. 2010;20(10):1670-9.

[18] Seredych M, Bandosz TJ. Combined Role of Water and Surface Chemistry in Reactive Adsorption of Ammonia on Graphite Oxides. Langmuir. 2010;26(8):5491-8.

[19] Seredych M, Rossin JA, Bandosz TJ. Changes in graphite oxide texture and chemistry upon oxidation and reduction and their effect on adsorption of ammonia. Carbon. 2011;49(13):4392-402.

[20] Corre Y, Seredych M, Bandosz TJ. Analysis of the chemical and physical factors affecting reactive adsorption of ammonia on graphene/nanoporous carbon composites. Carbon. 2013;55:176-84.

[21] Le Leuch LM, Subrenat A, Le Cloirec P. Hydrogen Sulfide and Ammonia Removal on Activated Carbon Fiber Cloth-Supported Metal Oxides. Environmental Technology. 2005;26(11):1243-54.

[22] Guo J, Xu WS, Chen YL, Lua AC. Adsorption of NH3 onto activated carbon prepared from palm shells impregnated with H2SO4. Journal of Colloid and Interface Science. 2005;281(2):285-90.

[23] Fortier H, Westreich P, Selig S, Zelenietz C, Dahn JR. Ammonia, cyclohexane, nitrogen and water adsorption capacities of an activated carbon impregnated with increasing amounts of ZnCl(2), and designed to chemisorb gaseous NH(3) from an air stream. J Colloid Interface Sci. 2008;320(2):423-35.

[24] Long JW, Laskoski M, Peterson GW, Keller TM, Pettigrew KA, Schindler BJ. Metal-catalyzed graphitic nanostructures as sorbents for vapor-phase ammonia. Journal of Materials Chemistry. 2011;21(10):3477-84.

[25] Sharonov VE, Aristov YI. Ammonia adsorption by MgCl2, CaCl2 and BaCl2 confined to porous alumina: the fixed bed adsorber. Reaction Kinetics and Catalysis Letters. 2005;85(1):183-8.

[26] Huang C-C, Li H-S, Chen C-H. Effect of surface acidic oxides of activated carbon on adsorption of ammonia. Journal of Hazardous Materials. 2008;159(2–3):523-7.

[27] Seredych M, Bandosz TJ. Mechanism of Ammonia Retention on Graphite Oxides: Role of Surface Chemistry and Structure†. The Journal of Physical Chemistry C. 2007;111(43):15596-604.

[28] Liu Z-h, Wang Z-M, Yang X, Ooi K. Intercalation of Organic Ammonium Ions into Layered Graphite Oxide. Langmuir. 2002;18(12):4926-32.

[29] Peterson GW, Wagner GW, Balboa A, Mahle J, Sewell T, Karwacki CJ. Ammonia Vapor Removal by Cu(3)(BTC)(2) and Its Characterization by MAS NMR. The journal of physical chemistry C, Nanomaterials and interfaces. 2009;113(31):13906-17.

[30] DeCoste JB, Peterson GW. Metal–Organic Frameworks for Air Purification of Toxic Chemicals. Chemical Reviews. 2014;114(11):5695-727.

[31] Britt D, Tranchemontagne D, Yaghi OM. Metal-organic frameworks with high capacity and selectivity for harmful gases. Proceedings of the National Academy of Sciences. 2008;105(33):11623-7.

[32] Küsgens P, Rose M, Senkovska I, Fröde H, Henschel A, Siegle S, et al. Characterization of metal-organic frameworks by water adsorption. Microporous and Mesoporous Materials. 2009;120(3):325-30.

[33] Burtch NC, Jasuja H, Walton KS. Water Stability and Adsorption in Metal–Organic Frameworks. Chemical Reviews. 2014;114(20):10575-612.

[34] Jasuja H, Burtch NC, Huang Y-g, Cai Y, Walton KS. Kinetic Water Stability of an Isostructural Family of Zinc-Based Pillared Metal–Organic Frameworks. Langmuir. 2013;29(2):633-42.

[35] Schoenecker PM, Carson CG, Jasuja H, Flemming CJJ, Walton KS. Effect of Water Adsorption on Retention of Structure and Surface Area of Metal–Organic Frameworks. Industrial & Engineering Chemistry Research. 2012;51(18):6513-9.

[36] Gogotsi Y, Dash RK, Yushin G, Yildirim T, Laudisio G, Fischer JE. Tailoring of Nanoscale Porosity in Carbide-Derived Carbons for Hydrogen Storage. Journal of the American Chemical Society. 2005;127(46):16006-7.

[37] Kim HS, Singer JP, Gogotsi Y, Fischer JE. Molybdenum carbide-derived carbon for hydrogen storage. Microporous and Mesoporous Materials. 2009;120(3):267-71.

[38] Seredych M, Portet C, Gogotsi Y, Bandosz TJ. Nitrogen modified carbide-derived carbons as adsorbents of hydrogen sulfide. J Colloid Interface Sci. 2009;330(1):60-6.

[39] Presser V, McDonough J, Yeon S-H, Gogotsi Y. Effect of pore size on carbon dioxide sorption by carbide derived carbon. Energy & Environmental Science. 2011;4(8):3059.

[40] Presser V, Heon M, Gogotsi Y. Carbide-Derived Carbons - From Porous Networks to Nanotubes and Graphene. Advanced Functional Materials. 2011;21(5):810-33.

[41] Gogotsi Y, Nikitin A, Ye H, Zhou W, Fischer JE, Yi B, et al. Nanoporous carbide-derived carbon with tunable pore size. Nat Mater. 2003;2(9):591-4.

[42] Jänes A, Thomberg T, Lust E. Synthesis and characterisation of nanoporous carbide-derived carbon by chlorination of vanadium carbide. Carbon. 2007;45(14):2717-22.

[43] Tallo I, Thomberg T, Kontturi K, Jänes A, Lust E. Nanostructured carbide-derived carbon synthesized by chlorination of tungsten carbide. Carbon. 2011;49(13):4427-33.

[44] Dash R, Chmiola J, Yushin G, Gogotsi Y, Laudisio G, Singer J, et al. Titanium carbide derived nanoporous carbon for energy-related applications. Carbon. 2006;44(12):2489-97.

[45] Dash RK, Yushin G, Gogotsi Y. Synthesis, structure and porosity analysis of microporous and mesoporous carbon derived from zirconium carbide. Microporous and Mesoporous Materials. 2005;86(1-3):50-7.

[46] Hoffman EN, Yushin G, El-Raghy T, Gogotsi Y, Barsoum MW. Micro and mesoporosity of carbon derived from ternary and binary metal carbides. Microporous and Mesoporous Materials. 2008;112(1-3):526-32.

[47] Leis J, Perkson A, Arulepp M, Käärik M, Svensson G. Carbon nanostructures produced by chlorinating aluminium carbide. Carbon. 2001;39(13):2043-8.

[48] Leis J, Perkson A, Arulepp M, Nigu P, Svensson G. Catalytic effects of metals of the iron subgroup on the chlorination of titanium carbide to form nanostructural carbon. Carbon. 2002;40(9):1559-64.

[49] Jeong J-H, Bae H-T, Lim D-S. The effect of iron catalysts on the microstructure and tribological properties of carbide-derived carbon. Carbon. 2010;48(12):3628-34.

[50] Perkson A, Leis J, Arulepp M, Käärik M, Urbonaite S, Svensson G. Barrel-like carbon nanoparticles from carbide by catalyst assisted chlorination. Carbon. 2003;41(9):1729-35.

[51] Portet C, Kazachkin D, Osswald S, Gogotsi Y, Borguet E. Impact of synthesis conditions on surface chemistry and structure of carbide-derived carbons. Thermochimica Acta. 2010;497(1-2):137-42.

[52] Borchardt L, Oschatz M, Lohe M, Presser V, Gogotsi Y, Kaskel S. Ordered mesoporous carbide-derived carbons prepared by soft templating. Carbon. 2012;50(11):3987-94.

[53] Kockrick E, Schrage C, Borchardt L, Klein N, Rose M, Senkovska I, et al. Ordered mesoporous carbide derived carbons for high pressure gas storage. Carbon. 2010;48(6):1707-17.

[54] Krawiec P, Kockrick E, Borchardt L, Geiger D, Corma A, Kaskel S. Ordered Mesoporous Carbide Derived Carbons: Novel Materials for Catalysis and Adsorption. The Journal of Physical Chemistry C. 2009;113(18):7755-61.

[55] Tsai W-Y, Gao P-C, Daffos B, Taberna P-L, Perez CR, Gogotsi Y, et al. Ordered mesoporous silicon carbide-derived carbon for high-power supercapacitors. Electrochemistry Communications. 2013;34:109-12.

[56] Oschatz M, Kockrick E, Rose M, Borchardt L, Klein N, Senkovska I, et al. A cubic ordered, mesoporous carbide-derived carbon for gas and energy storage applications. Carbon. 2010;48(14):3987-92.

[57] Borchardt L, Oschatz M, Graetz S, Lohe MR, Rümmeli MH, Kaskel S. A hard-templating route towards ordered mesoporous tungsten carbide and carbide-derived carbons. Microporous and Mesoporous Materials. 2014;186:163-7.

[58] Borchardt L, Hoffmann C, Oschatz M, Mammitzsch L, Petasch U, Herrmann M, et al. Preparation and application of cellular and nanoporous carbides. Chemical Society Reviews. 2012;41(15):5053-67.

[59] Korenblit Y, Rose M, Kockrick E, Borchardt L, Kvit A, Kaskel S, et al. High-Rate Electrochemical Capacitors Based on Ordered Mesoporous Silicon Carbide-Derived Carbon. ACS Nano. 2010;4(3):1337-44.

[60] Vakifahmetoglu C, Presser V, Yeon S-H, Colombo P, Gogotsi Y. Enhanced hydrogen and methane gas storage of silicon oxycarbide derived carbon. Microporous and Mesoporous Materials. 2011;144(1–3):105-12.

[61] Wang H, Zhu T, Fan X, Na H. Adsorption and desorption of small molecule volatile organic compounds over carbide-derived carbon. Carbon. 2014;67:712-20.

[62] Borchardt L, Hasché F, Lohe MR, Oschatz M, Schmidt F, Kockrick E, et al. Transition metal loaded silicon carbide-derived carbons with enhanced catalytic properties. Carbon. 2012;50(5):1861-70.

[63] Kockrick E, Borchardt L, Schrage C, Gaudillere C, Ziegler C, Freudenberg T, et al. CeO2/Pt Catalyst Nanoparticle Containing Carbide-Derived Carbon Composites by a New In situ Functionalization Strategy. Chemistry of Materials. 2010;23(1):57-66.

[64] Hasse B, Gläsel J, Kern AM, Murzin DY, Etzold BJM. Preparation of carbide-derived carbon supported platinum catalysts. Catalysis Today. 2015;249(0):30-7.

[65] Sevilla M, Mokaya R. Activation of carbide-derived carbons: a route to materials with enhanced gas and energy storage properties. Journal of Materials Chemistry. 2011;21(13):4727.

[66] Sevilla M, Foulston R, Mokaya R. Superactivated carbide-derived carbons with high hydrogen storage capacity. Energy & Environmental Science. 2010;3(2):223-7.

[67] Zheng L, Wang Y, Wang X, Wang X, An H, Yi L. The effects of surface modification on the supercapacitive behaviors of carbon derived from calcium carbide. Journal of Materials Science. 2010;45(22):6030-7.

[68] Schlange A, dos Santos AR, Hasse B, Etzold BJM, Kunz U, Turek T. Titanium carbide-derived carbon as a novel support for platinum catalysts in direct methanol fuel cell application. Journal of Power Sources. 2012;199:22-8.

[69] Glenk F, Knorr T, Schirmer M, Gütlein S, Etzold BJM. Synthesis of Microporous Carbon Foams as Catalyst Supports. Chemical Engineering & Technology. 2010;33(4):698-703.

CHAPTER 2

MATERIALS AND METHODS

2.1 Methods

To synthesized, characterize, and evaluate the materials present in this work, a series of custom experimental setups were built in-house. This section serves to expand on methods that are briefly explained in future chapters.

2.1.1 Carbide-derived Carbon Synthesis Experimental Setup

For this work, carbide-derived carbons were synthesized on an in-house chlorination setup. The system was designed similar to setups in literature, generally consisting of sample placed on a quartz or alumina boat within a quartz tube that can be heated using a horizontal tube furnace.[1-5] Many safety and design constraints were taken under consideration to minimize the risk involved with handling concentrated chlorine gas and ensuring smooth operation within limited fume hood space. A full schematic of the chlorination reactor setup can be seen in **Figure 2.1** below. A chlorine gas (Airgas 99.5%) lecture bottle was attached to a cross purge panel with a stainless steel regulator (Nexair PRS40223731-180D) and sealed with a PTFE o-ring. After the regulator, an actuator ball valve (Swagelok SS-43GS4-42AC) hooked up to a switch outside the fume hood is used to remotely enable chlorine flow to regulator. The switch is also used as an emergency shutoff valve, to limit the flow of chlorine past the regulator in case of any substantial leak downstream that would prevent a user from safely reaching in to close the chlorine lecture bottle manually. The chlorine stream is regulated to the desired flow

rate by a mass flow controller. A separate line, controlled by a mass flow meter, is used to dilute the chlorine gas to the desired concentration with Argon (Airgas 99.999%). This line can also be switched to a 5% H_2 in Argon tank using a 3-way valve for CDC annealing, if desired.

All lines, except for the quartz tube, are ¼" OD PFA tubing. Although 316 stainless steel is rated as "Good" against dry chlorine, small amounts of H_2O that are able to infiltrate the system as an impurity in reacting gases or from humid air during system maintenance can quickly convert Cl_2 to HCl and cause corrosion with stainless steel. In addition, these issues are easily spotted using PFA, as the distinctive yellow hue of HCl is a quick indicator of small amounts of water in the system likely due to inadequate purging after attaching the quartz reactor to the system. Despite their flexibility, no leak issues were seen with PFA.

The ¼" PFA is expanded to 1" OD, via several stainless steel fitting adapters to match the 1" OD of the quartz tube reactor. Two 1" Ultra Torr fittings with Viton o-rings are used to connect and disconnect a 20" long, 1" OD quartz tube from a horizontal tube furnace (Thermo Scientific Lindberg® Blue M® Mini-Mite™) where chlorination takes place at temperatures ranging from 200-1000^{o}C. The effluent stream from the reactor is bubbled through a concentrated NaOH solution to neutralize excess chlorine gas, HCl, and metal chlorides.

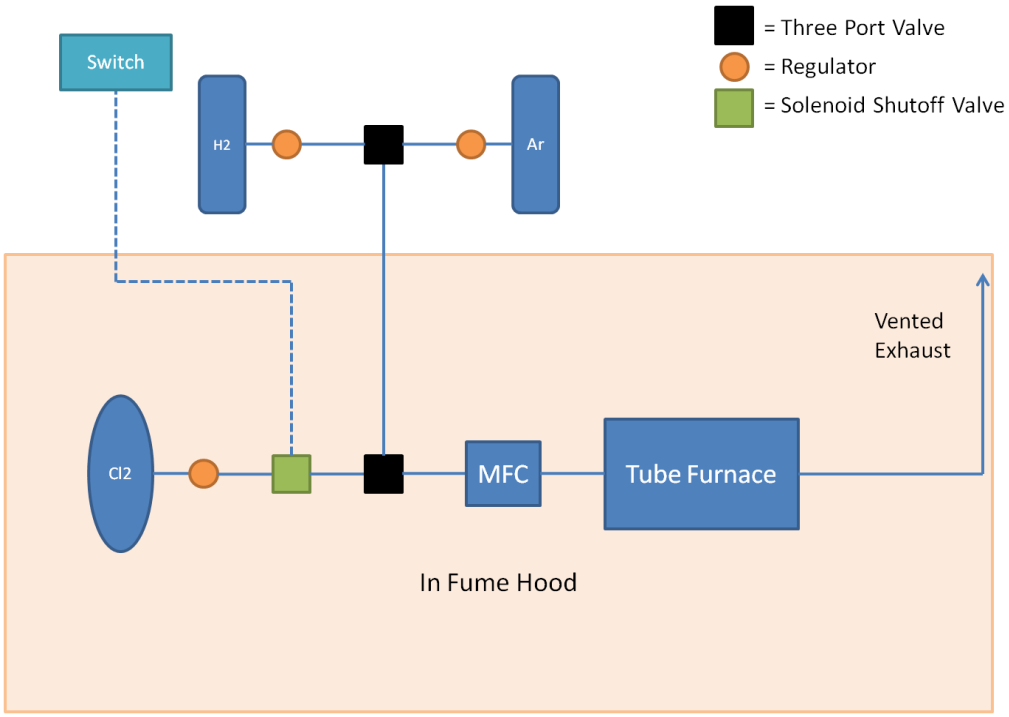

Figure 2.1. Carbide-derived Carbon Chlorination Reactor Schematic

2.1.2 Ammonia Breakthrough System Experimental Setup

To evaluate the ammonia adsorption capabilities of the synthesized samples within this work, an ammonia breakthrough system was designed for dynamic adsorption experiments under both dry and humid conditions. The micro-bed setup was used to evaluate milligram quantities of both MOF and CDC materials as ammonia adsorbents. Both the experimental procedure and system specifications heavily mirrored an experimental setup designed by the Edgewood Chemical Biological Center (ECBC).[6-8] This allowed easy and systematic comparison between materials tested at the center and in our laboratory. After initial testing, a vertical bed orientation was chosen, as this was seen to have the best repeatability between multiple runs. To account for the dead volume within the system, a blank bed of sand was used to calculate the time ammonia would reach the sensor in the absence of a porous adsorbent. This was subtracted from the breakthrough time of evaluated samples.

Figure 2.2 and **Figure 2.3** below provide the schematic for the ammonia breakthrough system under both dry (0% RH) and humid (75% RH) conditions.

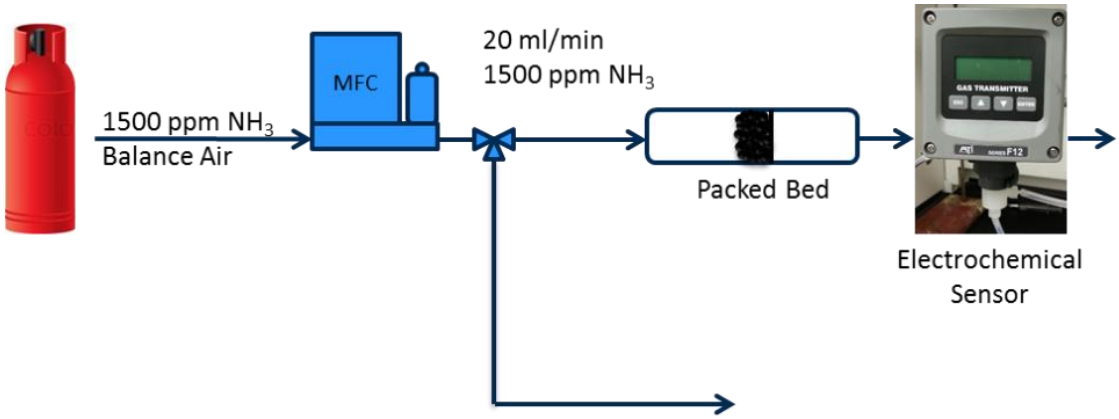

Figure 2.2. Ammonia Breakthrough System Apparatus Under Dry Conditions

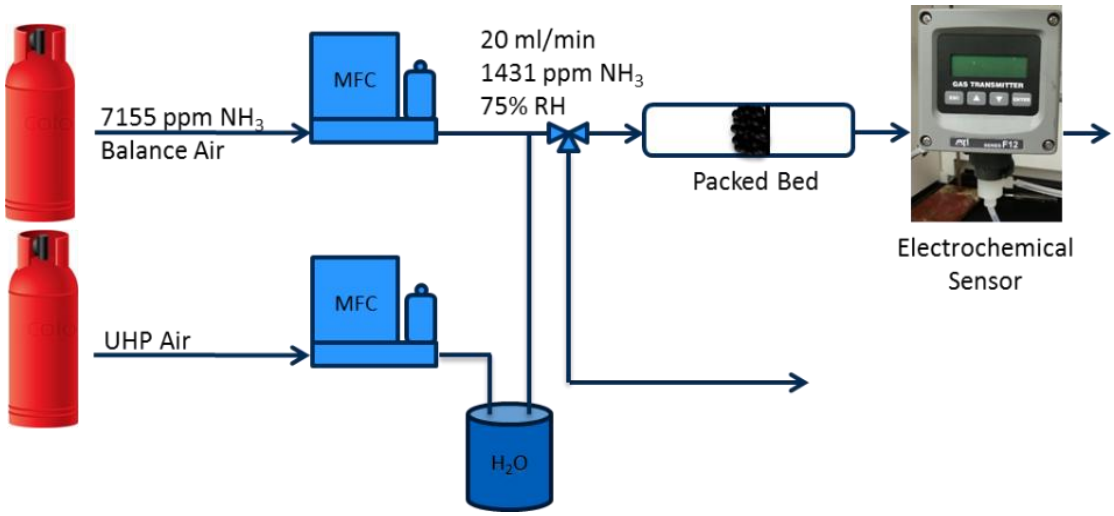

Figure 2.3. Ammonia Breakthrough System Apparatus Under Dry Conditions

The experimental procedure is as follows. Fine powder is packed within a quartz bed against a fine quartz frit of ID 4 mm to a standardized bed volume of 55mm^3. Samples are activated using heat tape for the desired time and temperature conditions under N_2 flow and then allowed to cool to room temperature. After cooling, the dry or wet breakthrough run was started. A dry run was initiated by switching the N_2 to a stream of 1500 ppm NH_3 in air at a rate of 20 ml min^{-1} (Airgas). The effluent stream was

analyzed using an Analytical Technology H10-15 ammonia electrochemical sensor. Once the dilute NH_3 stream is switched on, data points are taken at 30 second intervals until the sensor reached 500 ppm NH_3, at which point the NH_3 is switched off to preserve the life of the sensor. N_2 flow was maintained at 50 ml min^{-1} to capture the desorption behavior of the bed, and the sensor reading was recorded until the NH_3 concentration returned to ~100 ppm.

For humid breakthrough experiments, a humid stream is created by flowing air at 16 ml min^{-1} through a H_2O bubbler, and then combining it with a NH_3 stream of 7155 ppm and a flow rate of 4 ml min^{-1}. The total mixed stream flowed through the packed bed at a rate of 20 ml min^{-1} with a measured relative humidity of 75% and a calculated NH_3 concentration of 1431 ppm. The experimental procedure for wet and dry conditions were identical. Data points were again taken at 30 second intervals until the sensor reached 500 ppm NH_3, at which point the ammonia stream was switched to N_2 flow at 50 ml min^{-1} and the desorption behavior was recorded.

2.2 References

[1] Leis J, Perkson A, Arulepp M, Nigu P, Svensson G. Catalytic effects of metals of the iron subgroup on the chlorination of titanium carbide to form nanostructural carbon. Carbon. 2002;40(9):1559-64.

[2] Gogotsi Y, Nikitin A, Ye H, Zhou W, Fischer JE, Yi B, et al. Nanoporous carbide-derived carbon with tunable pore size. Nat Mater. 2003;2(9):591-4.

[3] Ávila-Brande D, Katcho NA, Urones-Garrote E, Gómez-Herrero A, Landa-Cánovas AR, Otero-Díaz LC. Nano-structured carbon obtained by chlorination of NbC. Carbon. 2006;44(4):753-61.

[4] Becker P, Glenk F, Kormann M, Popovska N, Etzold BJM. Chlorination of titanium carbide for the processing of nanoporous carbon: A kinetic study. Chemical Engineering Journal. 2010;159(1–3):236-41.

[5] Borchardt L, Hasché F, Lohe MR, Oschatz M, Schmidt F, Kockrick E, et al. Transition metal loaded silicon carbide-derived carbons with enhanced catalytic properties. Carbon. 2012;50(5):1861-70.

[6] Long JW, Laskoski M, Peterson GW, Keller TM, Pettigrew KA, Schindler BJ. Metal-catalyzed graphitic nanostructures as sorbents for vapor-phase ammonia. Journal of Materials Chemistry. 2011;21(10):3477-84.

[7] Grant Glover T, Peterson GW, Schindler BJ, Britt D, Yaghi O. MOF-74 building unit has a direct impact on toxic gas adsorption. Chemical Engineering Science. 2011;66(2):163-70.

[8] Jasuja H, Peterson GW, Decoste JB, Browe MA, Walton KS. Evaluation of MOFs for air purification and air quality control applications: Ammonia removal from air. Chemical Engineering Science. 2015;124(0):118-24.

CHAPTER 3

SYNTHESIS OF EMBEDDED IRON NANOPARTICLES IN FE3C-DERIVED CARBONS

Parts of this chapter are adapted from Mangarella, M.C., Ewbank, J.L., Dutzer, M.R., Alamgir, F.M., and Walton, K.S. (2014). Synthesis of Embedded Iron Nanoparticles in Fe_3C-derived Carbons. Carbon 79, 74-84.

3.1 Summary

Carbide-derived carbons with embedded Fe nanoparticles are synthesized by partial chlorination of iron carbide at 600^{o}C. Interestingly, the residual Fe studied by X-ray absorption near edge spectroscopy, scanning electron microscopy, and transmission electron microscopy show the extraction process does not follow a layer-by-layer extraction process, as proposed in the literature for the chlorination of other carbides. Instead, a large percentage of iron carbide converts to iron (II) and iron (III) chloride nanoparticles, which remain trapped within the resulting nanoporous carbon framework. Further reductive treatment can be used to produce dispersed Fe nanoparticles with an average particle diameter approaching 10nm.

3.2. Introduction

Porous carbons have long been attractive materials due to their low cost, tunable porosity, and superior chemical stability. Over the past few decades, carbon materials have garnered great attention as catalyst supports, sorbents, electrodes, etc. due to increased control over their pore structure through the use of nanocasting and other

synthesis approaches.[1-4] In addition, increasingly ordered carbon structures, such as SWNTs, graphene, fullerenes and nanodiamond, have been investigated due to great inherent tribological and conductive properties.[4] A new class of highly tailorable nanoporous carbons, carbide-derived carbons (CDCs), has also recently been established.[2, 5-9] These materials are produced through the selective extraction of a metal or heteroatom from a carbide precursor, commonly by halogenation. The resulting nanoporous carbon exhibits large specific surface areas and a high degree of microporosity. Many comprehensive studies have demonstrated that the pore size can be tuned with sub-angstrom precision by varying the chlorination temperature.[2, 7, 9-12] Therefore, many CDC materials have been investigated for gas storage, filtration, catalysis, capacitance, and other applications.[11, 13-17]

There has been growing interest to functionalize CDCs with metal nanoparticles.[18-20] Many traditional methods focus on impregnation of the metal by wetting the adsorbent with a solution containing the metal precursor. However, this often results in limited control of metal particle size, pore blockage of the carbon support, and weak support-metal interactions, particularly within templated pore architectures that rely on interconnecting pores.[21] As such, many new approaches have focused on in-situ approaches to limit pore blockage and maximize dispersion.[20, 22] Still these approaches can require lengthy synthesis procedures, and have motivated this study to investigate the viability of the metal in the metal carbide as an active site. This requires a careful look into the extraction process of the metal atom from the metal carbide, to fundamentally understand the species and dispersion of the metal if the chlorination reaction is halted before complete extraction. Studies within the literature for certain carbides, such as NbC

and SiC, show largely layer-by-layer extraction of the carbide precursor, leading to an undesirable and poorly distributed core of metal carbide.[23, 24] However, other metal carbides should be investigated as there is good evidence in the literature that they would undergo a different extraction mechanism than layer-by-layer extraction.

Iron carbide (Fe_3C) was chosen as the carbide precursor. Iron has also been shown to play an interesting role in CDC synthesis. The presence of minute quantities of iron has been shown to affect the nanostructure of the resulting CDC, producing nanodiamond, barrel-like carbon nanoparticles, and other structured carbon domains.[25-28] Graphitic carbon nanospheres and amorphous carbon nanotubes are found in the chlorination of ferrocene, and some structures are seen to surround $FeCl_2$ nanoparticles.[29, 30] Interestingly, $FeCl_3$ is the only expected product from the chlorination of ferrocene. It is hypothesized that these particles originate from retained $FeCl_3$ species that are reduced to $FeCl_2$ while they remain trapped in carbon nanostructures that prevent their sublimation. The retention of iron chloride nanoparticles upon the chlorination of Fe_3C would be highly attractive and a significant deviation from traditional layer-by-layer extraction. A previous investigation into the chlorination of Fe_3C demonstrated iron's role as a graphitization catalyst, producing high purity graphite at certain chlorination temperatures.[31, 32] Previous thermodynamic simulations on the chlorination of Fe_3C have shown that chlorination at moderate temperatures could produce solid $FeCl_2$ products within a closed system.[31] The presence of residual iron chloride species for certain chlorination temperatures was also noted by X-ray diffraction (XRD) in this study, and it was postulated that H_2 gas could be used to reduce the iron chloride species to prepare Fe

supported catalysts.[32] However, the iron chloride species were removed by HCl washing, and no further characterization was reported.

In this work, Fe_3C is chlorinated for varying chlorination times and samples were characterized by many techniques to understand the evolution of Fe dispersion and speciation. The objective of this study is to fundamentally understand the dispersion and speciation of the residual Fe at various extents of the chlorination reaction, and gain insight into the extraction process of Fe from Fe_3C. The goal of this study is to demonstrate the ability to create and control retained metal nanoparticles in Fe_3C-derived carbons (Fe_3C-CDCs) to aid their use in catalytic and adsorptive applications. Iron is an ideal candidate for this study because of the pervasiveness of iron species as adsorptive sites in catalytic and filtration processes, as well as the availability and low-cost of iron carbide.[33, 34] In addition, though Fe_3C has been chlorinated to form CDC materials previously in the literature, no porosity characterization for Fe_3C-derived carbons have currently been published, which is of principle interest for these applications.

3.3 Materials and Methods

3.3.1 Materials

One gram of Fe_3C (F. J. Brodmann & Co. 99.5% purity -200/+270 mesh) was placed on a quartz boat and inserted into a quartz tube of ID 1", length 20" and into a horizontal tube furnace. Each sample was heated to 600^{o}C at a ramp rate of 5^{o}C min^{-1} under Ar flow (Airgas 99.999%) at a rate of 100 ml min^{-1} and at ambient pressure. After reaching 600^{o}C, chlorine gas (Airgas 99.5%) flow was introduced into the reactor at a flow rate of 25 ml min^{-1} for a predetermined chlorination time ranging from 0.25-3 hours.

The Ar flow was maintained during chlorination. Acidic gases present in the effluent stream (Cl_2, HCl, iron chlorides) were neutralized with a concentrated NaOH scrubber solution downstream of the reactor.

After the chlorination time had elapsed the chlorine gas flow was turned off. Samples were maintained at 600^{o}C for 30 minutes under Ar flow, and then cooled to room temperature. A second series of annealed Fe_3C-CDCs were prepared for each chlorination time. These samples were purged with Ar for 30 minutes at 600^{o}C, after which the Ar flow was switched to 5% H_2 in Ar (99.999%) at a rate of 100 ml min^{-1} for 3 hours at 600^{o}C to remove residual chlorine. Afterwards, these samples were cooled to room temperature under Ar flow.

Unannealed samples were subsequently labeled as Fe_3C-CDC-CT, where CT stands for chlorination time, such as 0.25h, 0.5h, 0.75h, 1.0h, and 1.5h. Annealed samples were labeled as Fe_3C-CDC-CT-H_2 to denote exposure to hydrogen. In addition, layer separation was noted for Fe_3C-CDC-0.25h and Fe_3C-CDC-0.5h samples. These samples were hand-sieved and separated into a top, black powdered layer, and a bottom, silver/brown particulate layer. These samples were further subdivided into Fe_3C-CDC-CT-top and Fe_3C-CDC-CT-bot to denote either the top or bottom layer, respectively. The Fe_3C-CDC prefix is dropped in subsequent figures and throughout this chapter for brevity.

3.3.2 Methods

PXRD (Powder X-ray Diffraction) patterns were collected using an X'Pert X-ray PANalytical diffractometer with a Cu Kα X-ray source (λ = 1.5418 Å). XRD spectrums were collected from a range of 4-90^{o} in two theta (2θ) with a step size of 0.02^{o}. All

samples were run at room temperature. Nitrogen adsorption measurements were obtained on a Quadrasorb System from Quantachrome Instruments. Isotherms were collected at 77K using a sample of 30-50mg. Prior to each isotherm, samples were activated overnight at 423K under vacuum. Specific surface areas were calculated using the BET model under the pressure range 0.01-0.05 P/P_0. Pore size distributions for all samples were obtained using the Quenched Solid Density Functional Theory (QSDFT) model built into version 5.11 QuadraWin^{TM} software. An adsorption branch slit-pore/cylindrical pore model, nitrogen adsorbate, and carbon adsorbent were assumed for the DFT model parameters. Thermogravimetric analyses of all samples were carried out on a NETZSCH STA 449 F1 Jupiter instrument. Approximately 10mg of sample were heated from 25-1500^{o}C at a ramp rate of 5^{o}C min^{-1} and a flow rate of 20 ml min^{-1} of air (Airgas 99.999%). Residual metal % was calculated by assuming total combustion of carbon, and conversion of Fe to Fe_2O_3.

Pre-edge and XANES Fe K-edge spectra were collected at beamline 12-BM-B at the Advanced Photon Source of Argonne National Laboratories (Chicago). A Si(111) double monochromator was used to select the beam energy for all measurements. The beam size was 800µm x 1000µm. Samples were pressed into wafers of 13mm diameter and fixed to a sample stage with adhesive tape. The beam was internally calibrated with a metallic Fe reference foil, which was also run in series with all samples to account and correct for the energy shift of the beam. The first inflection point of the Fe K-edge was set to 7111.08 eV. XANES data was collected in transmission mode via the use of ionization chambers, and a step size of 0.3 eV was used. Before each sample, an area

scan of beam flux was taken to ensure no pinholes in the pressed wafer. Data was analyzed within Athena software.[35]

SEM images were obtained using a LEO 1530 Thermally-Assisted Field Emission (TFE) Scanning Electron Microscope (SEM). All samples were deposited onto carbon tape and not sputter coated prior to scanning. Images were scanned at an accelerating voltage of 3-10kV, depending on the charging effects of the sample. Particle size distributions were obtained by measuring the diameter of 50-100 particles from multiple SEM images of each sample. TEM images were obtained using a JEOL 100CX II transmission electron microscope (TEM) at an operating voltage of 100kV. Samples were suspended in a solution of methanol and deposited on a lacey carbon grid. High resolution (HRTEM) images were obtained using a FEI Tecnai F30 at an operating voltage of 300kV. Other HRTEM images were obtained using a Hitachi HT7700 TEM at an operating voltage of 120kV.

3.4 Results and Discussion

3.4.1 Structural properties and porosity characteristics of prepared Fe3C-CDCs

Figure 3.1 provides a reaction schematic for prepared Fe_3C-derived carbons. Iron was extracted by chlorine gas to form iron chloride compounds by the following reactions:

$$Fe_3C + \frac{9}{2}Cl_2 \rightarrow 3FeCl_3 + C \quad (1)$$

$$Fe_3C + 3Cl_2 \rightarrow 3FeCl_2 + C \quad (2)$$

The adsorption properties were investigated by nitrogen physisorption. The isotherms at 77K can be seen in **Figure 3.2**, with porosity results summarized in **Table 3.1**. The Fe_3C precursor exhibits little specific surface area (20 m^2 g^{-1}) and pore volume (0.02 cc g^{-1}). Unannealed Fe_3C-CDCs prepared at chlorination times ≤ 0.5 hours formed two layers: a black, powdery top layer and a silver/brown clay bottom layer. The relative mass percentages of each layer are reported in **Table A.2** in **Appendix A**. At chlorination times ≥ 0.75 hours, no layer separation was seen, and the Fe_3C-CDC visually resembled the black, powdery top layer at low chlorination times. All Fe_3C-CDCs annealed in H_2 formed one visually homogenous black powder layer irrespective of chlorination time.

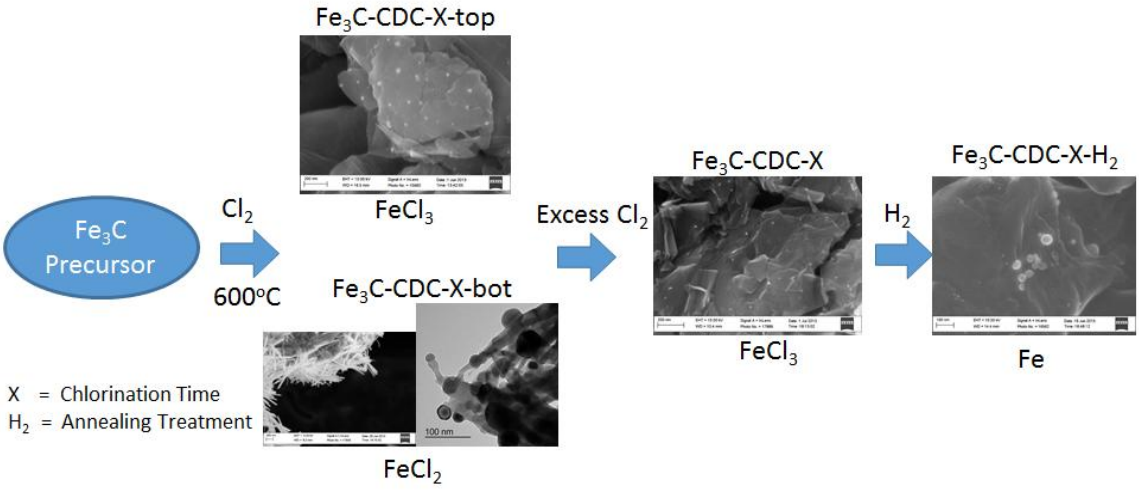

Figure 3.1. Reaction Schematic and Summary of the chlorination of Fe_3C

The specific surface area and pore volume are strongly affected by the chlorination time and annealing treatment. The bottom layers (0.25h-bot, 0.5h-bot) have little (~50 m^2 g^{-1}) porosity while the top layers (0.25h-top, 0.5h-top), as well as 0.75h and 1.0h samples, have progressively increasing porosity and characteristic type IV isotherms according to the Brunauer classification.[36-38] Annealed samples also exhibit type IV isotherms, seen in **Figure 3.2**, with a H2 type hysteresis that exhibits a sharp desorption

branch and a gradual increase in the adsorption branch. This signifies the presence of cavitation effects, and the closure of the hysteresis around the relative pressure P/P_0 = 0.42 can be attributed to a sudden nucleation of nitrogen gas bubbles within the mesopores of annealed Fe_3C-CDC samples.[39-41] To verify that the hysteresis was not caused by a chemisorption mechanism due to residual Fe, a sample with a large amount of residual iron, 0.25h-H_2, was recorded twice in series. There was no significant change in specific surface area, signifying no irreversible chemisorption.

Table 3.1. Porosity and residual metal for prepared Fe_3C-CDCs

Sample Name	Chlorination Time (h)	Annealing Time (h)	Specific Surface Area ($m^2\ g^{-1}$)[a]	Pore Volume (cc g^{-1})[b]	Residual Metal (%)[c]
Fe_3C	0	0	20	0.02	93
0.25h-top	0.25	0	96	0.18	-
0.25h-bot	0.25	0	53	0.14	-
0.25h-H_2	0.25	3	147	0.13	77.3
0.5h-top	0.50	0	229	0.26	-
0.5h-bot	0.50	0	51	0.15	-
0.5h-H_2	0.50	3	356	0.31	25.5
0.75h	0.75	0	339	0.34	-
0.75h-H_2	0.75	3	667	0.53	8.4
1.0h	1.0	0	374	0.40	-
1.0h-H_2	1.0	3	657	0.48	4.0
1.5h	1.5	0	353	0.38	-
1.5h-H_2	1.5	3	683	0.54	2.7
3.0h-H_2	3.0	3	-	-	0.8

a)Obtained by BET[36] Analysis at a Relative Pressure Range of 0.01-0.05 P/P0 b) Obtained at P/P0 = 0.99 c) Calculated by TGA

Annealed samples exhibit significantly higher surface areas, with a 97% increase in surface area comparatively between 0.75h and 0.75h-H_2. Hydrogen has been shown to be a far more effective annealing gas than Ar for Cl_2 removal from CDCs, and the drastic increase in porosity can be explained by a combination of the removal of physisorbed

chlorine gas, bonded surface Cl species, and the conversion of $FeCl_x$ species.[42] There is a maximum surface area and pore volume obtained at chlorination times ≥ 0.75 hours (0.75h-H_2 – 667 m^2 g^{-1}, 0.53 cc g^{-1}). These values are low for CDC materials, but the reaction temperature in this study was not optimized to obtain maximum porosity. Also, the onset of significant graphitization, as seen in the synthesis of other carbide-derived carbons, has been shown to severely reduce surface area and pore volume.[12] The presence of well-ordered graphitic sheets seen in Fe_3C-CDCs can limit porosity as the d-spacing of graphite, 3.4Å, can hinder the accessibility of the nitrogen probe molecule.[31]

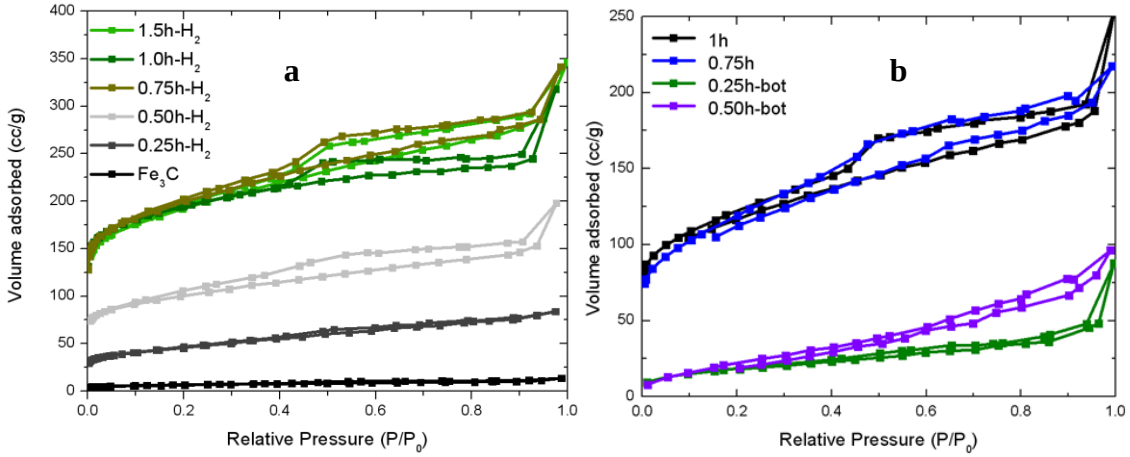

Figure 3.2. N_2 adsorption isotherms for (a) Fe_3C and annealed Fe_3C-CDCs, and (b) unannealed Fe_3C-CDCs

The hysteresis loop for unannealed Fe_3C-CDCs at long chlorination times and annealed Fe_3C-CDCs corresponds to a broad (002) graphite reflection in the XRD spectrum as seen in **Figure 3.3**, indicating the formation of a significant amount of mesoporosity as the degree of graphitization increases. The formation of highly ordered graphitic sheets was also observed in SEM, which will be discussed in greater detail in Section *2.2.1*. In addition to the (002) graphite reflection, the (004) graphite reflection can be seen at 2θ = ~55° for longer chlorination times. Other peaks were observed for annealed samples, present at 2θ = ~45°, ~65°, and ~82° corresponding to the (011), the

(002), and the (112) reflection of α-Fe. Peaks are also seen in unannealed samples at >0.75h present at 2θ = ~32°, ~35.5°, ~48° with d-spacings of 0.272, 0.244, and 0.178 nm respectively. Other studies have attributed similar peaks to more ordered carbon structures, such as nanodiamond, but confirmation of these structures was not obtained by TEM in this study.[28] The possible attribution of these peaks to residual iron complexes was also studied. The disappearance of peaks from the commercial Fe_3C spectrum in **Figure 3.3(b)** after short chlorination times indicate the precursor is quickly converted to iron chloride products. In **Figure 3.3(a)**, the intensity of the peak at 2θ = ~45° correlates very well with the percent of residual metal in annealed samples, supporting its attribution to reduced Fe in annealed samples and the (011) reflection of α-Fe. There were no definitive XRD peaks for Fe_2O_3, Fe_3O_4, $FeCl_3$, or $FeCl_2$ in both series of samples, therefore, more in-depth investigations on Fe speciation were conducted with XANES, discussed in Section 3.4.2.

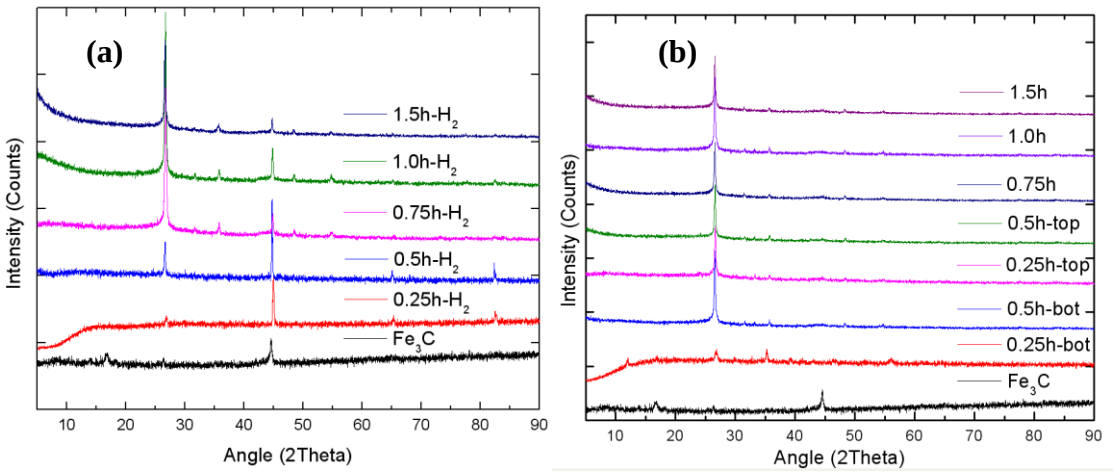

Figure 3.3. XRD patterns of (a) annealed Fe_3C-CDCs and (b) unannealed Fe_3C-CDCs

For more insight into the pore structure, Quench Solid Density Functional Theory (QSDFT) calculations were carried out and pore size distributions for annealed samples are presented in **Figure 3.4**. The QSDFT model is a quantitative model designed for

curved, non-homogenous surface geometries, and can be used to accurately describe CDC porosimetry.[43] Due to the cavitation effect, the adsorption branch of the N_2-isotherm was applied.[44] A slit-pore and cylindrical pore model were used in the QSDFT model to account for the hysteresis and the degree of graphitization within the samples, which are both indicative of significant mesoporosity. In **Figure 3.4(a)**, all pore size distribution plots have similar shapes, with a distinct micropore diameter of 9Å. The peak area increases with the total amount of N_2 adsorbed, and levels off near complete conversion at chlorination times $\geq$ 0.75h. There is a broad development of mesopores with an average diameter of 4 nm seen at chlorination times $\geq$ 0.75h. The increase in mesoporosity is consistent with the increase in graphite crystallinity seen in XRD, and is likely due to increased ordering at longer reaction times, as well as an increase in overall porosity. It is common for graphitized carbide-derived carbons to exhibit more mesoporosity.

In **Figure 3.4(b)**, different porosity characteristics are seen for the top and bottom unannealed samples. Top layer CDCs are more closely aligned with annealed samples, and feature a microporous peak at 13Å in diameter, as well as mesopores of around 3.4 nm in diameter. Bottom layer CDCs are more mesoporous, with most pores greater than 5 nm in diameter and a broad range of mesopores up to 20 nm in diameter. The 0.25h-bot sample has characteristics of both 0.25h-top and 0.5h-bot, suggesting it is a mixture of the layers, possibly due to poor layer separation. Further analysis was done to couple these porosity differences with the specific carbon and Fe nanostructures present in the top, bottom, and annealed series of samples.

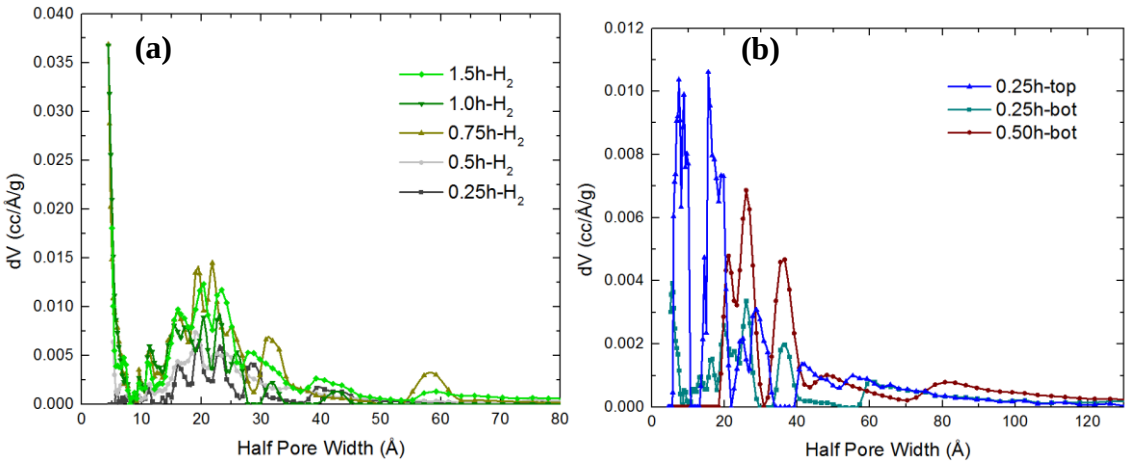

Figure 3.4. Pore size distributions for (a) annealed Fe_3C-CDCs and (b) unannealed Fe_3C-CDCs

3.4.2 Nanostructures obtained from partial chlorination of Fe_3C

3.4.2.1. Nanostructures of Unannealed Fe_3C-CDCs

Representative SEM images of unannealed Fe_3C-CDCs are presented in **Figure 3.5** and **Figure 3.6**. More SEM images are available in the **Appendix B** in **Figures B.2-B.14**. Planar graphitic sheets were observed in all samples, consistent with XRD patterns in **Figure 3.3(b)**. Depending on the chlorination time and layer, vastly different substructures were formed.

Top layers at chlorination times ≥ 0.5h, as seen in **Figure 3.5**, are largely graphitic, disordered, and contain embedded $FeCl_3$ nanoparticles. The XANES spectra in **Figure 3.7(a)** and **Figure 3.7(b)** were used to confirm the oxidation state of the iron. There is a well-established separation of 1.4eV between the Fe^{2+} and Fe^{3+} oxidation states in the pre-edge region, as the position of the pre-edge centroid shifts towards higher energy with an increase in Fe oxidation state.[41] The characteristic pre-edge region at ~7114 eV is indicative of an Fe(III) state, and the pre-edge feature matches very closely with the $FeCl_3$ standard.[45] There is some discrepancy between the 0.25h-top spectra and

the other CDCs, particularly in the white line region but also in the isosbestic point shared by the other CDCs at ~7127 eV. This is likely due to the presence of unreacted iron carbide at low chlorination times. Stoichiometrically, the minimum time required for complete conversion is calculated to be between 45 minutes, assuming complete selectivity to $FeCl_2$ in Equation (2), and 67 minutes, assuming complete selectivity to $FeCl_3$ in Equation (1).

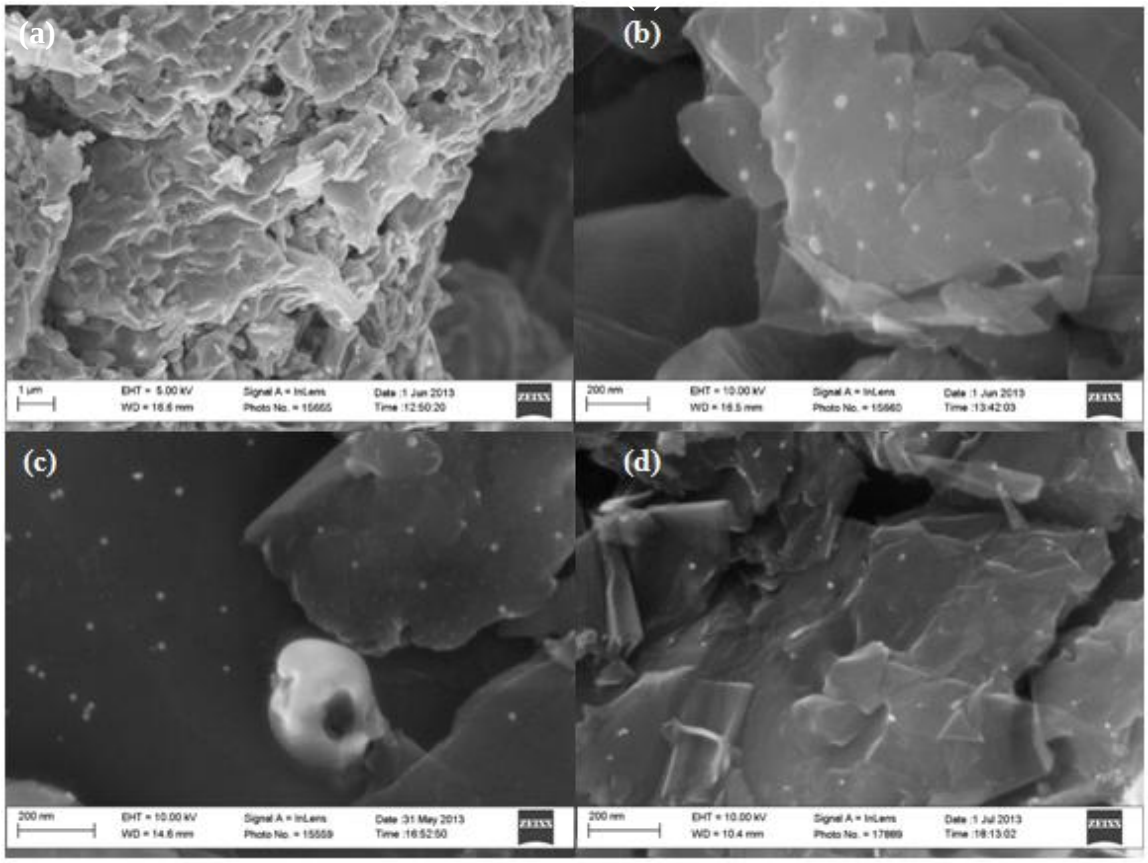

Figure 3.5. SEM Images of (a)(b) 0.5h-top, (c) 0.75h, (d) 1.0h

The presence of $FeCl_3$ is surprising, as its boiling point of 315^{o}C is well below the 600^{o}C chlorination temperature. It is hypothesized that after the surface reaction, $FeCl_3$ products agglomerate as they begin to diffuse through the resulting CDC, and catalyze the formation of carbon nanostructures before entering the bulk gas phase. As previously

stated, the role of $FeCl_3$ as a graphitization catalyst has been seen in the formation of graphitic carbon nanospheres, amorphous carbon nanotubes, and well-ordered graphite where $FeCl_3$ is hypothesized to transport carbon and facilitate graphitization.[29-31] In the chlorination of ferrocene, carbon nanostructures are thought to prevent $FeCl_3$ sublimation until it is reduced to $FeCl_2$.

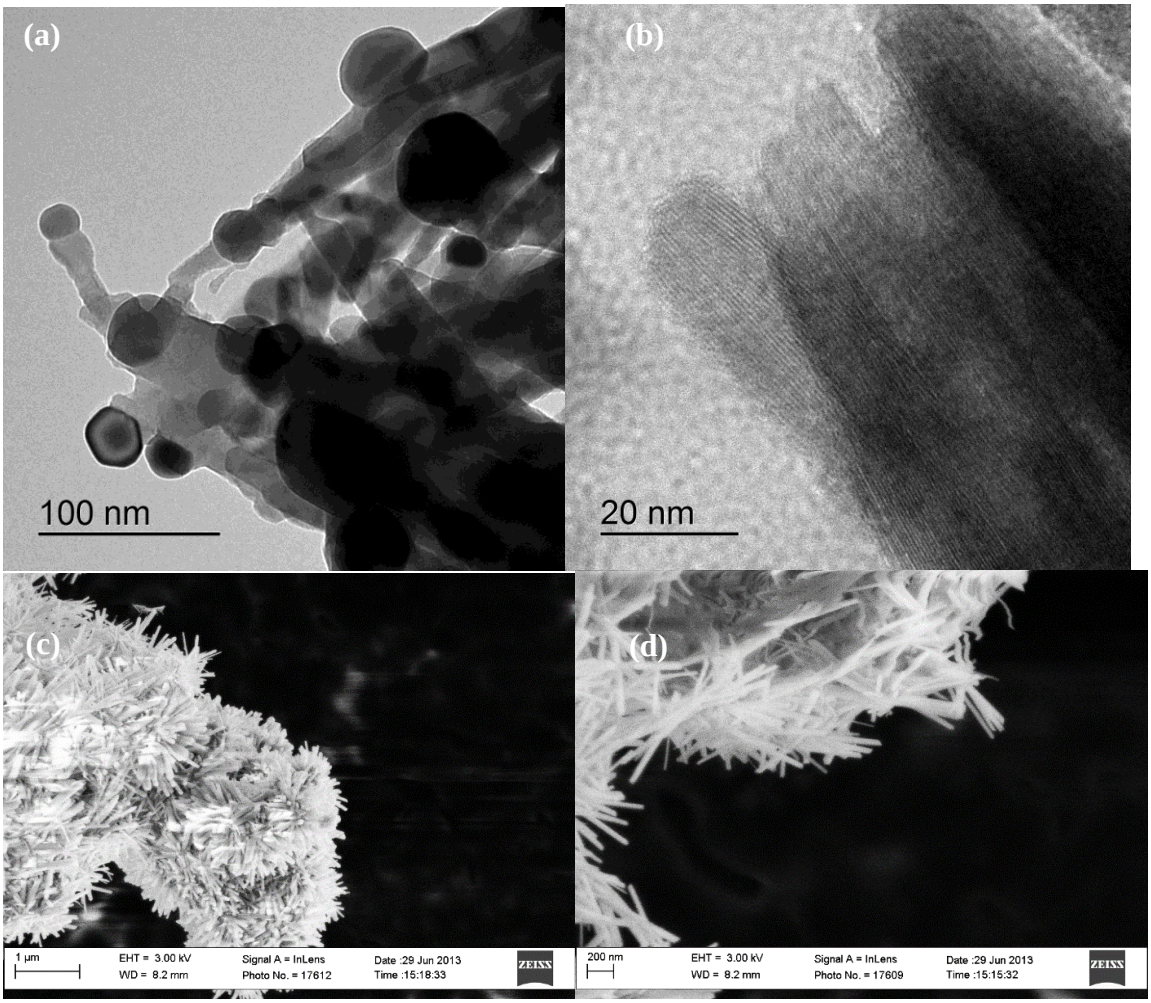

Figure 3.6. TEM and SEM Images of 0.5h-bot

The decomposition of $FeCl_3$ occurs by either the vaporization of $FeCl_3$ or the dimer Fe_2Cl_6. The dimer is reported to be the dominant species as high as 400^oC.[46,47] A thermodynamic study of the chlorination of Fe_3C by Gogotsi et al. have also shown significant amounts of Fe_2Cl_6 at equilibrium at 600^oC.[29] $FeCl_3$ and Fe_2Cl_6 have D3h and

D2h symmetry, respectively and the size of Fe_2Cl_6 is 0.502 nm long by 0.379 nm wide, while $FeCl_3$ can be calculated to be 0.318 nm long from the equilibrium bond length of 0.2122 nm.[48, 49] Given the size and shape of $FeCl_3$ and Fe_2Cl_6, it is plausible that they are sterically prevented from escaping by graphitic carbon nanostructures. The diffusion of $FeCl_3$ decomposition species are hypothesized to be inherently slow and hindered by graphitic carbon nanostructures, as a sample chlorinated at 3 hours contained less than 1% residual Fe. A similar phenomenon has recently been observed for the chlorination of TiC nanopowders, where residual TiC is postulated to be preserved due to surrounding graphitic carbon nanostructures that prevent chlorine diffusion.[50] Later, in annealed samples, graphite layers are seen surrounding a reduced Fe particle, further supporting this theory.

Different substructures were observed at lower chlorination times for each layer. The 0.25h-top sample shows the presence of small tubular structures approximately 200-400nm in length in **Figure A.2** and planar graphitic sheets can be seen in the 0.25h-bot sample, as well as Fe nanoparticles in **Figure A.4**. Due to charging effects, however, we were unable to increase magnification for a closer look without adding excessive noise to the detector signal. At 0.5h chlorination time, there is a more pronounced difference between the top and bottom layers. In **Figure 3.6**, 0.5h-bot sample SEM and TEM images are shown. Rod-like structures were observed in the 0.5h-bot sample, with diameters ranging from ~30-50nm and lengths up to 10μm. This was further investigated in TEM. It has been suggested that $FeCl_3$ can facilitate carbon dissolution, which is responsible for the creation of amorphous hollow carbon nanotubes upon the chlorination of ferrocene.[24, 30] The contrast difference between the tubular structure and the tip in

Figure 3.6(a) greatly supports $FeCl_3$ catalyzed carbon nanotube formation in the bottom sample. **Figure 3.6(b)** shows many joined structures with domains that have an observed lattice parameter of 7Å, on the order of a unit cell and much larger than the d-spacing of a graphitic carbon nanotube (3.4Å). It is heavily supported from the XANES spectra in **Figure 3.7(b)** that this sample contains predominantly $FeCl_2$, and these are suggested to be needle-like $FeCl_2$ structures. In **Figure 3.7(b)**, samples have a pre-edge transition of ~7112.1eV, which is indicative of the Fe^{2+} oxidation state. In addition, both samples match the same double peak white line and post-edge features of the $FeCl_2$ standard spectrum.

Significant amounts of residual $FeCl_2$ in the bottom layer samples are unexpected, as a previous thermodynamic study of the chlorination of Fe_3C by Gogotsi et al. showed that only small amounts of $FeCl_2$ could be produced at low chlorine concentrations.[29] It is possible that the formation of $FeCl_2$ in Fe_3C follows the same mechanism proposed for the chlorination of ferrocene.[31, 33] $FeCl_2$ was not supported as an initial product for the chlorination of ferrocene, and is suggested to form via the reduction of $FeCl_3$.[29, 30] Carbon nanostructures would consequently encapsulate the crystalline $FeCl_2$ to prevent oxidization by excess Cl_2. It is interesting that the bottom layer is no longer seen at longer chlorination times. The melting point and boiling point for $FeCl_2$ are 676^{o}C and 1020^{o}C, and $FeCl_2$ has a low vapor pressure at 600^{o}C.[46, 47] Intuitively, $FeCl_2$ could be further oxidized to $FeCl_3$, which slowly diffuses to the bulk phase.

These results show marked differences for Fe_3C-CDCs compared to other CDCs in terms of both metal dispersion and speciation. Kinetic studies with SiC have suggested a layer-by-layer extraction of Si, while the extraction of Fe results in dispersed residual

iron chloride domains.[5, 32] Studies with WC, NbC, SiC, and TiC have observed that when the extraction process has not proceeded to completion, the residual metal is largely in unreacted carbide form. In **Table 3.1** and **Figure 3.7**, it is shown that 0.5h-H_2 features 25.5% residual iron which is present as $FeCl_2$ and $FeCl_3$ in 0.5h-top and 0.5h-bot samples before reduced during annealing treatment.[9, 11, 32, 33]

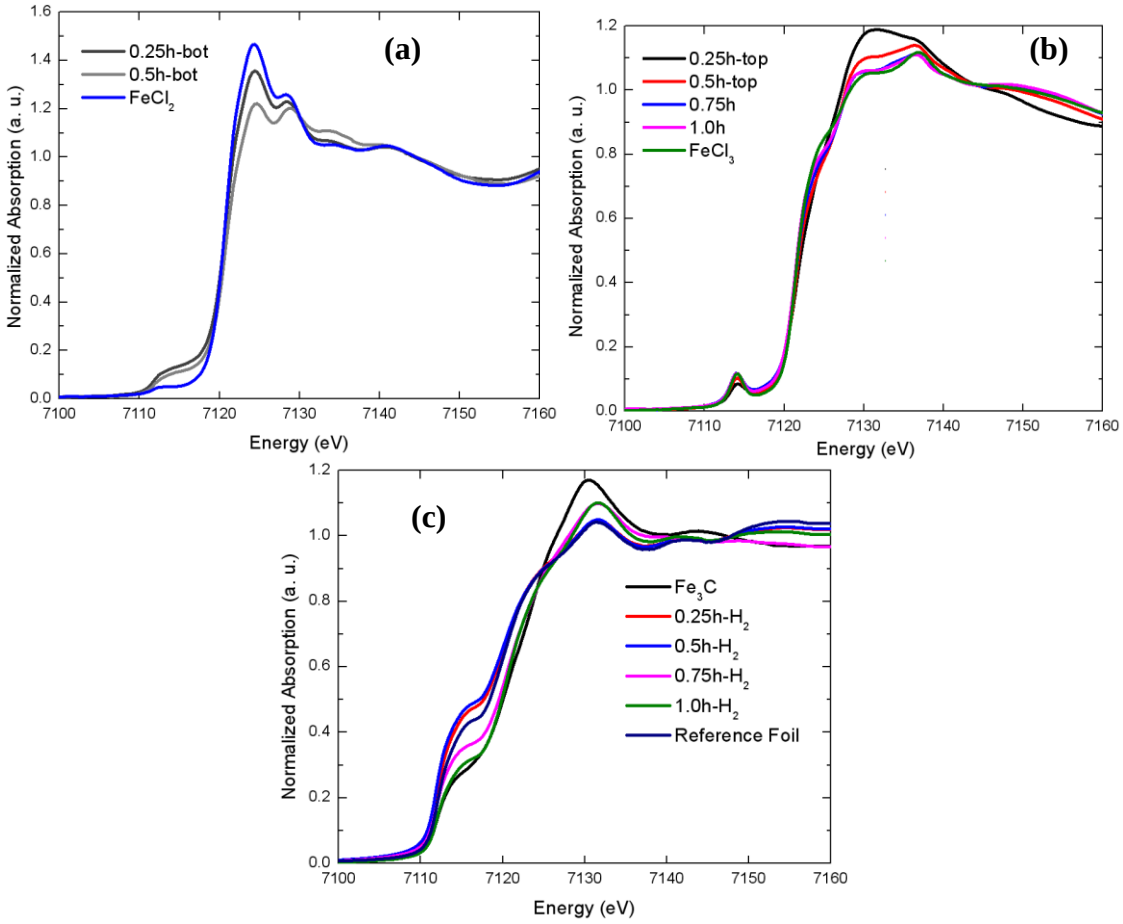

Figure 3.7. Fe-K edge for (a) unannealed bottom layer Fe_3C-CDCs, (b) unannealed top layer Fe_3C-CDCs, and (c) annealed Fe_3C-CDCs

3.4.2.2. Nanostructures of Annealed Fe_3C-CDCs

Representative SEM and TEM images of annealed Fe_3C-CDCs are presented in **Figure 3.8** and XANES spectrum for annealed samples are present in **Figure 3.7(c)**. A high degree of graphitic ordering is seen in all annealed samples, consistent with the

intense (002) reflection of graphite in the XRD spectrum in **Figure 3.3(a)**. X-ray diffraction spectra for annealed samples show a steep (100) reflection for α-Fe at 45^{o}, indicating H_2 annealing reacts with metal chlorides and removes chloride species. Dispersed within the observed planar graphitic crystals are Fe nanoparticles with diameters ranging from 5-100nm.

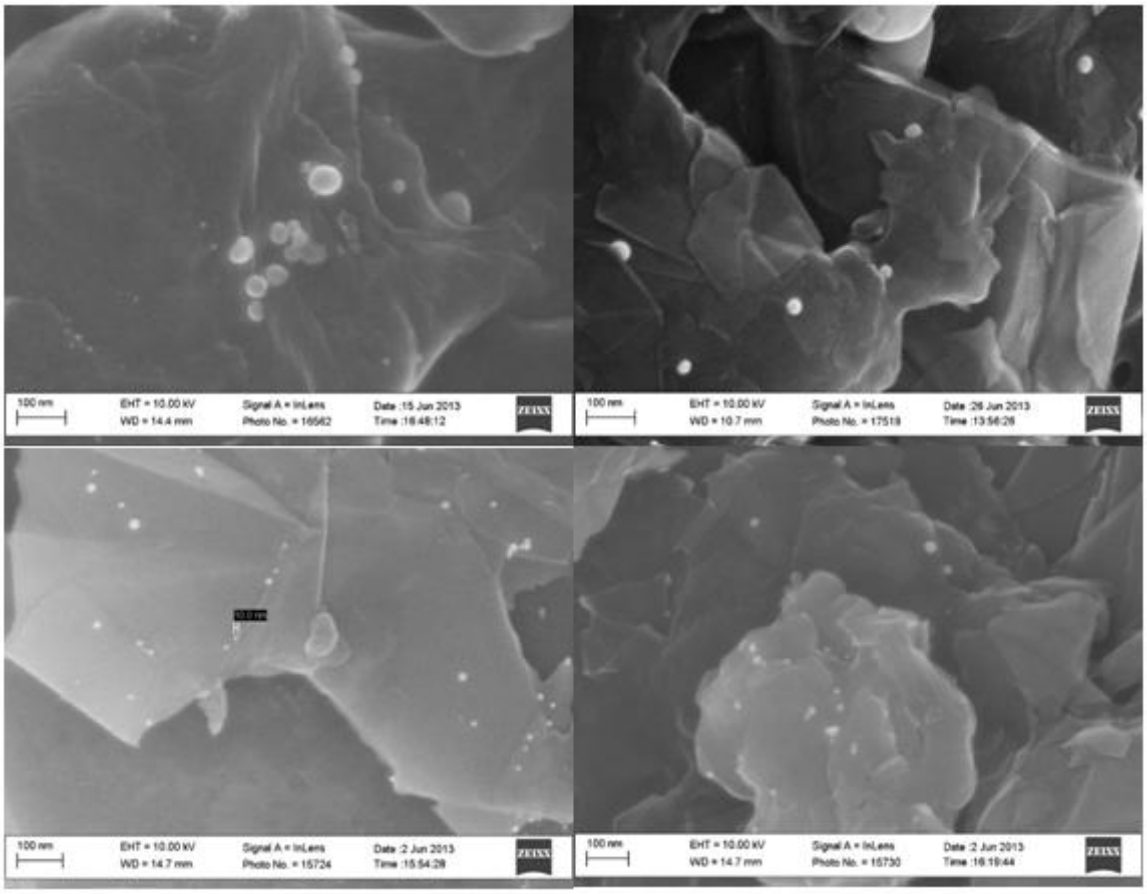

Figure 3.8. SEM Images of (a) 0.25h-H_2, (b) 0.5h-H_2, (c) 0.75h-H_2, (d) 1.0h-H_2

Particle size distribution versus chlorination time was calculated for annealed samples, and the results are summarized in **Figure 3.10**. Mean particle size decreases with increasing chlorination time, and almost all particles are less than 10nm in diameter at chlorination times ≥ 0.75h. This suggests that > 10nm Fe particles are mainly derived from reduced $FeCl_2$ species in the bottom layer, and upon annealing treatment they are

partially or fully removed along with the disappearance of the carbon nanotubes. Upon chlorination times ≥0.75h, after the disappearance of the bottom layer, only <10nm particles are present. Low resolution TEM images in **Figure 3.9(a)** and high resolution TEM images in **Figure 3.9(b)** further suggest that these particles are embedded within the CDC framework. HRTEM shows that there are evident graphitic sheets that envelope the Fe nanoparticle, supporting the hypothesis that these graphitic nanostructures prevent the sublimation of iron chloride species during chlorination.

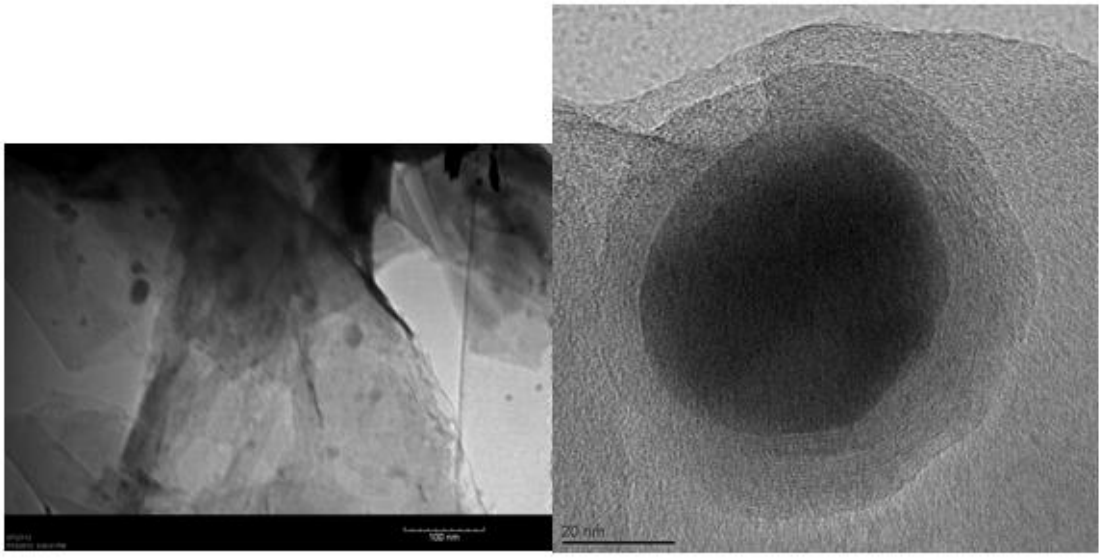

Figure 3.9. TEM Images of 1.0h-H_2

XANES spectra for the annealed Fe_3C-CDCs in **Figure 3.7(c)** also confirm metallic Fe is present in the annealed samples, and closely match the Fe reference foil spectrum. Therefore, iron chloride species present in unannealed samples are seen to be easily reduced to metallic Fe for catalytic applications. It is important to note that there is a significantly higher white line for Fe_3C precursor compared to annealed Fe_3C-CDCs and the reference foil. This is likely due to mild surface oxidation on the Fe_3C precursor, which can result from a common passivation treatment at the end of Fe_3C synthesis that

requires exposure to dilute O_2 to create a non-reactive surface on the freshly prepared carbide.[24]

The successful reduction of $FeCl_3$ particles during the annealing treatment demonstrates that there is some selective accessibility between the bulk gas phase and the trapped iron chloride nanoparticles. For instance, during the annealing treatment, for the case of longer chlorination time samples which contain $FeCl_3$ nanoparticles, H_2 gas is able to diffuse into a trapped $FeCl_3$ particle, reduces the particle to metallic Fe, and HCl gas is able to diffuse back out to the bulk phase. We believe that the size and shape differences between H_2 and HCl and the iron chloride decomposition species explain this behavior. The kinetic diameters of H_2 and HCl are quite small, 0.289 nm and 0.442 nm, and the linear shape of these gases offers much less steric hinderance than molecules with D3h and D2h point groups.

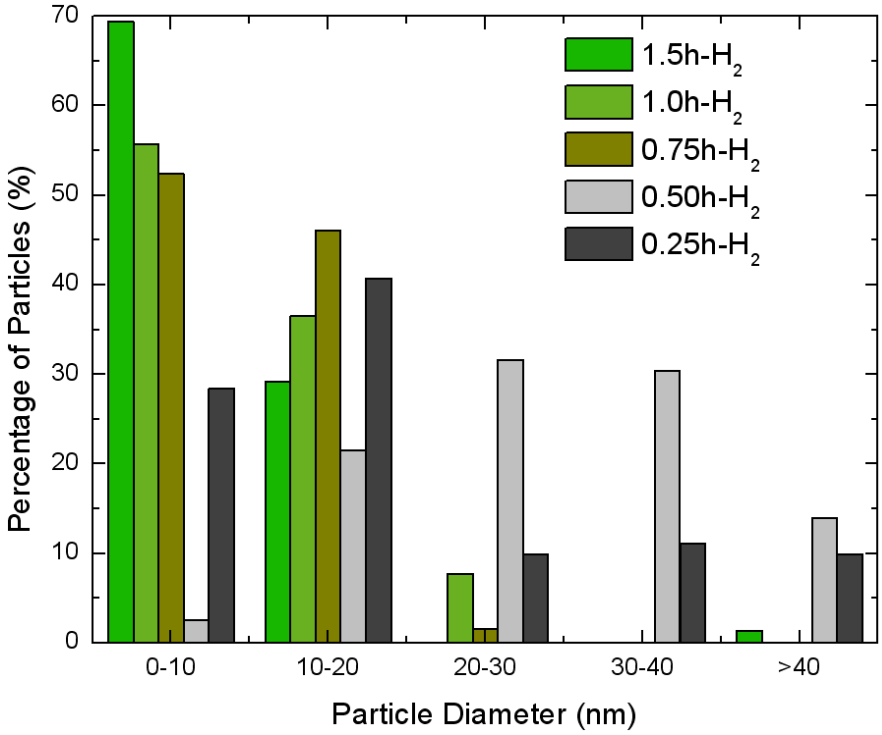

Figure 3.10. Particle size distributions for Fe nanoparticles in annealed Fe_3C-CDCs

3.5 Conclusions

Fe_3C-CDCs were synthesized at 600^oC at various chlorination times to study their porosity and residual metal characteristics. At low chlorination times, XANES analysis shows two distinct layers form with different $FeCl_x$ oxidation states: A porous layer containing $FeCl_3$ forms on top of unannealed samples, and a significantly less porous layer containing $FeCl_2$ forms on the bottom of unannealed samples. Unique structures are formed for each layer – with notable carbon nanotubes of ~30-50nm diameters in the bottom layer. Annealed Fe_3C-CDCs form mainly planar graphitic sheets with embedded Fe particles.

The present study clearly shows that the chlorination of Fe_3C at 600^oC does not follow a traditional layer-by-layer extraction of Fe from the carbide matrix. After the surface reaction of chlorine with iron carbide, a significant percentage of $FeCl_2$ and $FeCl_3$ products do not diffuse out of the resulting carbide-derived carbon, and are able to agglomerate and catalyze the formation of graphitic carbon nanostructures. These graphitic carbon nanostructures prevent the diffusion of vaporized iron chloride species and their decomposition products, and allow iron chloride species to remain as supported nanoparticles. This is a marked difference from traditional layer-by-layer extraction, in which the chloride products would diffuse out of the carbide-derived carbon into the bulk gas phase.

There are many attractive features of these retained iron chloride species. These nanoparticles can subsequently be reduced in H_2 and approach an average Fe nanoparticle size of 10 nm. Fe_3C-CDCs can be synthesized with specific surface areas and pore volumes approaching 700 $m^2\ g^{-1}$ and 0.54 $cm^3\ g^{-1}$, and a high degree of microporosity,

which renders them as good supports for catalytic and filtration applications. Theoretically, these materials can also be calcined to allow for Fe oxide sites and thus be further tailored for desired sorbate-sorbent interactions. These results provide a new strategy for a facile, one pot synthesis for supported Fe nanoparticles in CDC materials.

3.6 References

[1] Joo SH, Choi SJ, Oh I, Kwak J, Liu Z, Terasaki O, et al. Ordered nanoporous arrays of carbon supporting high dispersions of platinum nanoparticles. Nature. 2001;412(6843):169-72.

[2] Gogotsi Y, Nikitin A, Ye H, Zhou W, Fischer JE, Yi B, et al. Nanoporous carbide-derived carbon with tunable pore size. Nat Mater. 2003;2(9):591-4.

[3] Lee J, Han S, Hyeon T. Synthesis of new nanoporous carbon materials using nanostructured silica materials as templates. Journal of Materials Chemistry. 2004;14(4):478-86.

[4] Shenderova OA, Zhirnov VV, Brenner DW. Carbon Nanostructures. Critical Reviews in Solid State and Materials Sciences. 2002;27(3-4):227-356.

[5] Allen L, Ranyi Z, McNallan M. Kinetics of conversion of silicon carbide to carbide derived carbon. Journal of Physics: Condensed Matter. 2006;18(32):S1763.

[6] Hoffman EN, Yushin G, El-Raghy T, Gogotsi Y, Barsoum MW. Micro and mesoporosity of carbon derived from ternary and binary metal carbides. Microporous and Mesoporous Materials. 2008;112(1-3):526-32.

[7] Kim HS, Singer JP, Gogotsi Y, Fischer JE. Molybdenum carbide-derived carbon for hydrogen storage. Microporous and Mesoporous Materials. 2009;120(3):267-71.

[8] Presser V, Heon M, Gogotsi Y. Carbide-Derived Carbons - From Porous Networks to Nanotubes and Graphene. Advanced Functional Materials. 2011;21(5):810-33.

[9] Tallo I, Thomberg T, Kontturi K, Jänes A, Lust E. Nanostructured carbide-derived carbon synthesized by chlorination of tungsten carbide. Carbon. 2011;49(13):4427-33.

[10] Dash RK, Yushin G, Gogotsi Y. Synthesis, structure and porosity analysis of microporous and mesoporous carbon derived from zirconium carbide. Microporous and Mesoporous Materials. 2005;86(1-3):50-7.

[11] Dash R, Chmiola J, Yushin G, Gogotsi Y, Laudisio G, Singer J, et al. Titanium carbide derived nanoporous carbon for energy-related applications. Carbon. 2006;44(12):2489-97.

[12] Jänes A, Thomberg T, Lust E. Synthesis and characterisation of nanoporous carbide-derived carbon by chlorination of vanadium carbide. Carbon. 2007;45(14):2717-22.

[13] Borchardt L, Hasché F, Lohe MR, Oschatz M, Schmidt F, Kockrick E, et al. Transition metal loaded silicon carbide-derived carbons with enhanced catalytic properties. Carbon. 2012;50(5):1861-70.

[14] Zheng L, Wang Y, Wang X, Wang X, An H, Yi L. The effects of surface modification on the supercapacitive behaviors of carbon derived from calcium carbide. Journal of Materials Science. 2010;45(22):6030-7.

[15] Seredych M, Portet C, Gogotsi Y, Bandosz TJ. Nitrogen modified carbide-derived carbons as adsorbents of hydrogen sulfide. J Colloid Interface Sci. 2009;330(1):60-6.

[16] Kockrick E, Schrage C, Borchardt L, Klein N, Rose M, Senkovska I, et al. Ordered mesoporous carbide derived carbons for high pressure gas storage. Carbon. 2010;48(6):1707-17.

[17] Krawiec P, Kockrick E, Borchardt L, Geiger D, Corma A, Kaskel S. Ordered Mesoporous Carbide Derived Carbons: Novel Materials for Catalysis and Adsorption. The Journal of Physical Chemistry C. 2009;113(18):7755-61.

[18] Stein A, Wang Z, Fierke MA. Functionalization of Porous Carbon Materials with Designed Pore Architecture. Advanced Materials. 2009;21(3):265-93.

[19] Yang Y, Tang L, Burke N, Chiang K. Nanoporous carbon supported metal particles: their synthesis and characterisation. Journal of Nanoparticle Research. 2012;14(8):1-12.

[20] Kockrick E, Borchardt L, Schrage C, Gaudillere C, Ziegler C, Freudenberg T, et al. CeO2/Pt Catalyst Nanoparticle Containing Carbide-Derived Carbon Composites by a New In situ Functionalization Strategy. Chemistry of Materials. 2010;23(1):57-66.

[21] White RJ, Luque R, Budarin VL, Clark JH, Macquarrie DJ. Supported metal nanoparticles on porous materials. Methods and applications. Chemical Society Reviews. 2009;38(2):481-94.

[22] Long JW, Laskoski M, Peterson GW, Keller TM, Pettigrew KA, Schindler BJ. Metal-catalyzed graphitic nanostructures as sorbents for vapor-phase ammonia. Journal of Materials Chemistry. 2011;21(10):3477-84.

[23] Rufino B, Mazerat S, Couvrat M, Lorrette C, Maskrot H, Pailler R. The effect of particle size on the formation and structure of carbide-derived carbon on β-SiC nanoparticles by reaction with chlorine. Carbon. 2011;49(9):3073-83.

[24] Ávila-Brande D, Urones-Garrote E, Katcho NA, Lomba E, Gómez-Herrero A, Landa-Cánovas ÁR, et al. Electron microscopy characterization of nanostructured carbon obtained from chlorination of metallocenes and metal carbides. Micron. 2007;38(4):335-45.

[25] Jeong J-H, Bae H-T, Lim D-S. The effect of iron catalysts on the microstructure and tribological properties of carbide-derived carbon. Carbon. 2010;48(12):3628-34.

[26] Perkson A, Leis J, Arulepp M, Käärik M, Urbonaite S, Svensson G. Barrel-like carbon nanoparticles from carbide by catalyst assisted chlorination. Carbon. 2003;41(9):1729-35.

[27] Leis J, Perkson A, Arulepp M, Nigu P, Svensson G. Catalytic effects of metals of the iron subgroup on the chlorination of titanium carbide to form nanostructural carbon. Carbon. 2002;40(9):1559-64.

[28] Xu J, Zhang RJ, Wang JX, Ge SH, Zhou HC, Liu Y, et al. Effective control of the microstructure of carbide-derived carbon by ball-milling the carbide precursor. Carbon. 2013;52:499-508.

[29] Katcho NA, Urones-Garrote E, Ávila-Brande D, Gómez-Herrero A, Urbonaite S, Csillag S, et al. Carbon Hollow Nanospheres from Chlorination of Ferrocene. Chemistry of Materials. 2007;19(9):2304-9.

[30] Urones-Garrote E, Ávila-Brande D, Ayape-Katcho N, Gómez-Herrero A, Landa-Cánovas AR, Otero-Díaz LC. Amorphous carbon nanostructures from chlorination of ferrocene. Carbon. 2005;43(5):978-85.

[31] Dimovski S, Nikitin A, Ye H, Gogotsi Y. Synthesis of graphite by chlorination of iron carbide at moderate temperatures. Journal of Materials Chemistry. 2004;14(2):238-43.

[32] Dimovski S, Nikitin A, Ye H, Gogotsi Y. Low Temperature synthesis of graphite from iron carbide. In: Barsukov I, Johnson C, Doninger J, Barsukov V, eds. New Carbon Based Materials for Electrochemical Energy Storage Systems: Batteries, Supercapacitors and Fuel Cells: Springer Netherlands 2006, p. 399-410.

[33] Schuth F, Palkovits R, Schlogl R, Su DS. Ammonia as a possible element in an energy infrastructure: catalysts for ammonia decomposition. Energy & Environmental Science. 2012;5(4):6278-89.

[34] Li SZ, O'Brien RJ, Meitzner GD, Hamdeh H, Davis BH, Iglesia E. Structural analysis of unpromoted Fe-based Fischer-Tropsch catalysts using X-ray absorption spectroscopy. Applied Catalysis a-General. 2001;219(1-2):215-22.

[35] Ravel B, Newville M, Athena, Artemis, Hephaestus: data analysis for X-ray absorption spectroscopy using IFEFFIT. Journal of Synchrotron Radiation. 2005;12:537-42.

[36] Brunauer S, Deming LS, Deming WE, Teller E. On a theory of the van der Waals adsorption of gases. Journal of the American Chemical Society. 1940;62:1723-32.

[37] Brunauer S, Emmett PH, Teller E. Adsorption of gases in multimolecular layers. Journal of the American Chemical Society. 1938;60:309-19.

[38] Kruk M, Jaroniec M. Gas adsorption characterization of ordered organic-inorganic nanocomposite materials. Chemistry of Materials. 2001;13(10):3169-83.

[39] Kleitz F, Bérubé Fo, Guillet-Nicolas Rm, Yang C-M, Thommes M. Probing Adsorption, Pore Condensation, and Hysteresis Behavior of Pure Fluids in Three-Dimensional Cubic Mesoporous KIT-6 Silica. The Journal of Physical Chemistry C. 2010;114(20):9344-55.

[40] Rasmussen CJ, Vishnyakov A, Thommes M, Smarsly BM, Kleitz F, Neimark AV. Cavitation in Metastable Liquid Nitrogen Confined to Nanoscale Pores. Langmuir. 2010;26(12):10147-57.

[41] Thommes M, Smarsly B, Groenewolt M, Ravikovitch PI, Neimark AV. Adsorption Hysteresis of Nitrogen and Argon in Pore Networks and Characterization of Novel Micro- and Mesoporous Silicas. Langmuir. 2005;22(2):756-64.

[42] Portet C, Kazachkin D, Osswald S, Gogotsi Y, Borguet E. Impact of synthesis conditions on surface chemistry and structure of carbide-derived carbons. Thermochimica Acta. 2010;497(1-2):137-42.

[43] Neimark AV, Lin YZ, Ravikovitch PI, Thommes M. Quenched solid density functional theory and pore size analysis of micro-mesoporous carbons. Carbon. 2009;47(7):1617-28.

[44] Landers J, Gennady YG, Neimark AV. Density functional theory methods for characterization of porous materials. Colloids and Surfaces A: Physicochem. Eng. Aspects 2013;437(20):3-32.

[45] Wilke M, Farges F, Petit PE, Brown GE, Martin F. Oxidation state and coordination of Fe in minerals: An FeK-XANES spectroscopic study. American Mineralogist. 2001;86(5-6):714-30.

[46] Nalbandian L, Papatheodorou GN, Raman Spectra of the Vapor Molecules Fe2Cl6, FeCl3, and FeAlCl6. High Temperature Science. 1990;28(1):49-65.

[47] Holleman A, Wiberg E. Inorganic Chemistry. San Diego: Academic Press; 2001, p. 1442.

[48] Zaikov GE, Mikheev, YA. Kinetics and Mechanisms of Chemical Reactions. New York: Nova Publishers; 2005, p. 74.

[49] Varga Zn, Kolonits Mr, Hargittai M. Gas-Phase Structures of Iron Trihalides: A Computational Study of all Iron Trihalides and an Electron Diffraction Study of Iron Trichloride. Inorganic Chemistry. 2010;49(3):1039-45.

[50] Pérez CR, Yeon S-H, Ségalini J, Presser V, Taberna P-L, Simon P, et al. Structure and Electrochemical Performance of Carbide-Derived Carbon Nanopowders. Advanced Functional Materials. 2013;23(8):1081-9.

CHAPTER 4

TAILORED FE3C-DERIVED CARBONS FOR AMMONIA FILTRATION

4.1 Summary

Carbide-derived carbons are synthesized by chlorination of Fe_3C at temperatures ranging from 200-1000 ^oC. The complex extraction method of Fe from Fe_3C at moderate temperatures (600 ^oC) allows for the tailored inclusion of $FeCl_2$, $FeCl_3$, or Fe nanoparticles in the resulting CDC by controlling the synthesis conditions and post-treatment methods. In this study, we extend the synthesis to other temperatures in order to understand the role of chlorination temperature on the physical and textural properties of the resulting CDC. We also examine the activity of Fe_3C-CDCs with embedded $FeCl_3$ nanoparticles for ammonia adsorption. Materials synthesized at 600 ^oC show exceptional results in ammonia breakthrough experiments, and achieved dynamic loadings of 1.88 mmol g^{-1} at 0% relative humidity and 3.44 mmol g^{-1} at 75% relative humidity calculated at initial breakthrough when $[NH_3] > 0$ ppm. NH_3 temperature programmed desorption (NH_3-TPD) and Fourier Transform Infrared Spectroscopy (FTIR) experiments suggest that the uptake is primarily due to ammonia complexation with $FeCl_3$ nanoparticles under dry conditions, and additional interactions with trapped chlorine in the presence of water.

4.2 Introduction

Porous carbons have long seen pervasive use within the gas separation and purification industries due to their low cost, wide chemical and thermal stability, and high bulk porosity. Their exceptionally high surface areas allow for a large density of

adsorptive sites, while chemical and physical activation of porous carbons permits tailorability of the pore size for higher performance and gas selectivity. The control over the pore size is especially important for applications involving small gases, which are more efficiently adsorbed in pores with diameters similar to their kinetic diameter. This has driven a lot of research over the past several decades towards new synthesis approaches for carbons with specific mesoporous (2-50 nm) and microporous (< 2 nm) architectures.[1, 2]

For high vapor pressure gases, physisorption interactions are typically not strong enough to promote high adsorption loadings. As a result, many small, high vapor pressure toxic industrial chemicals (TICs), such as H_2S, SO_2, and NH_3 are of primary concern for emergency and military personnel due to their high toxicity and inability to be effectively removed by many adsorbents. The removal of NH_3 from air is particularly important due to its pervasive use in the fertilizer and waste treatment industries, as well as its low permissible exposure limit (PEL) of 50 ppm.[3] Recent studies on carbonaceous materials highlight the need for a small pore size as well as increased surface acidity through the addition of functional groups and metal oxides for effective removal of NH_3.[4-9] For dynamic applications, such as respiratory protection, bulk porosity plays less of a role when compared to the density and strength of surface groups available in small pores. This is demonstrated in the efficacy of graphite oxide, which was shown to have exceptionally high dynamic ammonia capacity due to the presence of oxygen groups between expanded graphitic sheets between 6 and 12 Å in diameter.[8-10]

Carbide-derived carbons (CDCs) are a relatively new class of porous carbons that feature extremely tailorable physical properties.[11, 12] These materials are produced

through the selective extraction of a metal or heteroatom from a carbide precursor, commonly by chlorination. Modification of the chlorination temperature, as well as careful choice of the carbide precursor, can result in sub-angstrom control of pore size with narrow pore size distributions.[13-16] The resulting nanoporous carbon also exhibits large specific surface areas and a high degree of microporosity, with a majority of the pores less than 1 nm in diameter for various carbides after chlorination.[15, 16] Unsurprisingly, these materials have shown exceptional results in the adsorption of small gases including H_2, CO_2, and CH_4.[17-19] Further functionalization of these materials with metal nanoparticles and active surface groups is of great interest to complement their tunable physical properties.[20-22] For example, in studies with H_2S, SiC-CDC has been successfully modified with nitrogen-containing groups to greatly enhance its dynamic capacity.[23]

Recently, we showed that the chlorination of iron carbide at 600 ^oC results in iron carbide-derived carbons (Fe_3C-CDCs) with retained Fe nanoparticles[24] due to a more complex Fe extraction mechanism when compared to the selective removal of other metal atoms from their respective carbides. Instead of a layer-by-layer extraction, it was shown that a large percentage of iron (II) or (III) chloride products were retained. It was hypothesized that these chlorides catalyze the formation of graphitic nanostructures, which hinder their removal. As a result, well-dispersed iron chloride nanoparticles were observed on Fe_3C-CDCs with an average particle size approaching 10 nm at longer chlorination times.[24] Furthermore, during hydrogen annealing, the Fe is converted to metallic iron nanoparticles proving that the residual iron is tailorable and accessible to small gases.

In this study, we further demonstrate that the residual iron is accessible and able to interact with target gases in adsorption separation applications. Unannealed Fe_3C-CDCs, featuring embedded $FeCl_3$ nanoparticles, are evaluated and determined to be effective NH_3 adsorbents. Annealed Fe_3C-CDCs are also synthesized at various chlorination temperatures to understand the tunability of their pore size and maximum bulk porosity over possible synthesis conditions. Design rules are provided to guide future synthesis of these materials with both tailored physical and chemical characteristic, with respect to their pore size distributions and residual metal content and form. The specific sorbent-sorbate interactions between NH_3 and unannealed Fe_3C-CDCs with included well-dispersed iron chloride nanoparticles are also investigated. Special attention is paid to textural and structural differences between annealed Fe_3C-CDC samples prepared in this study and unannealed Fe_3C-CDCs in a previous study, which adds insight into the complex extraction mechanism of Fe from Fe_3C and the role of retained iron chloride species.

4.3 Materials and Methods

4.3.1 Materials

One gram of a commercially available Fe_3C (F. J. Brodmann & Co. 99.5% purity -200/+275 mesh) was placed on a quartz boat and inserted into a quartz tube of ID 1", length 20" and into a horizontal tube furnace. Samples were heated to a reaction temperature ranging from 200-1000 ^oC at a ramp rate of 5 $^oC\ min^{-1}$ under Ar flow (Airgas 99.999%) at a rate of 100 ml min^{-1} and at ambient pressure. After reaching the desired chlorination temperature, chlorine gas (Airgas 99.5%) flow was introduced into the reactor at a flow rate of 25 ml min^{-1} for 2 hours, while the Ar flow was maintained. A

scrubber solution of concentrated NaOH was used to neutralize acidic gases present in the effluent stream (Cl_2, HCl, iron chlorides).

After the chlorination time had elapsed the chlorine gas flow was turned off and samples were cooled to 600 ^oC at a ramp rate of 5 ^oC min^{-1} under Ar flow. The Ar flow was then switched to 5% H_2 in Argon (99.999%) at a rate of 100 ml min^{-1} for 3 hours at 600 ^oC to remove residual chlorine and reduce residual metal chlorides. Afterwards, these samples were cooled to room temperature under Ar flow. These samples are referred to as "annealed" iron carbide derived carbons and are labeled as Fe_3C-CDC-CT-H_2, where CT denotes the chlorination temperature and the H_2 denotes exposure to hydrogen. Samples referred to as "unannealed" carbide-derived carbons follow the same synthesis procedure as above but are not treated with H_2 and are simply cooled down to room temperature after chlorination. These samples are chlorinated at 600 ^oC and labeled as Fe_3C-CDC-CT-T, where T represents the chlorination time. The Fe_3C-CDC prefix is dropped in subsequent figures and throughout this chapter for brevity.

4.3.2 Methods

Power X-ray diffraction (PXRD) patterns were collected using an X'Pert X-ray PANalytical diffractometer with a Cu Kα X-ray source (λ = 1.5418 Å). PXRD diffractograms were collected from a range of 4-90^o in two theta (2θ) with a step size of 0.02^o. All experiments were carried out at room temperature. Nitrogen adsorption measurements were obtained on a Quadrasorb Surface Area Analyzer from Quantachrome Instruments. Isotherms were collected at 77 K using a sample of 30-50 mg. Prior to each isotherm, samples were activated overnight at 423 K under vacuum. Specific surface areas were calculated using the BET model over the pressure range 0.01-

0.05 P/P_0. Pore size distributions for all samples were obtained using the Quenched Solid Density Functional Theory (QSDFT) model built into version 5.11 QuadraWin™ software. The QSDFT parameters were selected depending on the characteristics of the isotherm. For microporous, type I isotherms, a slit-pore model, nitrogen adsorbate, and carbon adsorbent were assumed for the QSDFT model. Whereas, for type IV isotherms that exhibit characteristic cavitation effects, an adsorption branch slit-pore/cylindrical pore model was used with an assumed nitrogen adsorbate and carbon adsorbent.

Raman spectra were obtained on a Confocal Raman Microscope Alpa-Witek operating at a wavelength of 514 nm. Each sample was flattened on a glass slide and focused under a 20x microscope lens. Spectra were collected from five distinct spots for each sample. Ten scans were performed for each spot. Peak fitting was performed using GRAMS/AI spectroscopy software from Thermo Scientific. Thermogravimetric analyses of all samples were carried out on a NETZSCH STA 449 F1 Jupiter instrument. Approximately 10 mg of sample were heated from 25-1500 ^{o}C at a ramp rate of 5 ^{o}C min^{-1} and a flow rate of 20 ml min^{-1} of air (Airgas 99.999%). Residual metal % was calculated by assuming total combustion of carbon, and conversion of Fe to Fe_2O_3.

Scanning electron microscopy (SEM) images were obtained using a LEO 1530 Thermally-Assisted Field Emission (TFE) Scanning Electron Microscope (SEM). All samples were deposited onto carbon tape and not sputter coated prior to scanning. Images were scanned at an accelerating voltage of 10 kV. Quantitative chemical analysis of select samples was conducted utilizing an Oxford-7426 EDS detector attached to the LEO 1530 TFE SEM. At least three separate spots were surveyed for each sample. TEM images were obtained using a Hitachi HT7700 TEM at an operating voltage of 120kV.

High resolution (HRTEM) images and diffraction patterns were obtained using a FEI Tecnai F30 at an operating voltage of 300 kV. Samples were suspended in a solution of methanol and deposited on a holey carbon grid with an ultrafine carbon film.

The schematic of our experimental setup can be seen in **Chapter 2,** under **Figure 2.2** and **Figure 2.3**. Fe_3C-CDC powder was packed within a quartz bed against a fine quartz frit of ID 4 mm to a standardized bed volume of $55mm^3$. Samples were activated under 50 ml min^{-1} N_2 flow at 150 ^oC for 2 hours and then allowed to cool back down to room temperature for 30-45 minutes. After cooling, the dry or wet breakthrough run was started. The dry run was initiated by switching the N_2 to a stream of 1500 ppm NH_3 in air at a rate of 20 ml min^{-1} (Airgas). For humid breakthrough experiments, the humid stream was created by flowing air at 16 ml min^{-1} through a H_2O bubbler, and then combining it with a NH_3 stream of 7155 ppm and a flow rate of 4 ml min^{-1}. The total mixed stream flowed through the packed bed at a rate of 20 ml min^{-1} with a measured relative humidity of 75% and a calculated NH_3 concentration of 1431 ppm. The effluent stream was analyzed using an Analytical Technology H10-15 ammonia electrochemical sensor. Once the dilute NH_3 stream was switched on, data points were taken at 30 second intervals until the sensor reached 500 ppm NH_3, at which point the NH_3 was switched off to preserve the life of the sensor. N_2 flow was maintained at 50 ml min^{-1} to capture the desorption behavior of the bed, and the sensor reading was recorded until the NH_3 concentration returned to ~100 ppm. A blank bed of sand was used to calculate the dead time within the system, and was subtracted from the breakthrough time of evaluated samples. No significant pressure drop was noted for these conditions. The experimental procedure for wet and dry conditions was identical. Exhausted unannealed samples were

labeled Fe_3C-CDC-CT-T-DE or Fe_3C-CDC-CT-T-WE to signify exposure to ammonia under both dry (DE) and wet (WE) conditions.

NH_3-TPD experiments were carried out using a Micromeritics© AutoChem II 2920 apparatus to probe the strength of acidic sites on Fe_3C-CDCs evaluated for ammonia adsorption. Approximately 40 mg of Fe_3C-CDC was loaded into a quartz U-tube, and each sample was pretreated in flowing He at 150 ^oC to remove adsorbed H_2O. After cooling, the sample was exposed to 20 ml min^{-1} of 2000 ppm NH_3 in a He carrier gas for 2 hours at 25 ^oC. To obtain the NH_3-TPD profile, the flow was then switched to He and the temperature was ramped to 500 ^oC at a rate of 5 ^oC min^{-1}. The effluent stream was analyzed by a thermal conductivity detector (TCD).

A Magna 560 FTIR (Nicolet Instruments) was used to collect FTIR spectra on samples before and after ammonia exposure. FTIR samples were prepared by diluting CDC powder with KBr in a 1:200 ratio and then pressed into a 13 mm disk. Absorbance data was averaged over 128 scans at a resolution of 2 cm^{-1}. A fresh background scan was taken and subtracted before each sample.

4.4 Results and Discussion

4.4.1 Dependence of Fe_3C-CDC Porosity on Reaction Temperature

Iron carbide was reacted with chlorine gas to selectively extract iron through the following reaction schemes:

$$Fe_3C + \frac{9}{2}Cl_2 \rightarrow 3FeCl_3 + C \quad (1)$$

$$Fe_3C + 3Cl_2 \rightarrow 3FeCl_2 + C \quad (2)$$

Fe_3C-CDCs were synthesized at different chlorination temperatures and evaluated by nitrogen physisorption, QSDFT, and PXRD to understand the effect of chlorination temperature on their physical properties. Nitrogen isotherms at 77 K are shown in **Figure 4.1**. There was an evident contrast between samples chlorinated below and above 500 ^{o}C. These results are shown in **Figure 4.1(a)** and **Figure 4.1(b)**. The isotherms in **Figure 4.1(a)** for Fe_3C-CDCs samples synthesized at temperatures $\leq$ 500 ^{o}C, exhibit characteristic type I isotherms by Brunauer classification.[25-27] There is a slight hysteresis and more gradual slope observed in the isotherms of 400C-2h-H_2 and 500C-2h-H_2, as the isotherm shape gradually shifts to a type IV isotherm seen for 600C-2h-H_2 in **Figure 4.1(b)**. As the chlorination temperature increases, the hysteresis beginning around the relative pressure P/P_0 = 0.42 widens. The gradual slope of the adsorption branch and the sharp decline in the desorption branch around this relative pressure resembles a H2 type hysteresis and heavily suggests the presence of cavitation effects.[28-30] There is also higher uptake close to the saturation pressure for 700C-2h-H_2 and 800C-2h-H_2, indicating a significant evolution of macroporosity at higher chlorination temperatures. Before QSDFT analysis, it was initially concluded that samples chlorinated at $\leq$ 500 ^{o}C were mainly microporous, while samples chlorinated at > 500 ^{o}C exhibited a much larger degree of meso and macroporosity.

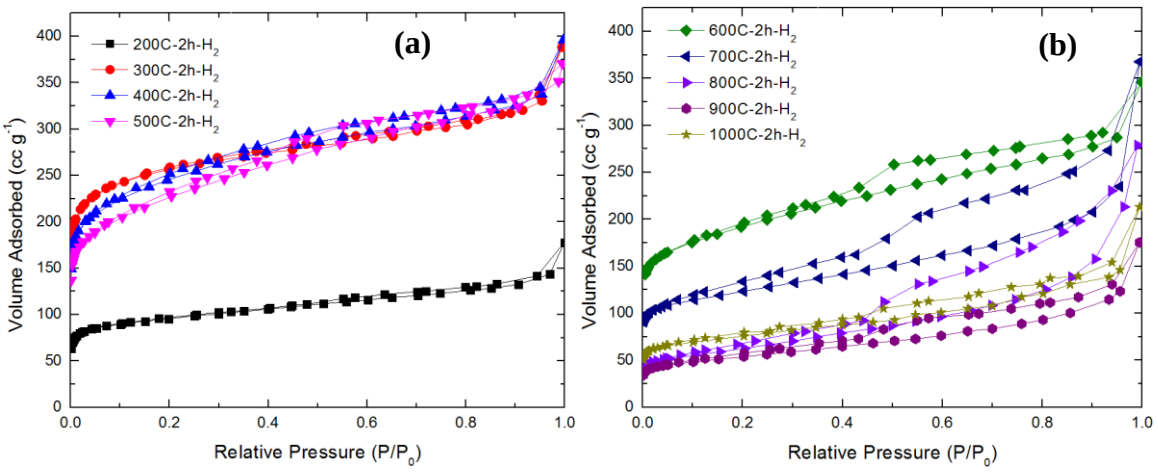

Figure 4.1. N_2 adsorption isotherms for (a) Low and (b) High Temperature Annealed Fe_3C-CDCs

The change in porosity versus chlorination temperature can be seen in **Figure 4.2**. A maximum specific surface area of 875 m^2 g^{-1} was achieved for the 300C-2h-H_2 sample. It is possible that this surface area could further increase at chlorination temperatures $\leq$ 300 ^oC, since at these temperatures it was difficult to achieve complete extraction of iron within 2 hours. The pore volume was relatively consistent for samples chlorinated between 300 ^oC and 700 ^oC, with a maximum pore volume of 0.66 cc g^{-1} for 400C-2h-H_2. As the chlorination temperature increases over this range, there is a decrease in surface area and increase in mesoporosity. Both decreasing surface area and increasing mesoporosity at higher chlorination temperatures have been observed for the chlorination of many other carbides.[14-16, 31] These trends are correlated with an increase in graphitization and ordering of the carbide-derived carbon at higher chlorination temperatures.

Table 4.1. Synthesis Conditions and Porosity for Annealed Fe_3C-CDCs

Sample Name	Chlorination Time (h)	Annealing Time (h)	Specific Surface Area ($m^2\ g^{-1}$)[a]	Pore Volume (cc g^{-1})[b]
Fe_3C	0	0	20	0.02
Fe_3C-CDC-200C-2h-H_2	2	3	330	0.28
Fe_3C-CDC-300C-2h-H_2	2	3	875	0.60
Fe_3C-CDC-400C-2h-H_2	2	3	860	0.66
Fe_3C-CDC-500C-2h-H_2	2	3	748	0.60
Fe_3C-CDC-600C-2h-H_2	2	3	652	0.48
Fe_3C-CDC-700C-2h-H_2	2	3	432	0.57
Fe_3C-CDC-800C-2h-H_2	2	3	197	0.43
Fe_3C-CDC-900C-2h-H_2	2	3	173	0.27
Fe_3C-CDC-1000C-2h-H_2	2	3	261	0.34

a)Obtained by BET Analysis at a Relative Pressure (P/P_0) Range of 0.01-0.05 b) Obtained at $P/P_0 = 0.99$

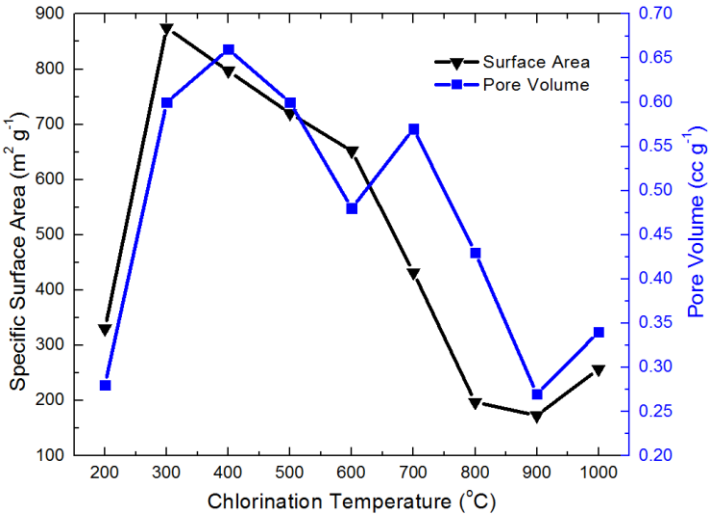

Figure 4.2. Annealed Fe_3C-CDC porosity versus chlorination temperature

Quenched Solid Density Functional Theory (QSDFT) was used to further investigate the effect of chlorination temperature on pore size, and the results are summarized in **Figure 4.3**.[32] Two different QSDFT methods were used to account for the distinct shift in pore architecture evident by the isotherm shapes in **Figure 4.1(a)** and **Figure 4.1(b)**. A slit-pore model was assumed for samples $\leq$ 500 ^{o}C with type I isotherms, and an adsorption branch slit-pore and cylindrical pore model was assumed for

samples > 500 ^{o}C exhibiting type IV isotherms and characteristic cavitation effects. Only the adsorption branch of the isotherm was applied for samples > 500 ^{o}C, as the sudden pore emptying in the desorption branch around P/P_0 = 0.42 is caused by the thermo-physical properties of nitrogen at 77 K and is not indicative of the pore size.[30] In **Figure 4.3(a)**, samples chlorinated at ≤ 500 ^{o}C show the majority of pores are < 2 nm in diameter with an initial peak maximum at 7 Å, with further microporosity likely present at pore sizes too small to be accurately infiltrated by the nitrogen probe molecule. A significant amount of small mesopores (< 4 nm in diameter) begin to develop at 400 ^{o}C as higher temperature Fe_3C-CDCs exhibit a micro and mesoporous structure due to increased structural ordering. In **Figure 4.3(b)**, there is a severe decrease in microporosity after 600 ^{o}C and a broad range of mesoporosity between 2 – 8 nm pore diameter. Further increases occur for meso and macropores with diameters > 100 nm for ≥ 700 ^{o}C samples, consistent with the sharp increase at high relative pressures for these samples. Full scale pore size distributions can be seen in **Appendix B**.

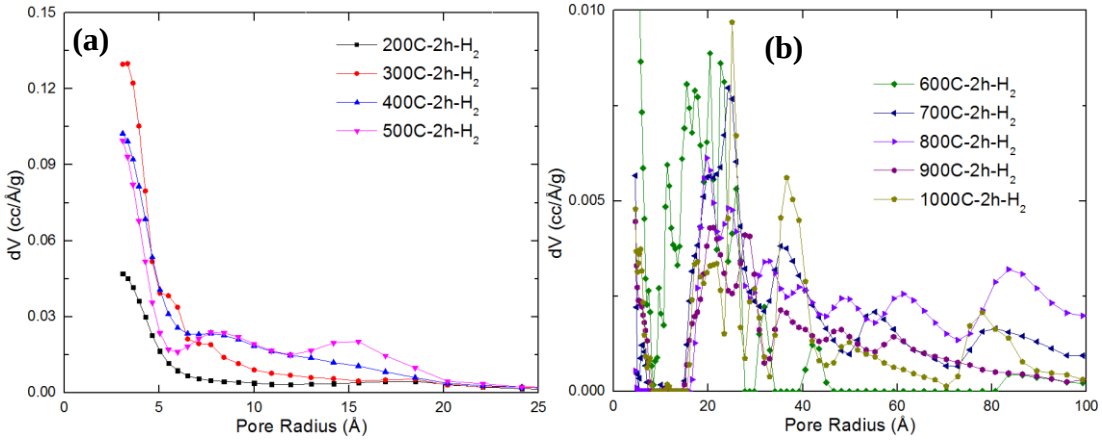

Figure 4.3. Pore size distributions for (a) Low Temperature and (b) High Temperature Annealed Fe_3C-CDCs

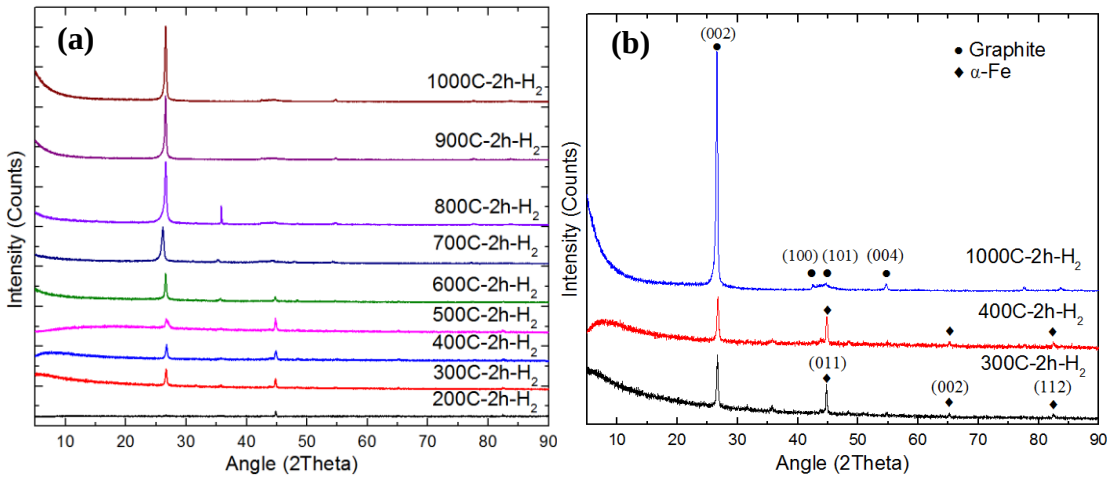

Figure 4.4. PXRD Patterns of Annealed Fe_3C-CDCs

Powder X-ray Diffraction (PXRD) patterns were collected for all samples and can be seen in **Figure 4.4**. The increase in mesoporosity at higher chlorination temperatures correlates well with the appearance and increase in intensity of several peaks corresponding to graphite. Peaks at 2θ = ~26° and 2θ = ~55° are identified as the (002) and (004) graphite reflection, which correspond to the parallel stacking of graphite layers. At higher chlorination temperatures, the (100) and (101) planes that represent the in-plane symmetry along graphene layers are present as a broad peak at 2θ = ~43°. These can be seen more clearly for 1000C-2h-H_2 in **Figure 4.4(b)**. The larger width of this peak at 2θ = ~43° is due to the presence of stacking faults for the in-plane direction. Scanning electron microscopy (SEM) images of these samples also support a much higher degree of graphitic ordering and will be discussed in later sections. Samples with incomplete conversion, also exhibited peaks at 2θ = ~45°, ~65°, and ~82° corresponding to the (011), the (002), and the (112) reflection of α-Fe. The presence of these peaks signify there is residual Fe present in the metallic form and not as unreacted carbide. Gravimetric calculations were performed for these samples according to **Equation B.1**. It can be seen in **Table B.1** that there is a significant portion of iron that has not been extracted from the

resulting CDC. As shown previously at 600 ^{o}C, a large percentage of iron chloride products can be retained in Fe_3C-CDCs due to graphitic carbon nanostructures that prevent or slow their removal.[24] After annealing treatment, they can be further reduced and present in the metallic form. From the α-Fe peaks present in **Figure 4.4**, this phenonemon appears extendable to other temperature regimes.

The (002) reflection of graphite at $2\theta = \sim 26^{o}$ is present for all samples, even for 200C-2h-H_2. A previous study by Gogotsi et al. showed unannealed Fe_3C-derived carbons chlorinated at or below 500 ^{o}C to be amorphous and found no evidence of ordered parallel graphitic layers via the (002) or (004) reflection in the PXRD pattern.[13] The addition of an annealing treatment and temperature ramp from chlorination temperature to the annealing temperature of 600 ^{o}C in this study likely facilitates this graphitization. In our previous study,[24] it was seen that a significant percentage of iron chloride products were retained as nanoparticles within the resulting CDC framework. It was hypothesized that $FeCl_3$ is retained at chlorination temperatures exceeding its decomposition temperature by catalyzing the growth of surrounding graphitic carbon nanostructures that prevent its removal to the bulk gas phase.[24] The addition of iron chloride to many carbides has also been shown to catalyze graphitization during the chlorination process, particularly at higher temperatures.[33-35] Gravimetric calculations in **Table B.1,** as well as the α-Fe present in the PXRD patterns in **Figure 4.4**, signify the presence of the iron chlorides before annealing treatment, and these retained iron chlorides likely catalyze the growth of graphitic domains during the temperature ramp. These graphitic domains are further investigated using Raman spectroscopy and their morphology is examined through Scanning Electron Microscopy.

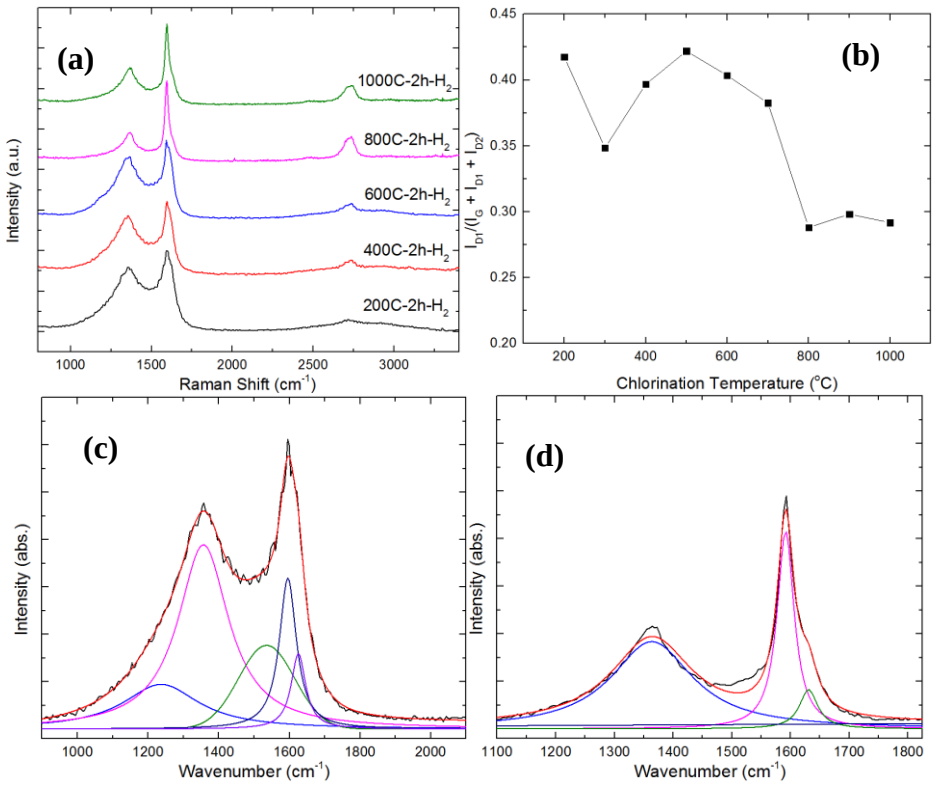

Figure 4.5. (a) Raman Spectra of Annealed Fe_3C-CDCs, (b) Degree of graphitization of Annealed Fe_3C-CDCs (c) Deconvolution of 200C-2h-H_2 (d) Deconvolution of 800C-2h-H_2

Raman spectra for annealed Fe_3C-CDCs are presented in **Figure 4.5(a)**. For all samples, two large first-order peaks were observed at ~1350 cm^{-1} and ~1590 cm^{-1}. These peaks were assigned to the D band and graphitic G band, respectively. The D band corresponds to defects and disorder within graphitic sheets and the G band corresponds to the vibrational mode of an ideal graphitic lattice with E_{2g} symmetry.[36] The D band can be further deconvoluted, depending on the type of carbonaceous material. Disordered graphite is usually fit with three peaks: the G band, the D1 band at ~1350 cm^{-1} assigned to the graphitic lattice breathing mode with A_{1g} symmetry, and the D2 band at ~1610 cm^{-1} corresponding to a graphitic lattice vibration mode with E_{2g} symmetry, but at the surface of a graphite crystal.[36-39] These three peaks fit well for Fe_3C-CDCs chlorinated at temperatures > 800 ^oC, as the D1 band can clearly be seen as a right shoulder to the

main G band peak. For samples chlorinated at a lower temperature, the D band was further deconvoluted into an additional D3 peak present at 1510 cm^{-1}, and a broad D4 peak present at 1150 cm^{-1}. The D4 peak has been tentatively ascribed to polyene structures and ionic impurities within graphitic lattices, and the D3 peak is assigned to amorphous carbon.[40-42] All peaks were fit with Lorentzian peak shapes, except D3, where a Gaussian peak was assumed.[38, 42] The degree of graphitization was used to determine the relative degree of ordering with a carbonaceous material, and these results are plotted versus chlorination temperature in **Figure 4.5(b)**. The degree of graphitization was calculated by averaging the $I_{D1}\backslash(I_G + I_{D1} + I_{D2})$ ratio taken from several spots within the CDC. The degree of graphitization is seen to remain relatively constant until a sharp decrease at chlorination temperatures $\geq$ 800 ^oC. These observations are consistent with the appearance of the (004) and (101) peaks in the diffraction patterns, indicating a direct relationship between graphitic ordering and chlorination temperature for annealed Fe_3C-CDCs.

A second-order peak was also observed at ~2720 cm^{-1}, becoming gradually sharper at higher chlorination temperatures. This broad peak, was assigned to the first overtone of the D1 band, (2 * D1), and is also referred to as the S1 band.[37, 40] In the case of well-ordered graphite, this band splits into two distinct peaks – a main peak at ~2720 cm^{-1} for the $(2* D1)_1$ band, with a pronounced shoulder at ~2680 cm^{-1} labeled as the $(2* D1)_2$ band.[43] The increased intensity of the S1 band at higher chlorination temperatures correlates well with the appearance of (004), (100), and (101) reflections of graphite in the PXRD patterns. These samples are still disordered graphitic structures even when

chlorinated at 1000 ^{o}C, as the S1 band can still be seen as one broad peak, indicating a lack of highly ordered graphite over significant 3-D domains.

4.4.2 Dependence of Fe_3C-CDC Topology on Chlorination Temperature

SEM images were taken across the full range of chlorination temperature, and can be seen in **Figure 4.6**, **Figure 4.7**, and **Figures B.3-B.7 in the Appendix B**. There are noted differences in the SEM images for Fe_3C-CDCs chlorinated at low and high temperatures, summarized in **Figure 4.6**. At 300 ^{o}C and 500 ^{o}C, in **Figure 4.6(a-b)** there are highly ordered tubular structures with sharp edges. These structures were investigated further using TEM. These domains are not present at higher temperatures, where the carbon is seen to be largely comprised of planar graphitic sheets. This is consistent with the high amount of 3-D ordering previously seen in the PXRD patterns. Similar tubular structures are confirmed to be carbon nanotubes under TEM, seen in **Figure 4.8(a-b).**

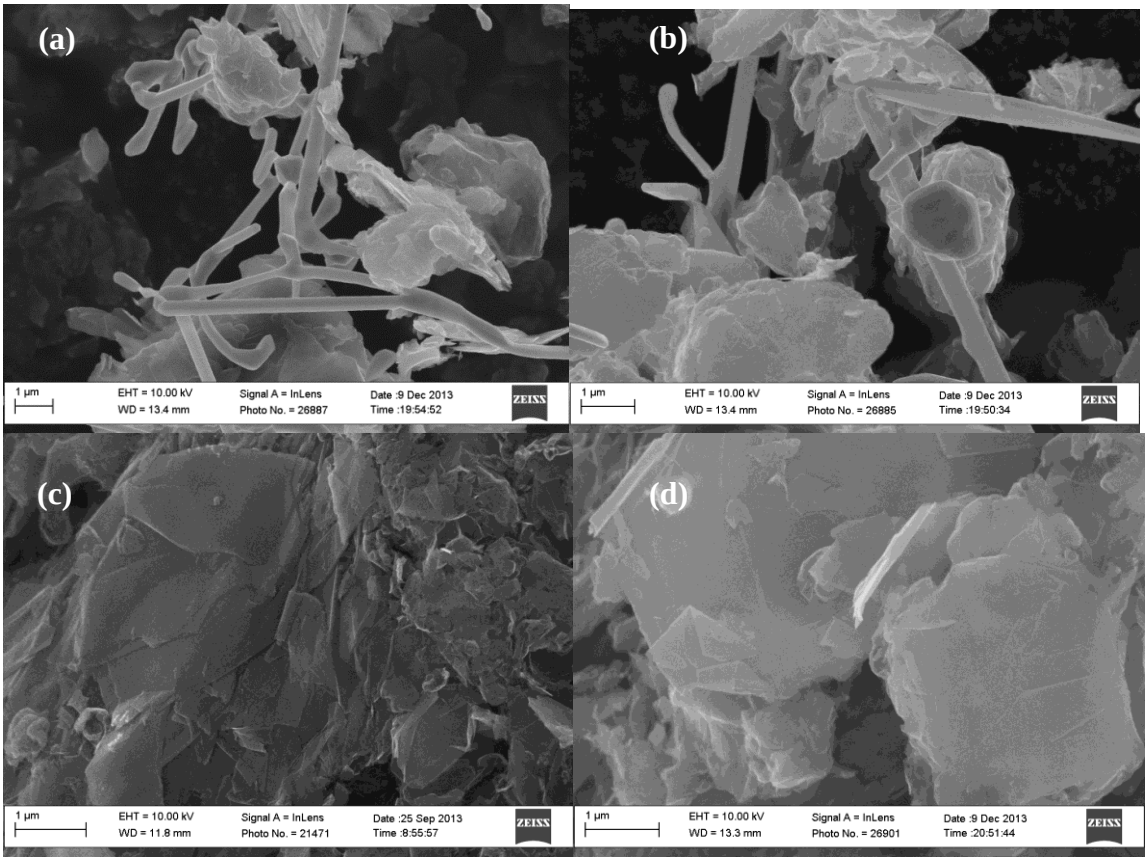

Figure 4.6. SEM Images of (a) 300C-2h-H_2 (b) 500C-2h-H_2 (c) 800C-2h-H_2 (d) 1000C-2h-H_2

The 200C-2h-H_2 sample exhibits the most interesting structures, seen in **Figure 4.7**. Well-ordered rectangular prisms can be seen in **Figure 4.7(a)**, ordered cylinders are present in **Figure 4.7(b)**, as well as pillared, complex 3-D prisms and cubes present in **Figures 4.7(c)** and **(d)**. At 200 ^{o}C, one of the main chlorination products, $FeCl_3$, is present below its boiling point (316 ^{o}C) for this sample. Most of the reaction product is still able to vaporize to the bulk gas phase, as evident from its high conversion in **Table B.1**, and EELS spectra on cubic shaped particles in **Figure 4.8(c)** and **Figure B.8** show no Fe present in these cubic domains. Both carbon and chlorine are present in the EELS Spectra in **Figure B.9**, and as evident from the diffraction patterns in **Figure 4.8(d)** and **Figure B.8**, these domains exhibit crystallinity. It is hypothesized that the slow

vaporization of $FeCl_3$ at this temperature allows ample time for the catalyzed formation of these intricate structures. At modest temperatures < 600 ^oC, iron chlorides are postulated to catalyze carbon nanostructures above its boiling point, as these nanostructures are hypothesized to impede the sublimation of $FeCl_3$ decomposition products, $FeCl_3$ and Fe_2Cl_6. Indeed, in our earlier investigation,[24] the presence of iron chloride in the tips of carbon nanotubes and Fe particles surrounded by graphitic carbon nanostructures were observed by TEM for samples synthesized at 600 ^oC. Similar, curved graphitic carbon nanotubes can be seen both in the SEM images in **Figure 4.6(a-b)** and in TEM in **Figure 4.8(a-b)** at chlorination temperatures of 300 ^oC and 500 ^oC.

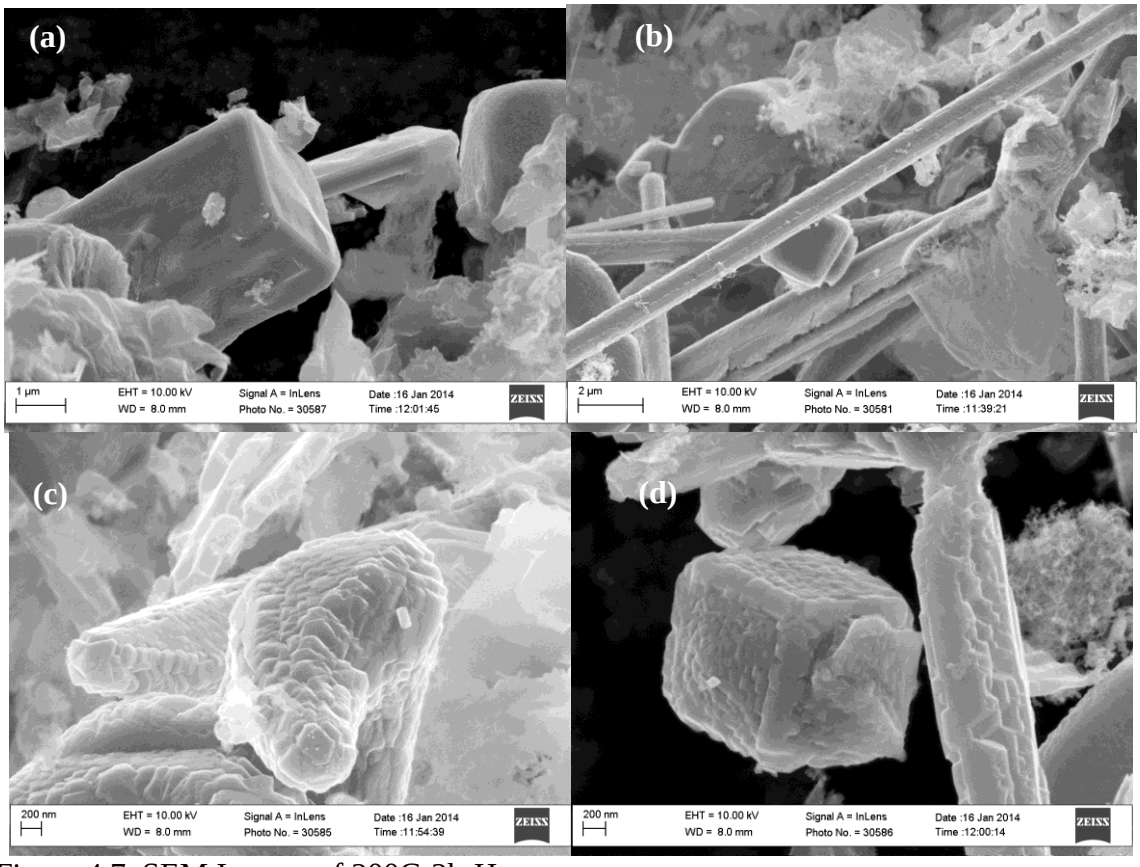

Figure 4.7. SEM Images of 200C-2h-H_2

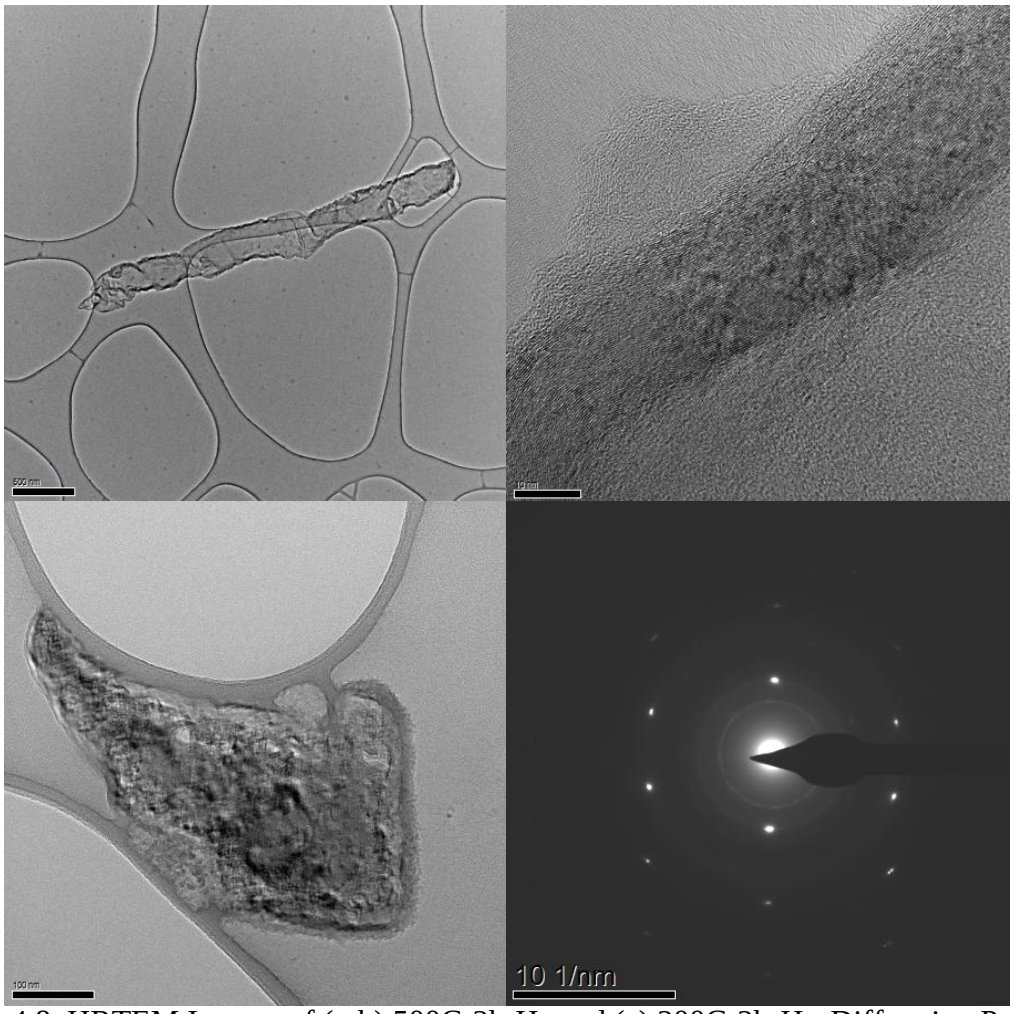

Figure 4.8. HRTEM Images of (a-b) 500C-2h-H_2 and (c) 200C-2h-H_2, Diffraction Pattern of (d) 200C-2h-H_2

4.4.3 Ammonia Breakthrough Experiments for Unannealed Fe_3C-CDCs

Ammonia breakthrough curves are shown in **Figure 4.9** for dry and humid conditions at 25 °C. For these experiments, a series of unannealed Fe_3C-CDCs were evaluated. These unannealed Fe_3C-CDCs were chlorinated at 600 ^oC for various chlorination times to include residual $FeCl_3$ nanoparticles.[24] Unlike the samples chlorinated at different temperatures, as seen in **Table 4.1,** these samples were not annealed to prevent the reduction of $FeCl_3$ to metallic Fe. It was hypothesized that NH_3 would form strong chemisorption interactions with $FeCl_3$ via the formation of metal

ammine chlorides.[7, 44] To evaluate the effect of $FeCl_3$ nanoparticles, Fe_3C was also chlorinated at 5 hours to prepare a metal free sample for use as a standard. Trapped Cl_2 is also present in unannealed CDCs, and prepared unannealed Fe_3C-CDCs were probed by EDS and FTIR to understand the role of residual chlorine on dynamic adsorptive performance.[45] The breakthrough time for these dynamic experiments was normalized on a per gram basis and the dynamic capacities, $W_{E,}$ were calculated by Equation (4):

$$W_E = \frac{\dot{n}_{NH_3} t_b}{m_{bed}} \quad (4)$$

A molar flow rate of $NH_{3,}$ $\dot{n}_{NH3}$, was adsorbed by the bed until breakthrough at time, t_b. This breakthrough time, t_b, is the time from when the NH_3 stream was first switched on, until initial breakthrough when the electrochemical sensor first registered $[NH_3] > 0$ ppm on the effluent stream. It is important to note that these dynamic capacities were taken at this initial breakthrough condition, as dynamic capacities calculated in other studies can also contain the integral of the breakthrough curve until saturation, which includes additional dynamic capacity retained by the sample after initial breakthrough but before complete saturation. The molar adsorbed amount of NH_3 was normalized by a known mass of the adsorbent, m_{bed}, to provide the normalized dynamic loading for each sample seen in **Table 4.2**. Repeatability of t_b on this breakthrough system was +/- 10%.

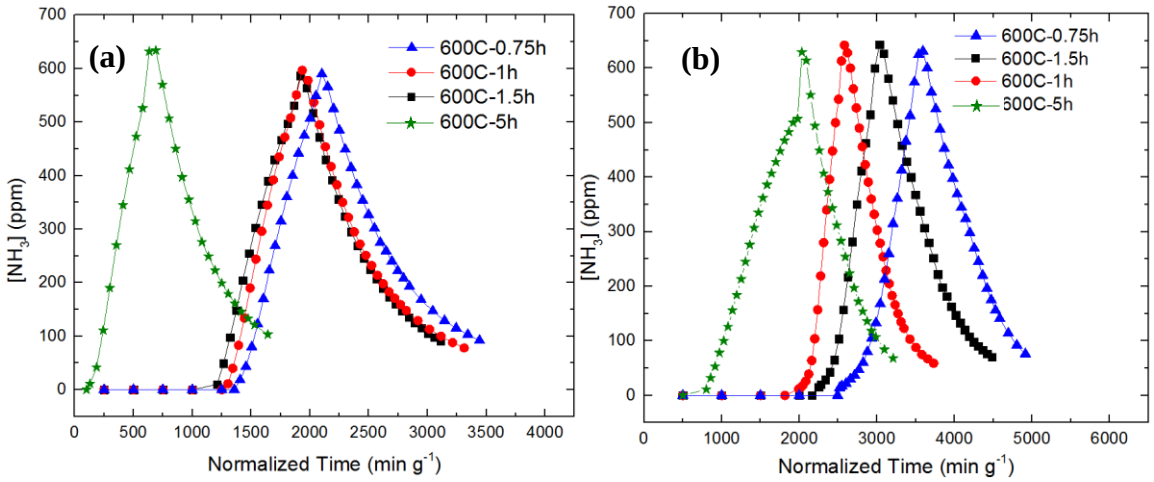

Figure 4.9. Breakthrough and desorption curves for unannealed Fe_3C-CDCs under dry (a) and humid (b) conditions

The bulk porosity and pore size distributions for unannealed Fe_3C-CDCs can be seen as in **Table 4.2** and **Figure B.2** in the **Appendix B**. Surface area, pore volume, and pore size are consistent between samples. Unannealed CDCs have lower surface area than the annealed CDCs seen in **Table 4.1** due to the presence of trapped chlorine that are normally removed by H_2 treatment.[45] In our previous study, it was shown that the presence of moderate amounts of $FeCl_3$ nanoparticles does not greatly affect porosity.[24] No significant improvement in surface area was seen after chlorinating past 45 min at 600^{o}C to fully remove residual Fe species. The metal free standard, 600C-5h, has slightly lower surface area and lower volume of micropores, which is likely caused by some structural degradation or increased pore filling from trapped chlorine species due to long exposure of chlorine gas at high temperature. Residual chlorine concentrations obtained through EDS show a decrease in chlorine concentration with increasing treatment time, as more $FeCl_3$ nanoparticles are slowly removed from the CDC matrix. The metal free standard had no measureable Fe present over numerous spots within the sample, but did include a significant amount of trapped chlorine species.

4.4.4 Role of Chlorine and $FeCl_3$ Nanoparticles for Ammonia Adsorption

Under dry conditions in **Figure 4.10(a)**, all samples had very similar breakthrough times around 1300 min g^{-1}, corresponding to dry capacities between 1.62-1.88 mmol g^{-1}. Under wet conditions in **Figure 4.10(b)**, the 600C-0.75h sample with 8.4% residual Fe has the highest wet capacity, at 3.44 mmol g^{-1}, while 600C-1h and 600C-1.5h exhibit lower wet capacities of 2.45 and 2.91 mmol g^{-1}. The metal-free standard, 600C-5h, had almost instantaneous breakthrough under dry conditions, and drastically lower humid dynamic capacity. This standard had similar physical properties and chlorine content to samples containing $FeCl_3$ nanoparticles, and heavily suggests residual metal plays a strong role in dynamic NH_3 adsorption.

Table 4.2. Dry and Humid NH_3 Dynamic Adsorption Capacities

Sample Name	Specific Surface Area (m_2 g^{-1})	Pore Volume (cc g^{-1})	Amount Fe (wt %)[a]	Amount Cl (wt %)[b]	Dry NH_3 Dynamic Capacity (mmol g^{-1})[c]	Humid NH_3 Dynamic Capacity (mmol g^{-1})[c]
Fe_3C-CDC-600C-0.75h[d]	339	0.34	8.4	15.0	1.88	3.44
Fe_3C-CDC-600C-1h[d]	374	0.40	4.0	13.4	1.75	2.45
Fe_3C-CDC-600C-1.5h[d]	353	0.38	2.4	10.8	1.62	2.91
Fe_3C-CDC-600C-5h	257	0.36	0.0[b]	5.7	0.17	1.07

a) Calculated from TGA b) Determined from EDS c) Calculated by initial breakthrough time d)Synthesized in a previous study[24]

To further elucidate the interactions between NH_3 and $FeCl_3$ nanoparticles embedded in unannealed Fe_3C-CDCs, NH_3-TPD experiments were carried out and ammonia desorption profiles can be seen in **Figure 4.10**. Two main peaks were observed – centered at ~70 ^oC and 220 ^oC, respectively. The integral of the 220 ^oC peak increases with residual Fe content, and was not observed for the metal free 600C-5h sample. This peak was assigned to chemisorption interactions resulting from the formation of iron ammine chlorides, and is not present for the 600C-5h as a result of complete $FeCl_3$

removal. One likely complex is $Fe[(NH_3)_6]Cl_3$, which has been observed to form spontaneously from $FeCl_3$ and NH_3 at room temperature.[46] Desorption occurring at ~70 ^oC is suggested to be weak physisorption interactions occurring between the pore wall and NH_3, in addition to interactions residual trapped chlorine present from the chlorination synthesis.

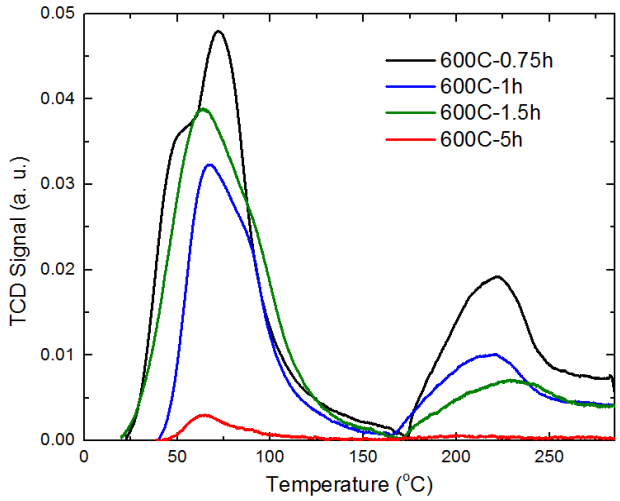

Figure 4.10. NH_3-TPD Profile for unannealed Fe_3C-CDCs

FTIR spectra were collected for fresh and exhausted samples, and can be seen in **Figure 4.11**. 600C-1h-DE and 600C-1h-WE, after exposure to ammonia during dry breakthrough (DE) and wet breakthrough conditions (WE), show a strong peak at 1400 cm^{-1}. This peak corresponds to the NH_4^+ deformation and matches well with the FTIR spectra of NH_4Cl, further indicating the formation of an ammine complex with the iron salt.[47] All fresh and exhausted samples also exhibit a strong peak at ~ 1375 cm^{-1}. This peak was assigned to C-H bending in plane, separate from the NH_4^+ peak at 1400 cm^{-1}. The ammonium peak is absent from the metal-free 600C-5h spectrum under dry conditions, and only present under humid conditions. As this peak is present for 600C-5h-WE, the retention of NH_4^+ under humid conditions is not solely due to complexation with $FeCl_3$. It is well-known that chlorine gas reacts with water to form HOCl and HCl.

Trapped chlorine gas is also likely to form ammonium chloride through the following reaction scheme:

$$Cl_2 + H_2O \rightarrow HOCl + HCl \quad (3)$$

$$NH_3 + HCl \rightarrow NH_4Cl \quad (4)$$

The ability of trapped chlorine gas to convert to HCl and react to form an ammonium salt explains the modest capacity of 600C-5h under humid breakthrough conditions. It has been seen in the literature that the dissolution of ammonia in co-adsorbed water could also facilitate acid-base interactions between NH_3 and acidic functional groups on the surface of carbon adsorbents.[48] However, there are relatively little oxygen containing functional groups seen in the FTIR spectra of unannealed Fe_3C-CDCs and low oxygen content seen in EDS experiments, making it likely that ammonium is predominately formed through interactions with chlorine in 600C-5h, as opposed to acidic functional groups.

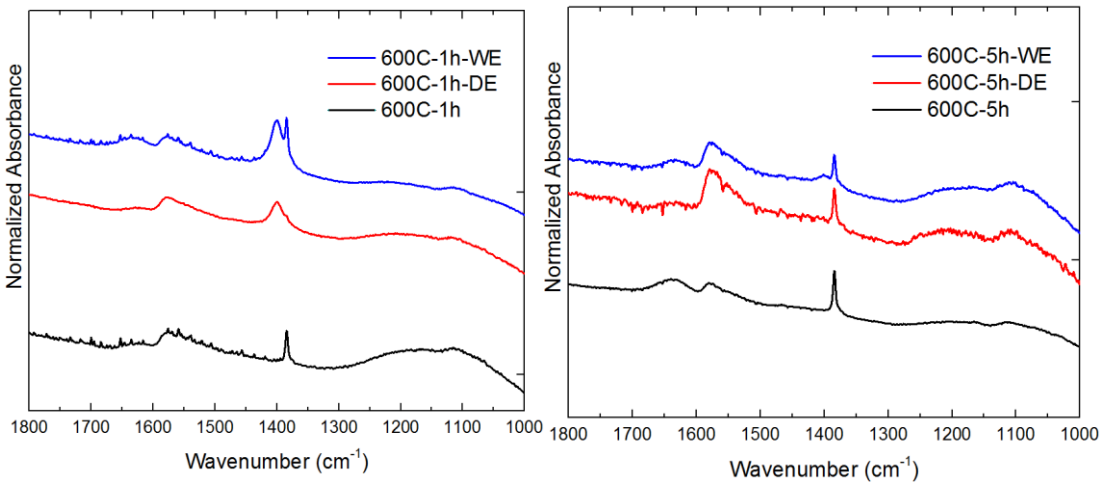

Figure 4.11. FTIR Spectra of fresh and exhausted unannealed Fe_3C-CDCs

4.5 Conclusions

Fe was selectively extracted from Fe_3C via chlorination and the effect of chlorination temperature on the physical properties of annealed Fe_3C-CDCs was

examined. Highly microporous Fe_3C-CDCs can be synthesized at low chlorination temperatures, with a maximum surface area (875 m^2 g^{-1}) obtained at 400 ^oC. It is possible that even higher surface areas and pore volumes can be obtained by chlorinating till complete extraction at extremely low temperatures (200 ^oC). The pore size of annealed Fe_3C-CDCs is highly versatile, and can be tuned by raising the chlorination temperature to allow increasing amounts of mesoporosity and macroporosity when desired. At low temperatures, the extraction of Fe is seen to catalyze the formation of very well ordered tubular and planar carbon structures. Over the entire temperature range, a high degree of graphitization was observed within both the PXRD patterns and Raman spectra.

In addition, at certain temperatures it was previously found that Fe_3C-CDCs synthesized at 600°C could retain iron chloride nanoparticles dispersed with their nanoporous framework. These samples were evaluated for NH_3 breakthrough experiments and exhibited high dynamic loadings under both dry and wet conditions. The sample with the highest amount of residual metal, 600C-0.75h, had the best performance with dynamic capacities of 1.88 mmol g^{-1} and 3.44 mmol g^{-1} under dry and wet conditions, respectively. When compared to a metal free Fe_3C-CDC control, Fe_3C-CDC-0.75h performed 1100% and 320% better under dry and wet conditions, respectively. NH_3-TPD and FTIR experiments show that this superior performance is a direct result of chemisorption interactions between NH_3 and $FeCl_3$ particles within the microporous framework. This is a particularly important conclusion, as these nanoparticles are hypothesized to be retained during synthesis due surrounding graphitic nanostructures, which hinder their diffusion into the bulk gas phase. In this work, these nanoparticles are still shown to be active in the adsorption of ammonia from air, indicating that they remain

accessible and are able to interact with small gases. In addition, trapped chlorine gas present from the CDC synthesis is shown to play a beneficial role for NH_3 adsorption in humid environments.

4.6 References

[1] Shenderova OA, Zhirnov VV, Brenner DW. Carbon Nanostructures. Critical Reviews in Solid State and Materials Sciences. 2002;27(3-4):227-356.

[2] Davis ME. Ordered porous materials for emerging applications. Nature. 2002;417(6891):813-21.

[3] Roney N, Llados F, Little S, Knaebel D. Toxicological Profile for Ammonia. In: Services USDoHaH, ed. 2004.

[4] Long JW, Laskoski M, Peterson GW, Keller TM, Pettigrew KA, Schindler BJ. Metal-catalyzed graphitic nanostructures as sorbents for vapor-phase ammonia. Journal of Materials Chemistry. 2011;21(10):3477-84.

[5] Corre Y, Seredych M, Bandosz TJ. Analysis of the chemical and physical factors affecting reactive adsorption of ammonia on graphene/nanoporous carbon composites. Carbon. 2013;55:176-84.

[6] Petit C, Bandosz TJ. Removal of ammonia from air on molybdenum and tungsten oxide modified activated carbons. Environmental Science & Technology. 2008;42(8):3033-9.

[7] Petit C, Karwacki C, Peterson G, Bandosz TJ. Interactions of ammonia with the surface of microporous carbon impregnated with transition metal chlorides. Journal of Physical Chemistry C. 2007;111(34):12705-14.

[8] Seredych M, Bandosz TJ. Removal of ammonia by graphite oxide via its intercalation and reactive adsorption. Carbon. 2007;45(10):2130-2.

[9] Seredych M, Tamashausky AV, Bandosz TJ. Graphite Oxides Obtained from Porous Graphite: The Role of Surface Chemistry and Texture in Ammonia Retention at Ambient Conditions. Advanced Functional Materials. 2010;20(10):1670-9.

[10] Seredych M, Rossin JA, Bandosz TJ. Changes in graphite oxide texture and chemistry upon oxidation and reduction and their effect on adsorption of ammonia. Carbon. 2011;49(13):4392-402.

[11] Presser V, Heon M, Gogotsi Y. Carbide-Derived Carbons - From Porous Networks to Nanotubes and Graphene. Advanced Functional Materials. 2011;21(5):810-33.

[12] Gogotsi Y, Nikitin A, Ye H, Zhou W, Fischer JE, Yi B, et al. Nanoporous carbide-derived carbon with tunable pore size. Nat Mater. 2003;2(9):591-4.

[13] Dimovski S, Nikitin A, Ye H, Gogotsi Y. Synthesis of graphite by chlorination of iron carbide at moderate temperatures. Journal of Materials Chemistry. 2004;14(2):238-43.

[14] Dash RK, Yushin G, Gogotsi Y. Synthesis, structure and porosity analysis of microporous and mesoporous carbon derived from zirconium carbide. Microporous and Mesoporous Materials. 2005;86(1-3):50-7.

[15] Dash R, Chmiola J, Yushin G, Gogotsi Y, Laudisio G, Singer J, et al. Titanium carbide derived nanoporous carbon for energy-related applications. Carbon. 2006;44(12):2489-97.

[16] Tallo I, Thomberg T, Kontturi K, Jänes A, Lust E. Nanostructured carbide-derived carbon synthesized by chlorination of tungsten carbide. Carbon. 2011;49(13):4427-33.

[17] Presser V, McDonough J, Yeon S-H, Gogotsi Y. Effect of pore size on carbon dioxide sorption by carbide derived carbon. Energy & Environmental Science. 2011;4(8):3059.

[18] Kim HS, Singer JP, Gogotsi Y, Fischer JE. Molybdenum carbide-derived carbon for hydrogen storage. Microporous and Mesoporous Materials. 2009;120(3):267-71.

[19] Vakifahmetoglu C, Presser V, Yeon S-H, Colombo P, Gogotsi Y. Enhanced hydrogen and methane gas storage of silicon oxycarbide derived carbon. Microporous and Mesoporous Materials. 2011;144(1–3):105-12.

[20] Borchardt L, Hasché F, Lohe MR, Oschatz M, Schmidt F, Kockrick E, et al. Transition metal loaded silicon carbide-derived carbons with enhanced catalytic properties. Carbon. 2012;50(5):1861-70.

[21] Krawiec P, Kockrick E, Borchardt L, Geiger D, Corma A, Kaskel S. Ordered Mesoporous Carbide Derived Carbons: Novel Materials for Catalysis and Adsorption. The Journal of Physical Chemistry C. 2009;113(18):7755-61.

[22] Kockrick E, Borchardt L, Schrage C, Gaudillere C, Ziegler C, Freudenberg T, et al. CeO2/Pt Catalyst Nanoparticle Containing Carbide-Derived Carbon Composites by a New In situ Functionalization Strategy. Chemistry of Materials. 2010;23(1):57-66.

[23] Seredych M, Portet C, Gogotsi Y, Bandosz TJ. Nitrogen modified carbide-derived carbons as adsorbents of hydrogen sulfide. J Colloid Interface Sci. 2009;330(1):60-6.

[24] Mangarella MC, Ewbank JL, Dutzer MR, Alamgir FM, Walton KS. Synthesis of Embedded Iron Nanoparticles in Fe3C-derived Carbons. Carbon. 2014;79:74-84.

[25] Brunauer S, Deming LS, Deming WE, Teller E. On a theory of the van der Waals adsorption of gases. Journal of the American Chemical Society. 1940;62:1723-32.

[26] Brunauer S, Emmett PH, Teller E. Adsorption of gases in multimolecular layers. Journal of the American Chemical Society. 1938;60:309-19.

[27] Kruk M, Jaroniec M. Gas adsorption characterization of ordered organic-inorganic nanocomposite materials. Chemistry of Materials. 2001;13(10):3169-83.

[28] Rasmussen CJ, Vishnyakov A, Thommes M, Smarsly BM, Kleitz F, Neimark AV. Cavitation in Metastable Liquid Nitrogen Confined to Nanoscale Pores. Langmuir. 2010;26(12):10147-57.

[29] Kleitz F, Bérubé Fo, Guillet-Nicolas Rm, Yang C-M, Thommes M. Probing Adsorption, Pore Condensation, and Hysteresis Behavior of Pure Fluids in Three-Dimensional Cubic Mesoporous KIT-6 Silica. The Journal of Physical Chemistry C. 2010;114(20):9344-55.

[30] Thommes M, Smarsly B, Groenewolt M, Ravikovitch PI, Neimark AV. Adsorption Hysteresis of Nitrogen and Argon in Pore Networks and Characterization of Novel Micro- and Mesoporous Silicas. Langmuir. 2005;22(2):756-64.

[31] Jänes A, Thomberg T, Lust E. Synthesis and characterisation of nanoporous carbide-derived carbon by chlorination of vanadium carbide. Carbon. 2007;45(14):2717-22.

[32] Neimark AV, Lin YZ, Ravikovitch PI, Thommes M. Quenched solid density functional theory and pore size analysis of micro-mesoporous carbons. Carbon. 2009;47(7):1617-28.

[33] Leis J, Perkson A, Arulepp M, Nigu P, Svensson G. Catalytic effects of metals of the iron subgroup on the chlorination of titanium carbide to form nanostructural carbon. Carbon. 2002;40(9):1559-64.

[34] Xu J, Zhang R, Ge S, Wang J, Liu Y, Chen P. Effect of iron catalyst on the microstructure and electrochemical properties of vanadium carbide-derived carbons. Materials Chemistry and Physics. 2013;141(1):540-8.

[35] Jeong J-H, Bae H-T, Lim D-S. The effect of iron catalysts on the microstructure and tribological properties of carbide-derived carbon. Carbon. 2010;48(12):3628-34.

[36] Tuinstra F, Koenig JL. Raman Spectrum of Graphite. The Journal of Chemical Physics. 1970;53(3):1126-30.

[37] Wang Y, Alsmeyer DC, McCreery RL. Raman spectroscopy of carbon materials: structural basis of observed spectra. Chemistry of Materials. 1990;2(5):557-63.

[38] Sadezky A, Muckenhuber H, Grothe H, Niessner R, Pöschl U. Raman microspectroscopy of soot and related carbonaceous materials: Spectral analysis and structural information. Carbon. 2005;43(8):1731-42.

[39] Dresselhaus MS, Dresselhaus G. Light scattering in graphite intercalation compounds. In: Cardona M, Güntherodt G, eds. Light Scattering in Solids III: Springer Berlin Heidelberg 1982, p. 3-57.

[40] Cuesta A, Dhamelincourt P, Laureyns J, Martínez-Alonso A, Tascón JMD. Raman microprobe studies on carbon materials. Carbon. 1994;32(8):1523-32.

[41] Dippel B, Jander H, Heintzenberg J. NIR FT Raman spectroscopic study of flame soot. Physical Chemistry Chemical Physics. 1999;1(20):4707-12.

[42] Jawhari T, Roid A, Casado J. Raman spectroscopic characterization of some commercially available carbon black materials. Carbon. 1995;33(11):1561-5.

[43] Beyssac O, Goffé B, Petitet J-P, Froigneux E, Moreau M, Rouzaud J-N. On the characterization of disordered and heterogeneous carbonaceous materials by Raman spectroscopy. Spectrochimica Acta Part A: Molecular and Biomolecular Spectroscopy. 2003;59(10):2267-76.

[44] Sharonov VE, Aristov YI. Ammonia adsorption by MgCl2, CaCl2 and BaCl2 confined to porous alumina: the fixed bed adsorber. Reaction Kinetics and Catalysis Letters. 2005;85(1):183-8.

[45] Portet C, Kazachkin D, Osswald S, Gogotsi Y, Borguet E. Impact of synthesis conditions on surface chemistry and structure of carbide-derived carbons. Thermochimica Acta. 2010;497(1-2):137-42.

[46] Bremm S, Meyer G. Reactivity of ammonium halides: Action of ammonium chloride and bromide on iron and iron (III) chloride and bromide. Zeitschrift für anorganische und allgemeine Chemie. 2003;629(10):1875-80.

[47] Miller FA, Wilkins CH. Infrared Spectra and Characteristic Frequencies of Inorganic Ions. Analytical Chemistry. 1952;24(8):1253-94.

[48] Seredych M, Bandosz TJ. Combined Role of Water and Surface Chemistry in Reactive Adsorption of Ammonia on Graphite Oxides. Langmuir. 2010;26(8):5491-8.

CHAPTER 5

EFFECT OF PORE SIZE ON ACID FUNCTIONALIZED MO2C-DERIVED CARBONS FOR AMMONIA ADSORPTION

5.1 Summary

Carbide-derived carbons were synthesized by chlorinating Mo_2C at temperatures ranging from 500-900^oC. The chlorination temperature was varied to create carbide-derived carbons with unique micro, micro/meso, and mesoporous pore structures. Sulfuric and nitric acid treatments were performed to graft acidic functional groups on the carbon surface to provide specific interactions with NH_3. Acid-treated Mo_2C-CDC were evaluated in dynamic NH_3 breakthrough experiments and shown to have exceptional breakthrough capacities in both dry (0% RH) and humid (75% RH) environments. Acidic groups were characterized by X-ray Photoelectron Spectroscopy (XPS), Boehm Titration, and Fourier Transform Infrared Spectroscopy (FTIR) to normalize the performance of acid-treated Mo_2C-CDC on a per acid group basis and understand the unique mechanisms within each pore structure. From these results, it was suggested that acidic functional groups are best utilized in predominately microporous structures for NH_3 adsorption under both dry and humid conditions. Specific interactions between NH_3 and surface carboxyl, ester, and nitrate groups are hypothesized to contribute to high dynamic loadings for CDC adsorbents.

5.2 Introduction

Ammonia is a highly toxic and corrosive gas that is a key component within the agriculture and chemical industries. It is heavily produced for its essential role in

fertilizer within agriculture, and also found as a significant emitted compound from livestock and wastewater. Even at low concentrations, ammonia can negatively impact the growth and health of livestock as well as the well-being of industrial workers that are responsible for its transportation, use, and removal.[1] The US Occupational Safety and Health Administration (OSHA) has set a permissible exposure limit (PEL) for ammonia at 50 ppm, highlighting the need to separate any appreciable concentration of ammonia from air.[2] Due to its small size and high vapor pressure, ammonia remains a challenging gas for common adsorbents to adequately remove at ambient conditions.

Carbide-derived carbons are highly tunable porous carbons derived from a carbide precursor. Typically, high temperature chlorination is used to selectively extract the metal atom as a volatile metal chloride, allowing the remaining carbon to form a porous network with specific surface areas exceeding 2000 $m^2 g^{-1}$. It has been extensively shown that the size and distribution of these pores can be tuned with great precision through either careful choice of the carbide precursor or the chlorination temperature.[3-8] Many carbide precursors exhibit narrow pore size distributions and high bulk porosity over a wide chlorination temperature range. These features, combined with the high tailorability of their pore size, allow CDCs to be excellent adsorbent materials and fundamental materials for physical structure property relationships in adsorptive applications. Studies on both CO_2 and H_2 storage have used CDC materials with various pore size distributions to present strong evidence that ultra-micropores contribute most to the storage of these small gases in CDC adsorbents.[9-11]

Pore size has also been hypothesized to play a role in dynamic NH_3 adsorption, but the relationship between pore size and NH_3 adsorption is more complex, specifically

in humid environments.[12, 13] Intuitively, the small diameter of ammonia, 3Å, requires the presence of ultra-micropores to provide adequate non-specific interactions. However many adsorbents, even those exhibiting high microporosity, typically have poor NH_3 performance in the absence of chemical specific functionalities. The need for specific interactions present within these micropore spaces is crucial to effectively bind NH_3 to the surface under dry conditions. The co-adsorption of water within the pore structure is also important to consider. Under humid conditions, the presence of water has shown to greatly enhance the dynamic loading of ammonia.[12] Due to ammonia's high polarity and its ability to form hydrogen bonds, it is highly soluble in co-adsorbed water. The deprotonation of acidic functional groups, such as carboxylic acids, in aqueous environments can also allow the facilitation of acid-base interactions between ammonium and the conjugate bases of acidic functional groups on the carbon surface. The role of pore size for the adsorption of water is also important. Water is best able to cluster in small pores, starting with the formation of hydrogen bonds with oxygen functionalities on the carbon surface.[14, 15] In addition, the size of these pores should be large enough to include acidic functional groups, and the adsorption of water and ammonia. It has been estimated that this ideal size is about 2-3 nm in diameter.[12, 16]

Initial studies on CDCs have demonstrated the surface chemistry of these materials can be tuned through acidic treatment and the addition of nitrogen groups for separations and storage applications.[17, 18] The tunable pore size inherent to CDCs is ideal to systematically determine the ideal pore architecture for the separation of ammonia from both dry and humid air streams. In this study, a series of Mo_2C-CDC were prepared at different chlorination temperatures to synthesis adsorbents with unique micro,

micro/meso, and mesoporous pore architectures. Mo_2C was chosen as the carbide precursor due to the high bulk porosity of Mo_2C-CDCs over a large chlorination temperature range.[19, 20] In addition, the pore structure of Mo_2C-CDC is highly tunable, from predominately microporous to predominately mesoporous. Prepared Mo_2C-CDCs were acid treated stepwise with both concentrated sulfuric and nitric acid to graft functional groups on the surface. The amount and type of these acidic functional groups were characterized by various titration and spectroscopic methods, and the ammonia breakthrough results were normalized by these acidic characteristics to selectively determine the role of pore size under both dry and humid conditions. Exhausted samples were characterized to provide insight into the specific adsorptive interactions taking place within each pore structure.

5.3 Materials and Methods

5.3.1 Materials

5.3.1.1. Mo_2C-derived Carbon Synthesis

Carbide-derived carbons were prepared using one gram of Mo_2C (Sigma Aldrich 99.5% purity −325 mesh). The carbide precursor was spread out on a quartz boat and inserted into a quartz tube of ID 1", length 20" and into a horizontal tube furnace. Samples were heated to a reaction temperature of 500^{o}C, 700^{o}C, or 900^{o}C at a ramp rate of 5^{o}C min^{-1} under 100 ml min^{-1} of Ar flow (Airgas 99.999%). After reaching the desired chlorination temperature, chlorine gas (Airgas 99.5%) was introduced into the reactor at a flow rate of 25 ml min^{-1} for 2, 3, or 4 hours, for 500 ^{o}C, 700 ^{o}C, or 900 ^{o}C respectively, while the Ar flow was maintained at 100 ml min^{-1}. The chlorination time was increased to

ensure complete etching of the carbide precursor at lower temperatures. A scrubber solution of concentrated NaOH was used to neutralize acidic gases present in the effluent stream, including Cl_2, HCl, and molybdenum chlorides.

After the chlorination time had elapsed the chlorine gas flow was turned off and samples were cooled or heated to 600^{o}C at a ramp rate of 5^{o}C min^{-1} under Ar flow. The Ar flow was then switched to 5% H_2 in Ar (Airgas 99.999%) at a rate of 100 ml min^{-1} for 3 hours at 600^{o}C to anneal the CDC materials and remove residual chlorine. At the end of the annealing treatment, these samples were cooled to room temperature under Ar flow. These samples are referred to as "annealed" molybdenum carbide derived carbons and were labeled as M-CT, where CT denotes the chlorination temperature.

5.3.1.2. Mo_2C-CDC Acid Treatment

Mo_2C-CDCs were prepared batch-wise according to the procedure in the previous section until a batch size of 250 mg was attained at all chlorination temperatures. Each batch was verified by N_2-sorption at 77K, and Powder X-ray Diffraction (PXRD) to be structurally and porosimetrically equivalent. Energy dispersive spectroscopy (EDS) was used to verify that all batches were fully etched, and did not include any residual Mo_2C. For the acid treatment, 7 mL of a 13M stock solution of H_2SO_4 was added to 200 mg of each Mo_2C-CDC and heated at 70^{o}C in an oil bath for 6 hours. The temperature was subsequently raised to 100^{o}C and held for 12 hours. Samples were then transferred to rotary oven in a 45 mL teflon-lined acid digestion vessel for 12 hours at 200^{o}C. Finally, samples were added to 7 mL of a 15M stock solution of HNO_3 and heated to 70^{o}C in an oil bath for 6 hours. After each treatment, samples were diluted and decanted stepwise with copious amounts of distilled water. Once the decanted liquid reached a minimum pH

of 3, the samples were filtered and repeatedly washed with distilled water until the filtrate reached a neutral pH. Scanning electron microscopy (SEM) images were taken before and after to verify that the resulting acid treated samples did not include any remnants of filter paper. These samples were labeled M-CT-S-N to signify the acidification via both sulfuric acid and nitric acid.

5.3.2 Methods

Power X-ray Diffraction (PXRD) patterns were collected using an X'Pert X-ray PANalytical diffractometer using a Cu Kα X-ray source (λ = 1.5418 Å) and an X'accelerator module. PXRD spectrums were collected at room temperature from a range of 4-90^{o} in two theta (2θ) with a step size of 0.02^{o}. Nitrogen sorption measurements were obtained on a Quadrasorb System from Quantachrome Instruments, and used to calculate specific surface area, pore volume, and pore size distribution. Approximately 30-50mg of each sample was activated overnight at 423K under vacuum and isotherms were collected at 77K. Specific surface areas were calculated using the BET model under the pressure range 0.01-0.05 P/P_0. Pore size distributions for all samples were obtained using the Quenched Solid Density Functional Theory (QSDFT) model in version 5.11 of the QuadraWin^{TM} software. Parameters for the QSDFT model were chosen depending on the characteristics of the isotherm. For microporous, type I isotherms, a slit-pore model, nitrogen adsorbate, and carbon adsorbent were assumed for the QSDFT model. Whereas, for type IV isotherms that exhibited characteristic cavitation effects, an adsorption branch slit-pore/cylindrical pore model was used with an assumed nitrogen adsorbate and carbon adsorbent.

Scanning electron microscopy (SEM) images were obtained using a LEO 1530 Thermally-Assisted Field Emission (TFE) Scanning Electron Microscope (SEM). All samples were deposited onto carbon tape and not sputter coated prior to scanning. Images were scanned at an accelerating voltage of 10kV. Quantitative chemical analysis of select samples was conducted utilizing an Oxford-7426 EDS detector attached to the LEO 1530 TFE SEM. At least three separate spots were surveyed for each sample.

Boehm titration was performed to quantify the amount of acidic functional groups.[21-23] Briefly, 50 mg of each sample was added to a 0.01M solution of NaOH. The solution was shaken for 24 h and filtered. 10 mL aliquots of the filtrate solution were collected, and 20 mL of a 0.01M HCl solution was added. N_2 was bubbled through the solutions for 2h to remove CO_2 and the solutions were subsequently back titrated with a 0.01M NaOH solution. A pH probe was used to monitor the endpoint of the titration at pH = 7.0 under constant stirring.

X-ray Photoelectric Spectroscopy (XPS) measurements were taken on a Thermo K-alpha XPS, monochromated Al Kα source with a double-focusing hemispherical analyzer. High resolution spectra were taken of C1s, O1s, N1s with 30 total scans at 0.1 eV step size, 50 ms dwell time, 50 eV pass energy, and 400 μm spot size. A total of 10 survey scans were used to quantify the surface elemental concentration. A Magna 560 FTIR (Nicolet Instruments) was used to collect FTIR spectra. FTIR samples were prepared by diluting CDC powder with KBr in a 1:200 ratio and then pressed into a 13 mm disk. Absorbance data was averaged over 128 scans at a resolution of 2 cm^{-1}. A fresh background scan was taken and subtracted before each sample.

For ammonia breakthrough experiments, samples were evaluated on our experimental setup described in **Chapter 2,** under **Figure 2.2** and **Figure 2.3**. Mo_2C-CDC powder was packed within a quartz bed against a fine quartz frit of ID 4 mm to a standardized bed volume of $55mm^3$. Samples were activated under 50 ml min^{-1} N_2 flow at 150^oC for 2 hours and then allowed to cool back down to room temperature for 30-45 minutes. A dilute concentration of ammonia was flowed through the quartz bed at a flow rate of 20 ml min^{-1}. Breakthrough experiments were run under dry (0% RH) and humid (75% RH) conditions; humid conditions were achieved through the use of a water bubbler. The ammonia concentration for dry and humid runs was 1500 ppm and 1431 ppm, respectively. The dry run was started by switching the N_2 to a stream of 1500 ppm NH_3 in air at a rate of 20 ml min^{-1} (Airgas). For a humid breakthrough run, a humid stream was created by flowing air at 16 ml min^{-1} through a H_2O bubbler, and then combining it with a NH_3 stream of 7155 ppm in air at a flow rate of 4 ml min^{-1}. The effluent stream was analyzed using an Analytical Technology H10-15 ammonia electrochemical sensor. Once the dilute NH_3 stream was switched on, data points were taken at 30 second intervals until the sensor reached 500 ppm NH_3, at which point the NH_3 was switched off to preserve the life of the sensor. N_2 flow was maintained at 50 ml min^{-1} to capture the desorption behavior of the bed, and the sensor reading was recorded until the NH_3 concentration returned to ~100 ppm. A blank bed of sand was used to calculate the dead time within the system, and was subtracted from the breakthrough time of evaluated samples. No significant pressure drop was noted for these conditions. The procedure for wet and dry conditions was identical. The activated mass was used in performance normalization calculations.

5.4 Results and Discussion

5.4.1 Physical Properties of Mo_2C-CDCs Before and After Acidification

Molybdenum was selectively etched from Mo_2C in the following reaction scheme to create Mo_2C-CDC:

$$Mo_2C + 5Cl_2 \rightarrow 2MoCl_2 + C \quad (1)$$

Mo_2C-CDCs were synthesized at different chlorination temperatures and annealed with H_2 to remove residual chlorine species and maximize available surface area.[24] The chlorination temperature significantly affects the bulk porosity and pore size distributions of CDCs. Acidified Mo_2C-CDC-S-N were synthesized by subjecting each carbide-derived carbon to a strong oxidative treatment in concentrated H_2SO_4 and HNO_3. Acidification is known to cause pore blockage and possible degradation of the carbide-derived carbon framework. In addition, the additional mass of functional groups that do not contribute additional porosity can reduce the specific surface area, as it on a mass basis. Both of these effects were investigated through nitrogen sorption and Quenched Solid Density Function Theory (QSDFT). Nitrogen isotherms at 77K can be seen in **Figure 5.1** for both as-synthesized untreated Mo_2C-CDCs and treated Mo_2C-CDC-S. Pore size distributions for both series of samples are presented in **Figure 5.2**. Bulk porosity can be found in **Table 5.1**.

In **Figure 5.1**, the shape of the nitrogen isotherm was seen to be strongly dependent on the chlorination temperature. M-500C has a characteristic Type I isotherm shape by Brunauer classification, indicating a microporous structure.[25-27] As the

chlorination temperature increases, there is a growing hysteresis loop present in M-700C and M-900C's nitrogen isotherm, and both samples resemble a type VI isotherm with a triangular H2 hysteresis loop according to IUPAC classification. This hysteresis is likely caused by the presence of cavitation effects. The rapid pore emptying of nitrogen at relative pressure = 0.42 is characteristic of the tensile stress limit of the condensed nitrogen fluid.[28-30] Since this rapid desorption is caused by the thermo-physical properties of the fluid, and not characteristic of the pore structure, only the adsorption branch for M-700C and M-900C was used in subsequent QSDFT calculations. Untreated Mo_2C-CDCs show high bulk porosity at all three chlorination temperatures, with M-700C having the greatest specific surface area of 1793 m^2 g^{-1}. M-700C and M-900C have similarly high pore volumes of 1.63 cc g^{-1}. M-500C exhibits a high surface area of 1457 m^2 g^{-1}, but comparatively smaller total pore volume, and appears highly microporous from the isotherm shape. These results are in good agreement with previous investigations on Mo_2C-CDCs.[19, 20]

Table 5.1. Porosity and residual metal for prepared Mo_2C-CDCs

Sample Name	Specific Surface Area (m^2 g^{-1})[a]	Pore Volume (cc g^{-1})[b]	V_{micro}	V_{meso}	Micropore Volume (%)	V_{micro} change (%)	V_{meso} change (%)
M-500C	1457	1.05	0.73	0.23	69.5	-	-
M-700C	1793	1.61	0.45	1.05	28.0	-	-
M-900C	1141	1.63	0.16	1.38	9.8	-	-
M-500C-S-N	557	0.26	0.25	0.01	96.2	-65.7	-95.7
M-700C-S-N	773	0.41	0.27	0.10	65.9	-40.0	-90.5
M-900C-S-N	714	0.74	0.17	0.52	23.0	6.3	-62.3

a)Obtained by BET Analysis at a Relative Pressure Range of 0.01-0.05 P/P0 [22, 23] b) Obtained at P/P0 = 0.99

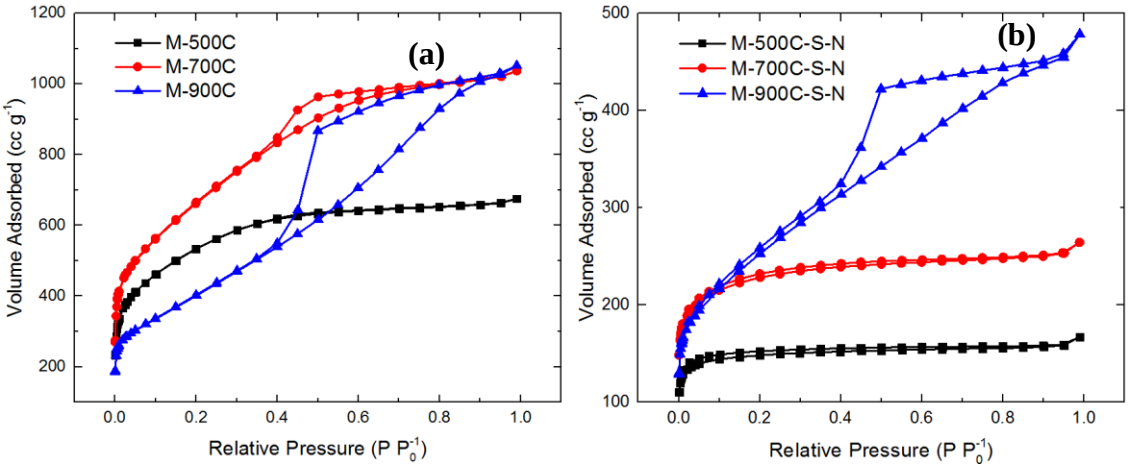

Figure 5.1 Nitrogen Adsorption Isotherms for (a) Untreated Mo_2C-CDCs and (b) Acid-Treated Mo_2C-CDCs

Pore size distributions in **Figure 5.2** show distinct differences between the pore structures of synthesized Mo_2C-CDCs. M-500C is mainly a microporous structure, with almost all pores less than 3 nm in diameter. As the chlorination temperature increases, increased mesoporosity is seen in M-700C and M-900C. M-700C features a large amount of micropores and small mesopores from 2-5 nm diameter. M-900C is largely mesoporous, with a wide peak of mesopores between 3 – 12 nm in diameter. This increase in mesoporosity correlates well with the gradual shift from Type I to Type IV isotherm at increasing chlorination temperatures. In **Table 5.1**, drastic differences occur in the percentage of total pore volume resulting from micropores (diameter < 2 nm). Chlorination at 500 ^{o}C results in 69.5% microporous pore volume, while M-900C total pore volume only exhibits a 9.8% contribution from its micropores.

After acidification, there are notable changes in the bulk porosity, isotherm shape, and pore size distribution of Mo_2C-CDCs. As expected, the surface area decreases after acidification. The volume of micropores and mesopores, V_{micro} and V_{meso} respectively, both decrease significantly after acidification for all samples except for M-900C-S-N. This decrease is likely caused by three factors. First, the additional mass of functional

groups that do not add porosity dilute the overall pore volume on a mass basis. Second, a percentage of mesopores are likely converted to micropores after the addition of functional groups within the pore space. The increase in V_{micro} for M-900C-S-N supports that there are functional groups grafted within the pore space, especially considering the first mass dilution effect. Third, some pore blockage and pore degradation is suggested to cause some porosity loss. From the pore size distributions in **Figure 5.2**, there are several changes within specific pore sizes for these samples. In general, the small mesopores (2-5 nm in diameter) seem to completely shift or experience blockage/degradation after acidification. The mesopores present in this range for M-500C are completely absent in M-500C-S-N's pore size distribution, and only a small broad peak from 2-3 nm is noted from M-700C-S-N. More striking is the difference in isotherm shape for M-700C, which shifts from a Type IV isotherm to a Type I after acidification. The hysteresis loop present in M-700C due to cavitation is no longer seen in the isotherm after acidification. It is possible that functional groups are now present in the large main pore cavity, reducing its size and removing the cavitation effect. It is also likely that in some ink-bottle type pores, the small neck is now blocked by these functional groups.

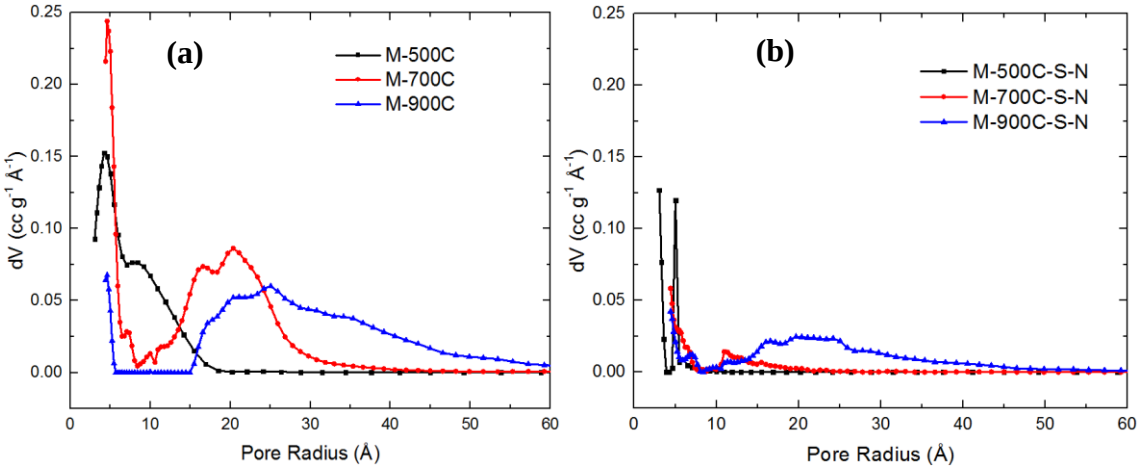

Figure 5.2 Pore size distributions for (a) Untreated Mo_2C-CDCs and (b) Acid-Treated Mo_2C-CDCs

5.4.2 Acid Group Functionalities after acidification of Mo_2C-CDCs

Acidification through subsequent sulfuric acid and nitric acid treatment severely altered the surface chemistry of Mo_2C-CDCs. Elemental data from XPS survey scans in **Table 5.2**, shows drastic increases in oxygen content for all samples. There is also an increase in nitrogen content for M-500C-S-N and M-700C-S-N. Relatively little difference is seen in the XRD patterns in **Figure 5.3**, the broad (002) reflection of M-900C-S-N is still preserved after acidification, indicating no severe changes in carbon structure. As XRD only shows quite amorphous structures for untreated Mo_2C-CDCs, the resulting differences in surface species are best observed in the FTIR spectra in **Figure 5.4**. Little significant functional groups were observed in Mo_2C-CDCs prior to acidification, and XPS data confirms that Mo_2C-CDCs have relatively little oxygen and no nitrogen content before acidification. There is a trend of increasing oxygen content at lower chlorination temperatures for untreated Mo_2C-CDCs. This has previously been seen in the literature for other carbide-derived carbons.[3, 24] One possible explanation is that there are more dangling bonds present in CDCs chlorinated at lower temperatures due to the reduced mobility of carbon. Oxygen is then able to form functionalities on the surface post-synthesis after reintroduction of ambient air. Although carbides typically have a layer of respective metal oxide after passivation, it is unlikely that any oxygen containing species originating from the carbide precursor are able to retained at such high chlorination and annealing temperatures.

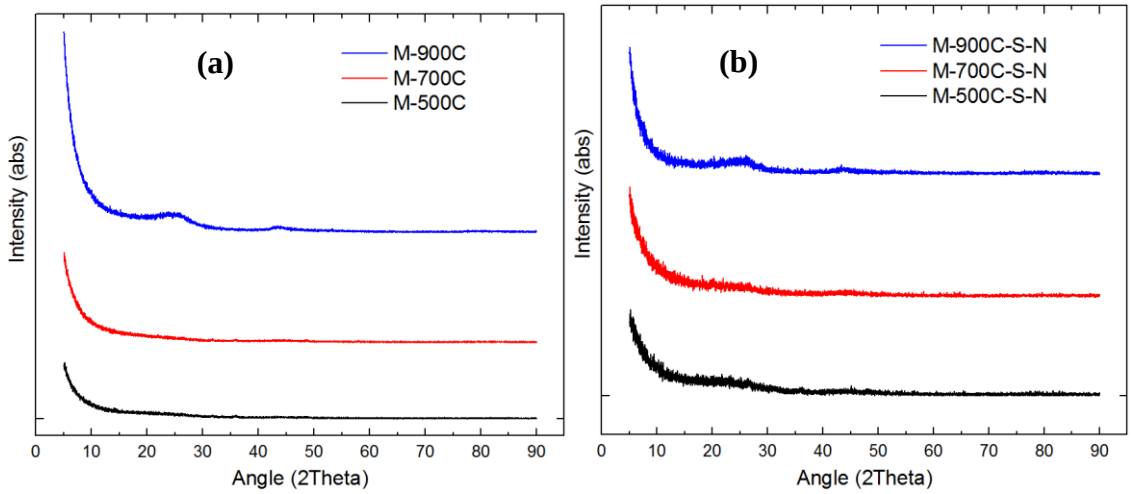

Figure 5.3 X-ray Diffraction Spectra for (a) Untreated Mo_2C-CDCs and (b) Acid-Treated Mo_2C-CDCs

After acidification, several groups are present in the FTIR spectra, seen in **Figure 5.4(b)** and XPS spectra in **Figure 5.5**. Although FTIR is not quantitative, the relative intensities in the FTIR spectra for treated Mo_2C-CDCs reflect greater oxidation for samples chlorinated at lower temperatures. The intensities of these peaks match well with the mass percentage of oxygen determined by XPS. There is a correlation between chlorination temperature and degree of oxidation; as the chlorination temperature decreases the extent of oxidation increases. It is suggested that the oxygen species present after chlorination could cause greater differences in electronegativity on the carbon surface, facilitating easier attack by oxidative agents. In addition, at lower chlorination temperatures there is less reorganization of carbon, which could provide easier sites of attack for the formation of carbonyl and hydroxyl groups, similar to the fashion in which these groups are first added on amorphous sites on carbon nanotubes.

Table 5.2. XPS for prepared and treated Mo_2C-CDCs

Sample Name	Amount C (wt %)	Amount O (wt %)	Amount N (wt %)	Amount S (wt %)	Amount Mo (wt %)
M-500C	96.51	3.49	0.0	0.0	0.0
M-700C	98.39	1.61	0.0	0.0	0.0
M-900C	99.31	0.69	0.0	0.0	0.0
M-500C-S-N	75.98	22.16	1.86	0.0	0.0
M-700C-S-N	84.10	14.54	1.24	0.12	0.0
M-900C-S-N	95.82	4.18	0.0	0.0	0.0

A peak at ~1725 cm^{-1} was present for all samples and quite sharp for M-700-S-N and M-500C-S-N. This peak was assigned to the C=O stretch for carboxylic acids and ketones.[28] This vibration was not assigned to the C=O stretch in aldehydes, as this would be accompanied by two bands for the C-H stretch in the 2830-2695 cm^{-1} region: the fundamental aldehydic C-H stretch and the first overtone of the C-H bending vibration due to Fermi resonance. Another aldehyde band, present around 2720 cm^{-1}, is also absent in the spectra of treated Mo_2C-CDCs suggesting that aldehyde groups are not present.[32] M-500C-S-N and M-700C-S-N feature a broad band centered at 3410 cm^{-1} ranging from 3000 – 3670 cm^{-1}. This band was assigned to O-H stretching modes, and it is likely that there is a large contribution from hydroxyl functional groups. The peaks at 1220 cm^{-1}, 1230 cm^{-1}, and 1240 cm^{-1} for M-900C-S-N, M-700C-S-N, and M-500C-S-N are most likely due to the C-O stretch for carboxylic acids. In all samples there is another strong peak at ~1600 cm^{-1} that gradually "shifts" from lower to higher wavenumbers with decreasing chlorination temperature, from 1580 cm^{-1} to 1590 cm^{-1} to 1615 cm^{-1} in M-900C-S-N, M-700C-S-N, and M-500C-S-N respectively. This peak is tentatively assigned to aromatic ring stretching modes or highly conjugated carbonyl groups.[33] In

M-500C-S-N a small unique peak is observed at 1383 cm^{-1} – this peak is tentatively assigned to the asymmetrical stretch of nitrate groups in nitroalkanes.[32]

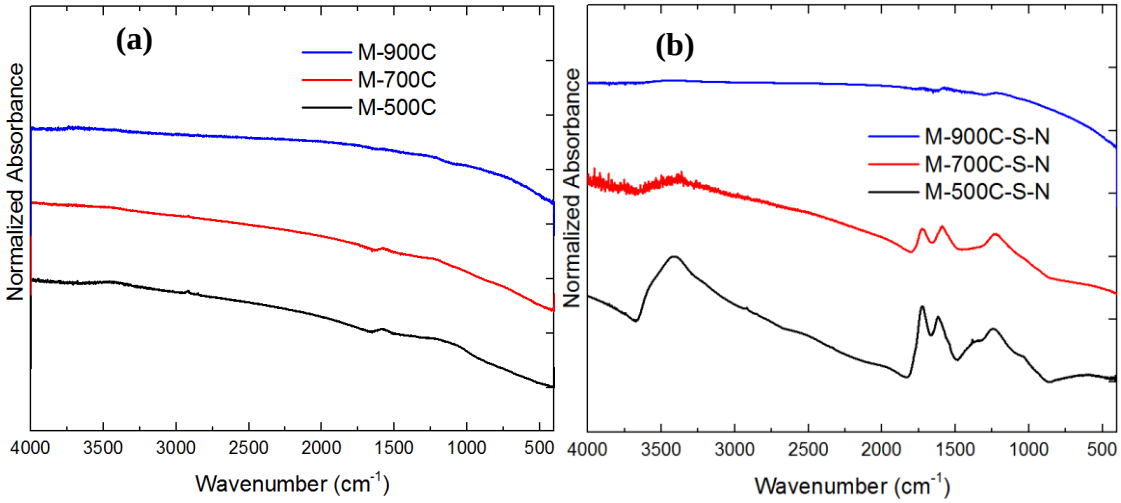

Figure 5.4 FTIR spectra (a) Untreated Mo_2C-CDCs and (b) Acid-Treated Mo_2C-CDCs

XPS deconvolutions in **Figure 5.5**, show the presence of functional groups within the C1s, O1s, and N1s spectra. No significant contribution was seen in the S2p spectra, and no residual chlorine or molybdenum was observed in any of the acidified samples. A split peak is observed for the N1s spectra for M-500C-S-N and M-700C-S-N. The first peak at 400.1 eV and 400.5 eV for M-500C-S-N and M-700C-S-N corresponds to N-H bonds, pyrrolic, and pyridine nitrogen, while a second peak present at 405.5 eV and 405.76 eV is assigned to nitrate groups.[34] Only instrumental noise is observed for the M-500C-S-N N1s spectrum. The O1s spectra was deconvoluted into three peaks for all samples. The first peak is present at ~531.2 eV for all treated samples and is assigned to carbonyl groups likely present in carboxylic acids and ketone groups. The second peak, present at ~532.6 eV, is assigned to C-O present in epoxy, phenol, and carboxyl groups.[34, 35] Finally, the third peak centered ~ 536.4 eV is likely due to chemisorbed oxygen or water that cannot be removed with ultra-high vacuum.[34, 35]

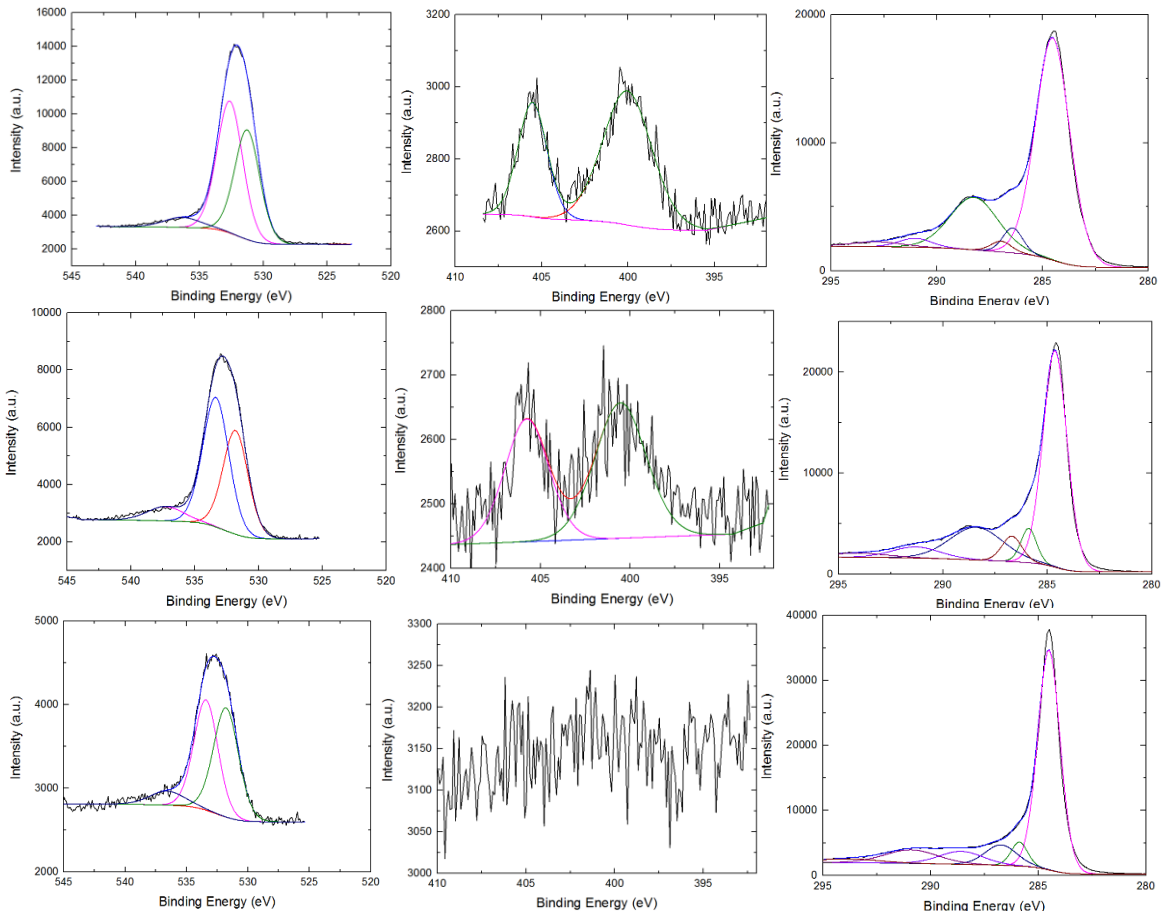

Figure 5.5 O1s, N1s, C1s XPS Spectra for M-500-S-N (top), M-700-S-N (middle), M-900-S-N (bottom)

The C1s spectra was deconvoluted into several contributions from oxygen containing functional groups. First, a large peak, corresponding to graphitic, aromatic or aliphatic carbon is seen at ~284.5 eV for all three acidified samples. The peak at ~286.0 eV is assigned to the C-O bond in hydroxyl groups. The next peak present at ~287.0 eV is assigned to carbonyl groups, and possible -C-N present in nitrogen containing M-500C-S-N and M-700C-S-N. There is a large peak present at ~288.4 eV assigned to the carbonyl group present in ketones, carboxylic acids, and esters. The peak at ~289.9 eV is assigned to carboxylic acids (O-C=O) and the satellite peak of the π–π* transition for aromatic carbon. Finally, the shoulder at ~293.0 eV is assigned to the plasmon band.

There are marked differences for C1s spectrum for acidified Mo_2C-CDCs. The increase in intensity for the ~288.4 eV peak assigned to C=O in ketones, carboxylic acids, and esters correlates well with the intensity of the C=O stretch for carboxylic acids and ketones seen in the FTIR spectra. The relative intensity of this peak also suggests a greater degree of acidification with decreasing chlorination temperature.

5.4.3 Ammonia Breakthrough Experiments for Mo_2C-CDCs

Ammonia dynamic adsorptive performance was tested under both dry and wet conditions for treated and untreated samples and the results are summarized in **Table 5.3**. Before acidification, Mo_2C-CDCs exhibit nearly instantaneous breakthrough in dry conditions, and marginally better performance with the addition of water in humid environments. Despite exceptional bulk porosity, Mo_2C-CDCs can retain very little ammonia regardless of their pore size. Without the addition of specific interactions via acidifications, untreated samples cannot effectively bind ammonia to the surface. There is a slight trend of increased capacity with increasing microporosity, particularly under humid conditions. Water adsorbs more efficiently in small micropores, and it is likely that the higher volume of micropores and high amount of oxygen functionalities together increase the dynamic capacity for M-500C and M-700C. Breakthrough adsorption curves for both wet and dry conditions can be seen in **Figure 5.6**.

Dry and humid dynamic loadings for all samples drastically increased after acidification. M-500C-S-N exhibits the best dynamic capacity, adsorbing 4.95 mmol NH_3 and 6.01 mmol NH_3 per gram adsorbent under both dry and humid conditions respectively. M-700C-S-N also has great capacity with or without the presence of water, adsorbing 4.83 mmol g^{-1} and 4.85 mmol g^{-1} respectively. M-900C-S-N, which had the

lowest functionalization based on XPS and FTIR measurements, had modest performance in comparison. However, when compared to its untreated analog, M-900C-S-N had drastic improvements in both dry (0.99 mmol g^{-1}) and wet capacity (1.31 mmol g^{-1}).

Table 5.3. Dry and Humid NH_3 dynamic capacities for prepared Mo_2C-CDCs

Sample Name	Specific Surface Area (m_2 g^{-1})	Pore Volume (cc g^{-1})	Dry NH_3 Dynamic Capacity (mmol g^{-1})[a]	Humid NH_3 Dynamic Capacity (mmol g^{-1})[a]
M-500C	1457	1.05	0.21	0.37
M-700C	1793	1.61	0.05	0.28
M-900C	1141	1.63	0.00	0.07
M-500C-S-N	557	0.26	4.95	6.01
M-700C-S-N	773	0.41	4.83	4.85
M-900C-S-N	714	0.74	0.99	1.31

a) Calculated by initial breakthrough time

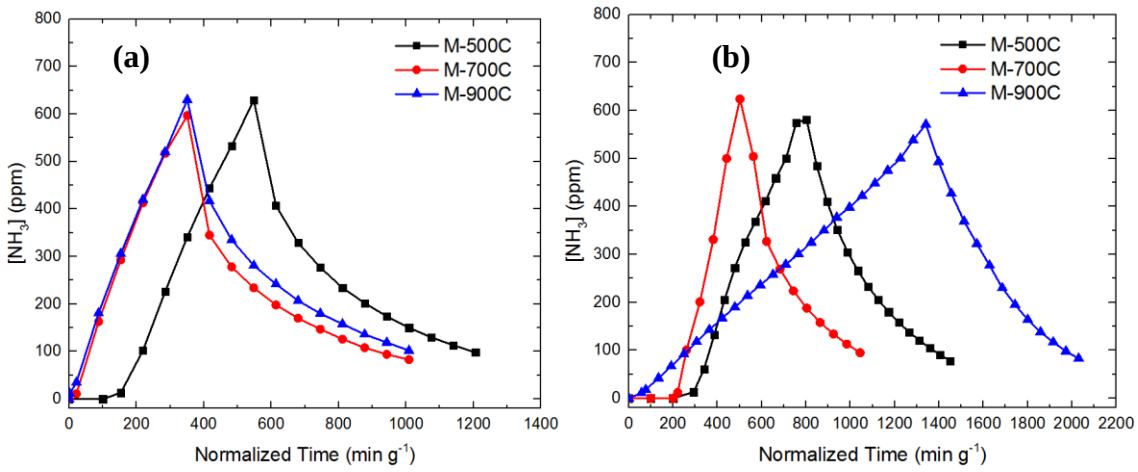

Figure 5.6 Ammonia Breakthrough Curves for Untreated Mo_2C-CDCs under (a) Dry and (b) Wet Conditions

A modified Boehm titration method was employed to quantify the total amount of acidic functional groups on the surface of treated samples and normalize breakthrough performance. Increasing acidic group content is seen at lower chlorination temperatures in **Table 5.4**, and correlates well with differences seen in the XPS and FTIR spectra of the treated samples. It is further suggested that there is a negative correlation between chlorination temperature and degree of acidification. Further identification of these

oxygen containing surface groups could not be accurately employed through Boehm titration, as nitrogen groups present in XPS have similar pKa values, preventing deconvolution of the relative amounts of lactone, phenol, and carboxylic acid groups.

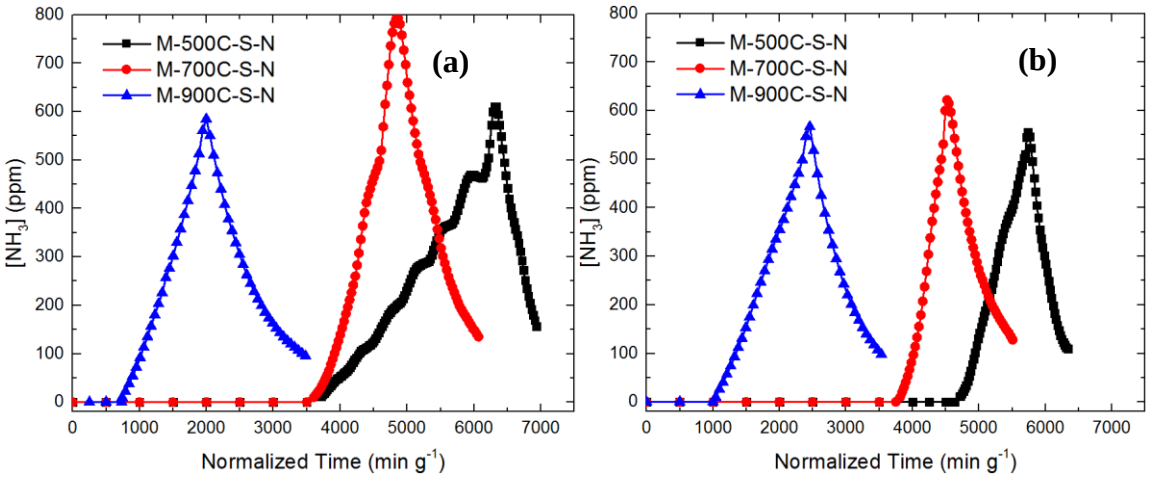

Figure 5.7 Ammonia Breakthrough Curves for Treated Mo_2C-CDCs under (a) Dry and (b) Wet Conditions

After normalization of acidic groups, predominately microporous samples are seen to perform the best under both dry and humid conditions. On a per acidic molar basis, M-900C-S-N still falls short in performance compared to M-700C-S-N and M-500C-S-N, which suggests that micropores best promote ammonia interactions with grafted acidic groups. As both the M-500C-S-N and M-700C-S-N have ammonia loadings in molar excess of their molar acidic groups under both wet and dry conditions, it is possible some ammonia is retained temporarily in small micropores within these samples or as a multilayer. Through breakthrough experiments on untreated Mo_2C-CDCs, it is clear that the presence of micropores without the presence of specific acidic groups are ineffective at binding appreciable amounts of ammonia.

An increase in capacity under humid conditions is seen for all samples. As previously mentioned, ammonia is readily soluble in co-adsorbed water films due to

hydrogen bonding. The formation of NH_4^+ upon dissolution is beneficial to reactive adsorption routes, such as facilitating acid-base interactions and the formation of an ammonium salt with deprotonated carboxylic acids. It was previously hypothesized that 2-3 nm pores would be the ideal size to accommodate water, functional groups, and ammonia.[12] M-700C-S-N had the highest volume of these pores, but exhibited slightly decreased normalized capacity when compared to M-500C-S-N. It is possible that under wet conditions, smaller micropores are more advantageous. It is interesting to note that under dry conditions, M-500C-S-N has decreased normalized capacity. The irregular shape of the breakthrough curve in **Figure 5.7(a)** suggests that at significantly small pore sizes, there could be diffusional issues that prevent efficient utilization of acidic groups. A similar, but less drastic change in slope is seen for M-700C-S-N around 4500 min g^{-1}. Comparatively worse performance was also noted for highly microporous TiC-CDCs in H_2S filtration applications.[17] In addition to diffusion limitations, the location and dispersion of the functional groups can be crucial for targeting ammonia molecules before they are able to break through the packed bed. It is possible that acidic groups are more clustered in mainly microporous supports after acidification. Groups clustered near the entrance of small micropores could then hinder both the acidification of internal porosity and the accessibility of ammonia to these inner pore spaces.

Interestingly, under humid conditions, no significant changes in slope appeared in the breakthrough curve for M-500C-S-N or M-700C-S-N. It is suggested from these results that the presence of water can either aid diffusion of ammonia in the pore space, or negate this diffusional issue through another effect. Intuitively however, the diffusion of a molecule in empty pore space should be faster than through a film. It is possible that

significant amounts of acidic functional groups on the surface of each CDC particle are able to form water films and attract ammonia to the internal pore space.

Table 5.4. Acidic Group Content in treated Mo_2C-CDCs

Sample Name	Acidic groups (mmol g^{-1})	Dry Dynamic Capacity per Acidic Group (mmol NH_3/ mmol acidic group)	Wet Dynamic Capacity per Acidic Group (mmol NH_3/ mmol acidic group)
M-500C-S-N	4.69	1.06	1.28
M-700C-S-N	4.30	1.12	1.13
M-900C-S-N	2.42	0.41	0.54

5.5 Analysis of Adsorption Mechanisms on Treated Mo_2C-CDCs

FTIR spectra were collected on dry exhausted (DE) and wet exhausted (WE) samples to probe the specific adsorption mechanisms. In **Figure 5.8**, there is a strong decrease in intensity for the peak at ~1725 cm^{-1} for all samples. This peak, previously assigned to the C=O stretch for carboxylic acids and ketones, suggests the reactive adsorption of ammonia with carboxylic acid groups. This is further supported by the decrease in intensity of the peak at 1220-1240 cm^{-1} previously assigned to the C-O stretch for carboxylic acids. The appearance of a peak at 1402 cm^{-1} is attribute to ammonium ions.[33] Ammonia is able to interact with carboxylic acids through the use of its lone pair of electrons to form an ammonium salt. The previous broad peak ranging from 3000 – 3670 cm^{-1} and centered at 3410 cm^{-1} assigned to the O-H in various environments has broadened into peaks centered at 3150 cm^{-1} and 3400 cm^{-1}. The broadening of this range is suggested by Seredych et al. to result from the conversion of esters to hydroxyl groups as ammonia is converted to surface NH_2 groups.[34] These peak positions are relatively constant for all samples, but there is an increase in intensity with decreasing chlorination temperature and from dry to humid conditions for each sample. This correlates well with the dynamic loading capacity under each respective sample and condition.

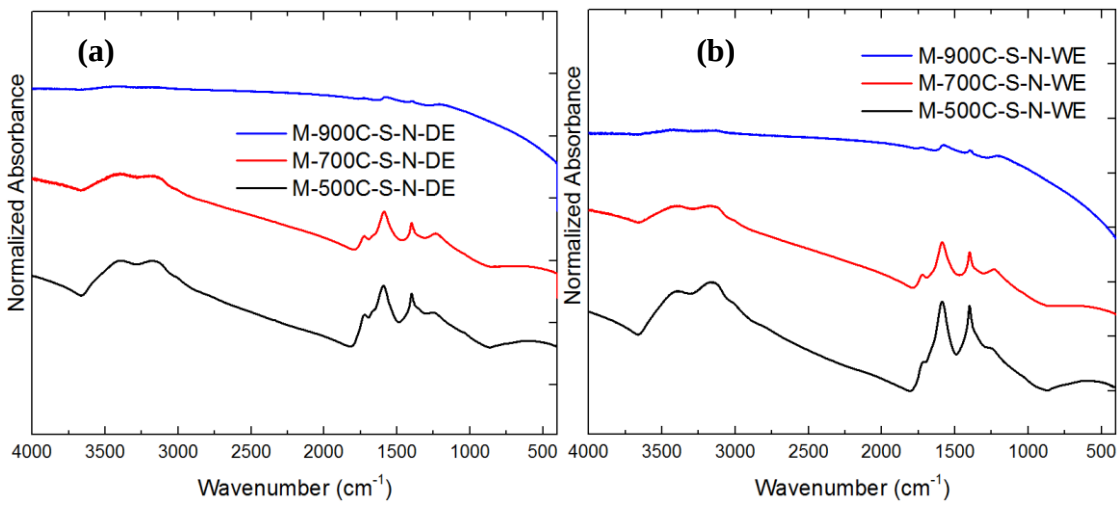

Figure 5.8 FTIR spectra (a) Dry Exhausted (DE) and (b) Wet Exhausted Samples

5.6 Conclusions

A series of Mo_2C-CDCs were chlorinated at different temperatures to produce porous carbons with unique micro, micro/meso, and mesoporous pore spaces. These as-synthesized CDCs were then subjected to sulfuric and nitric acid treatment to form acidic functional groups on the surface. It was shown through FTIR that acidic oxygen groups were able to effectively bind ammonia to the surface through reactive mechanisms. After normalization on a per acidic group basis, results suggest that a microporous and small mesoporous pore structure is ideal for ammonia adsorption on an acid functionalized carbonaceous support, as M-700C-S-N is seen to have the highest utilization of acidic functional groups. In terms of dynamic adsorption on a per mass basis, M-500C-S-N had the highest dynamic capacity under both dry (4.95 mmol g^{-1}) and humid (6.01 mmol g^{-1}) conditions. There are possible diffusion limitations noted for M-500C-S-N, and M-700C-S-N under dry conditions, due to irregular shapes in the breakthrough curve. Curiously, this is not seen in humid conditions and dynamic adsorption studies on water could potentially bring key insight into this phenomenon. For ideal performance in a dynamic

ammonia filtration process, there is likely a trade-off between effective diffusivity to active sites on the carbonaceous framework, requiring mesopores, and adequate proximity to nearby acidic groups, requiring small micropores.

5.7 References

[1] Carson T, Osweiler G, Thorne P. Adverse Health Effects. Iowa Concentrated Animal Feeding Operations Air Quality Study 2002, p. 101-42.

[2] Roney N, Llados F, Little S, Knaebel D. Toxicological Profile for Ammonia. In: Services USDoHaH, ed. 2004.

[3] Dash R, Chmiola J, Yushin G, Gogotsi Y, Laudisio G, Singer J, et al. Titanium carbide derived nanoporous carbon for energy-related applications. Carbon. 2006;44(12):2489-97.

[4] Dash RK, Yushin G, Gogotsi Y. Synthesis, structure and porosity analysis of microporous and mesoporous carbon derived from zirconium carbide. Microporous and Mesoporous Materials. 2005;86(1-3):50-7.

[5] Gogotsi Y, Nikitin A, Ye H, Zhou W, Fischer JE, Yi B, et al. Nanoporous carbide-derived carbon with tunable pore size. Nat Mater. 2003;2(9):591-4.

[6] Hoffman EN, Yushin G, El-Raghy T, Gogotsi Y, Barsoum MW. Micro and mesoporosity of carbon derived from ternary and binary metal carbides. Microporous and Mesoporous Materials. 2008;112(1-3):526-32.

[7] Jänes A, Thomberg T, Lust E. Synthesis and characterisation of nanoporous carbide-derived carbon by chlorination of vanadium carbide. Carbon. 2007;45(14):2717-22.

[8] Tallo I, Thomberg T, Kontturi K, Jänes A, Lust E. Nanostructured carbide-derived carbon synthesized by chlorination of tungsten carbide. Carbon. 2011;49(13):4427-33.

[9] Presser V, McDonough J, Yeon S-H, Gogotsi Y. Effect of pore size on carbon dioxide sorption by carbide derived carbon. Energy & Environmental Science. 2011;4(8):3059.

[10] Gogotsi Y, Dash RK, Yushin G, Yildirim T, Laudisio G, Fischer JE. Tailoring of Nanoscale Porosity in Carbide-Derived Carbons for Hydrogen Storage. Journal of the American Chemical Society. 2005;127(46):16006-7.

[11] Yushin G, Dash R, Jagiello J, Fischer JE, Gogotsi Y. Carbide-Derived Carbons: Effect of Pore Size on Hydrogen Uptake and Heat of Adsorption. Advanced Functional Materials. 2006;16(17):2288-93.

[12] Le Leuch LM, Bandosz TJ. The role of water and surface acidity on the reactive adsorption of ammonia on modified activated carbons. Carbon. 2007;45(3):568-78.

[13] Bandosz TJ, Petit C. On the reactive adsorption of ammonia on activated carbons modified by impregnation with inorganic compounds. Journal of Colloid and Interface Science. 2009;338(2):329-45.

[14] McCallum CL, Bandosz TJ, McGrother SC, Müller EA, Gubbins KE. A Molecular Model for Adsorption of Water on Activated Carbon: Comparison of Simulation and Experiment. Langmuir. 1999;15(2):533-44.

[15] Salame II, Bandosz TJ. Adsorption of Water and Methanol on Micro- and Mesoporous Wood-Based Activated Carbons. Langmuir. 2000;16(12):5435-40.

[16] Brennan JK, Bandosz TJ, Thomson KT, Gubbins KE. Water in porous carbons. Colloids and Surfaces A: Physicochemical and Engineering Aspects. 2001;187–188(0):539-68.

[17] Seredych M, Portet C, Gogotsi Y, Bandosz TJ. Nitrogen modified carbide-derived carbons as adsorbents of hydrogen sulfide. J Colloid Interface Sci. 2009;330(1):60-6.

[18] Hasse B, Gläsel J, Kern AM, Murzin DY, Etzold BJM. Preparation of carbide-derived carbon supported platinum catalysts. Catalysis Today. 2015;249(0):30-7.

[19] Kim HS, Singer JP, Gogotsi Y, Fischer JE. Molybdenum carbide-derived carbon for hydrogen storage. Microporous and Mesoporous Materials. 2009;120(3):267-71.

[20] Jänes A, Thomberg T, Kurig H, Lust E. Nanoscale fine-tuning of porosity of carbide-derived carbon prepared from molybdenum carbide. Carbon. 2009;47(1):23-9.

[21] Goertzen SL, Thériault KD, Oickle AM, Tarasuk AC, Andreas HA. Standardization of the Boehm titration. Part I. CO2 expulsion and endpoint determination. Carbon. 2010;48(4):1252-61.

[22] Oickle AM, Goertzen SL, Hopper KR, Abdalla YO, Andreas HA. Standardization of the Boehm titration: Part II. Method of agitation, effect of filtering and dilute titrant. Carbon. 2010;48(12):3313-22.

[23] Boehm HP. Some aspects of the surface chemistry of carbon blacks and other carbons. Carbon. 1994;32(5):759-69.

[24] Portet C, Kazachkin D, Osswald S, Gogotsi Y, Borguet E. Impact of synthesis conditions on surface chemistry and structure of carbide-derived carbons. Thermochimica Acta. 2010;497(1-2):137-42.

[25] Brunauer S, Emmett PH, Teller E. Adsorption of gases in multimolecular layers. Journal of the American Chemical Society. 1938;60:309-19.

[26] Brunauer S, Deming LS, Deming WE, Teller E. On a theory of the van der Waals adsorption of gases. Journal of the American Chemical Society. 1940;62:1723-32.

[27] Kruk M, Jaroniec M. Gas adsorption characterization of ordered organic-inorganic nanocomposite materials. Chemistry of Materials. 2001;13(10):3169-83.

[28] Thommes M, Smarsly B, Groenewolt M, Ravikovitch PI, Neimark AV. Adsorption Hysteresis of Nitrogen and Argon in Pore Networks and Characterization of Novel Micro- and Mesoporous Silicas. Langmuir. 2005;22(2):756-64.

[29] Rasmussen CJ, Vishnyakov A, Thommes M, Smarsly BM, Kleitz F, Neimark AV. Cavitation in Metastable Liquid Nitrogen Confined to Nanoscale Pores. Langmuir. 2010;26(12):10147-57.

[30] Thommes M. Physical Adsorption Characterization of Nanoporous Materials. Chemie Ingenieur Technik. 2010;82(7):1059-73.

[31] Pradhan BK, Sandle NK. Effect of different oxidizing agent treatments on the surface properties of activated carbons. Carbon. 1999;37(8):1323-32.

[32] Silverstein RM, Webster FX, Kiemle DJ. Spectrometric Indentification of Organic Compounds. 7 ed: John Wiley & Sons, Inc.; 2005.

[33] Freeman JJ. Chemistry and physics of carbon. Journal of Chemical Technology & Biotechnology. 1990;47(4):379-80.

[34] Shen. Surface Chemical Functional Groups Modification of Porous Carbon. Recent Patent on Chemical Engineering. 2008;1:27-40.

[35] Desimoni E, Casella GI, Cataldi TRI, Salvi AM, Rotunno T, Di Croce E. Remarks on the surface characterization of carbon fibres. Surface and Interface Analysis. 1992;18(8):623-30.

[36] Miller FA, Wilkins CH. Infrared Spectra and Characteristic Frequencies of Inorganic Ions. Analytical Chemistry. 1952;24(8):1253-94.

[37] Seredych M, Bandosz TJ. Mechanism of Ammonia Retention on Graphite Oxides: Role of Surface Chemistry and Structure†. The Journal of Physical Chemistry C. 2007;111(43):15596-604.

.

CHAPTER 6

SUMMARY AND FUTURE DIRECTIONS

6.1 Summary

The fundamental goal of this work was to provide the tools and methods necessary to include well-dispersed chemical specific active sites in CDCs. To accomplish this goal, this work investigated novel methods to include metal nanoparticles within CDCs to increase sorbate-sorbent interactions. In **Chapter 3**, it was shown through incomplete extraction, a large percentage of the metal from the carbide precursor can be retained in a resulting CDC as a well-dispersed and tunable active site.

In Chapter 4, the physical properties of CDCs with tunable metal sites were determined. Design rules were provided to allow for tunability of the pore size and bulk porosity in addition to the chemical properties of the residual metal. In addition, the activity of residual $FeCl_3$ nanoparticles was established through a series of ammonia adsorption experiments. From the results, it was concluded that embedded metal nanoparticles within carbide-derived carbons can be effective adsorptive sites for small gases.

In **Chapter 5**, the addition of functional groups to enhance interactions with ammonia was investigated. The high bulk porosity of CDCs is ideal for dispersed acidic functional groups to provide acid-base interactions with ammonia, and the tunable pore size inherent to CDCs allowed for investigation of the ideal pore architecture for optimal activity of these acid sites. It was suggested from the results of acid-treated Mo_2C-CDCs,

that an ammonia adsorbent should feature a high amount of micropores and small mesopores for most efficient use of acidic functional groups.

The applied goal for this research project was to attain a 6.9 mmol g^{-1} dynamic loading of NH_3 under dry and wet conditions, representing a ten-fold increase over current defense industry standard materials. The maximum performance of designed Mo_2C-CDC adsorbents was attained in **Chapter 5**, with M-500C-S-N achieving a dynamic loading of 4.95 mmol g^{-1} and 6.01 mmol g^{-1} under dry and wet conditions. However, these breakthrough capacities were calculated initial breakthrough, when the sensor registers $[NH_3] > 0$ ppm. In contrast, the target loading is a saturated loading, and includes the amount of ammonia adsorbed until the sensor reaches the inlet concentration of $[NH_3] = \sim 1500$ ppm. Through integration of the adsorbed amount of NH_3 from 0 to 500 ppm on the breakthrough curve, M-500C-S-N was estimated to have a dynamic capacity of 7.10 mmol g^{-1} and 6.81 mmol g^{-1} when under dry and wet conditions at $[NH_3] = 500$ ppm. This represents a drastic increase over the industry standard, and almost certainly reaches the goal of a saturated loading of 6.9 mmol g^{-1} when calculated until saturation.

Fundamentally, this work has developed novel and facile methods for the inclusion of chemical specific active sites in carbide-derived carbons. These results serve to further the fundamental understanding of the metal extraction process and the surface modification of CDCs. In addition, the use of relatively inexpensive carbide precursors (<\$1 per kg for Fe_3C and Mo_2C) make the materials developed within this research project viable on the commercial scale.

6.2 Future Directions

The scale up of the current carbide-derived carbon synthesis is of utmost importance for future studies. Scale-up would save valuable synthesis and characterization time and permit material characterization methods that require greater amounts of sample. There are two limitations with the current setup. Metal chloride products with high boiling points (> 300^{o}C) easily solidifies directly after exiting the tube furnace. Typically, the metal chloride does not settle at the bottom of the quartz tube, but grows radially from all sides of the quartz to the center. At too high of a batch size or too fast of a chlorination rate, back pressure can result. Consequently, experimental runs have been ran at small batch sizes (typically 1 gram), and low concentrations of chlorine (20% v/v) to ensure safe operation. Depending on the carbide precursor, 1 gram of carbide typically results in only 50-100 mg of CDC, contingent on the amount of residual metal and the mass percentage of carbon present in the carbide.

To mitigate these effects, a new vertical flow packed bed reactor design has been proposed, utilizing a quartz frit to hold carbide precursor in place and a quartz bulb on the outlet of the reactor to collect metal chloride products. During operation, downward flow would carry volatile metal chloride to the bottom outlet of the reactor. Solidification outside of the reactor would cause a large percentage of the by-products to fall into the quartz bulb, while a side outlet would carry flow through a NaOH scrubber to neutralize any unreacted chlorine gas. The larger diameter of the quartz tube, 2”, would also allow for large amounts of carbide precursor to be loaded on the quartz frit at relatively small bed sizes. This would limit axially differences in conversion, which should be avoided when synthesizing CDCs with retained metal sites. Increased batch sizes would allow the

use of several new characterization techniques. Titration methods such as potentiometric titration and Boehm titration could be employed. Increased sample size is also necessary to crush and sieve samples to standardize particle size for dynamic breakthrough experiments.

Fundamental studies on Fe_3C-CDC should continue after the construction of this reactor. Reaction conditions where a combination of $FeCl_2$ and $FeCl_3$ nanostructures and nanoparticles are observed, could be further purified and studied in the absence of the diffusional limitations of a quartz boat and tube reactor setup. In addition, studies on the dispersion and form of the residual Fe in Fe_3C-CDCs at other chlorination temperatures could be better carried out without the fear of convoluted multiple phases due to these mass transfer limitations.

It is highly likely that other metal carbides are able to form embedded metal nanoparticles in their respectively CDCs. Other candidates that should be investigated are metals that can act as graphitization catalysts with relatively low melting and boiling points to result in the partial removal of the metal chloride. Initial investigations into the chlorination of Co_2C, seen in **Appendix C**, suggest retention of Co nanoparticles is also possible within Co_2C-CDCs, but there is a large trade-off between successful partial removal of $CoCl_2$ to increase porosity and excessive graphitization that decreases internal porosity. At high enough temperatures to vaporize the $CoCl_2$, there can be extreme organization of the CDC. This leads to relatively non-porous highly ordered graphite. This may have interesting uses if there are intercalated Co species present, but from an adsorption standpoint the absence of accessible surface area severely limits the utility of these CDCs.

Appendix A

EMBEDDED IRON NANOPARTICLES IN FE3C-DERIVED CARBONS

Parts of this chapter are adapted from Mangarella, M.C., Ewbank, J.L., Dutzer, M.R., Alamgir, F.M., and Walton, K.S. (2014). Synthesis of Embedded Iron Nanoparticles in Fe3C-derived Carbons. Carbon 79, 74-84.

A.1 Residual Metal in Fe_3C-derived carbons

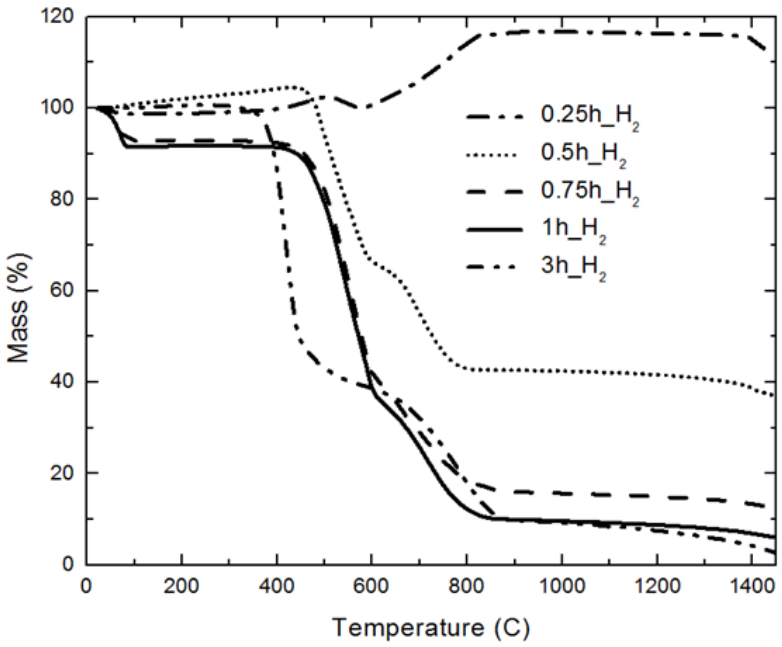

Figure A.1. TGA Profiles of Annealed Fe_3C-CDCs

Table A.1 – Residual Metal Content of Annealed Fe_3C-CDC Samples

Chlorination Time (h)	**Residual Mass at 1450°C (%)**	**Residual Fe assuming conversion to Fe_2O_3 (%)**
0	**N/A**	**93**
0.25	**111**	**77.3**
0.5	**36.6**	**25.5**
0.75	**12.0**	**8.4**
1	**5.8**	**4.0**
1.5	**4.0**	**2.7**
3	**1.2**	**0.8**

Table A.2 – Relative Portion of Top and Bottom Layers

Sample Name	Relative Mass Percent (%)
0.25h-top	12.4
0.25h-bot	87.6
0.5h-top	51.9
0.5h-bot	48.1

A.2 Supporting SEM Images for Fe_3C-derived Carbons

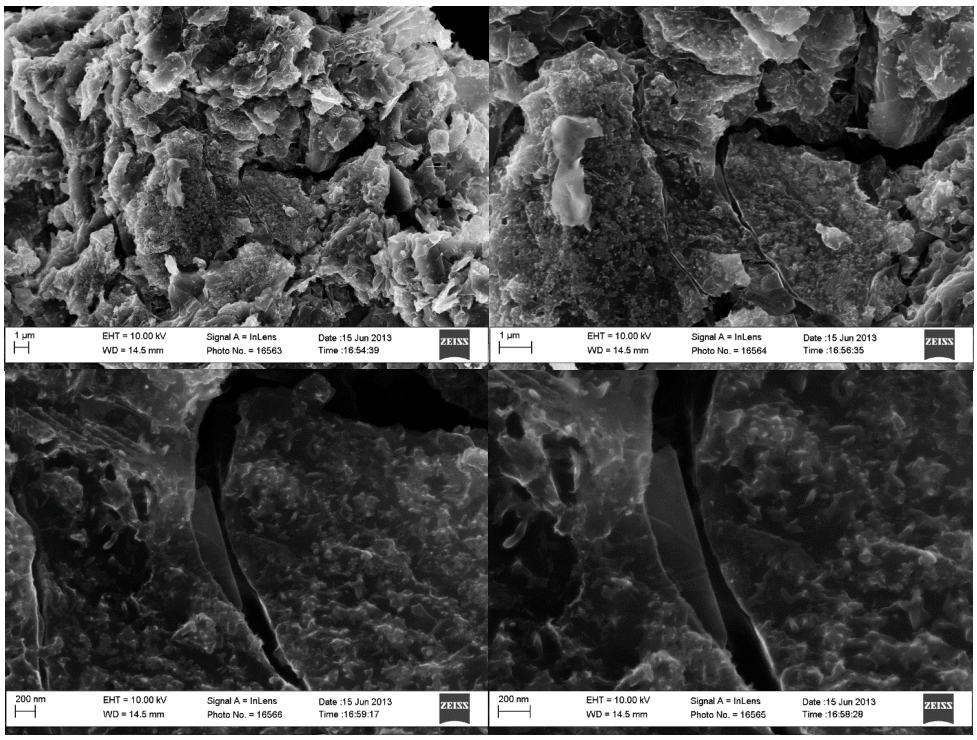

Figure A.2. SEM Images of 0.25h-top

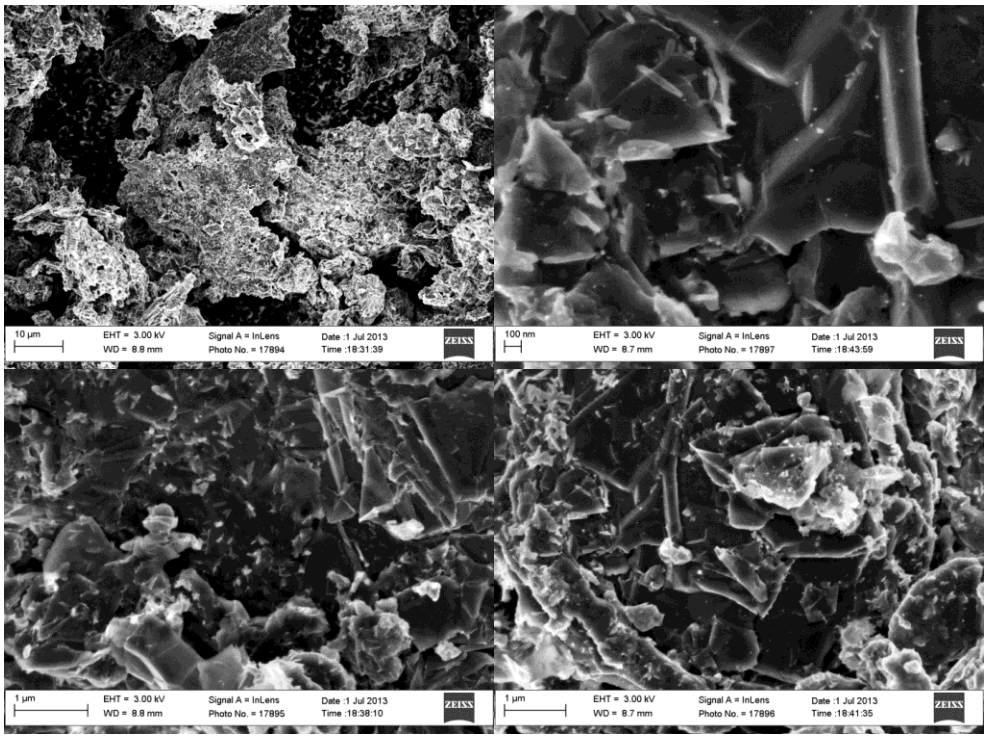

Figure A.3. SEM Images of 0.25h-top at 3kV

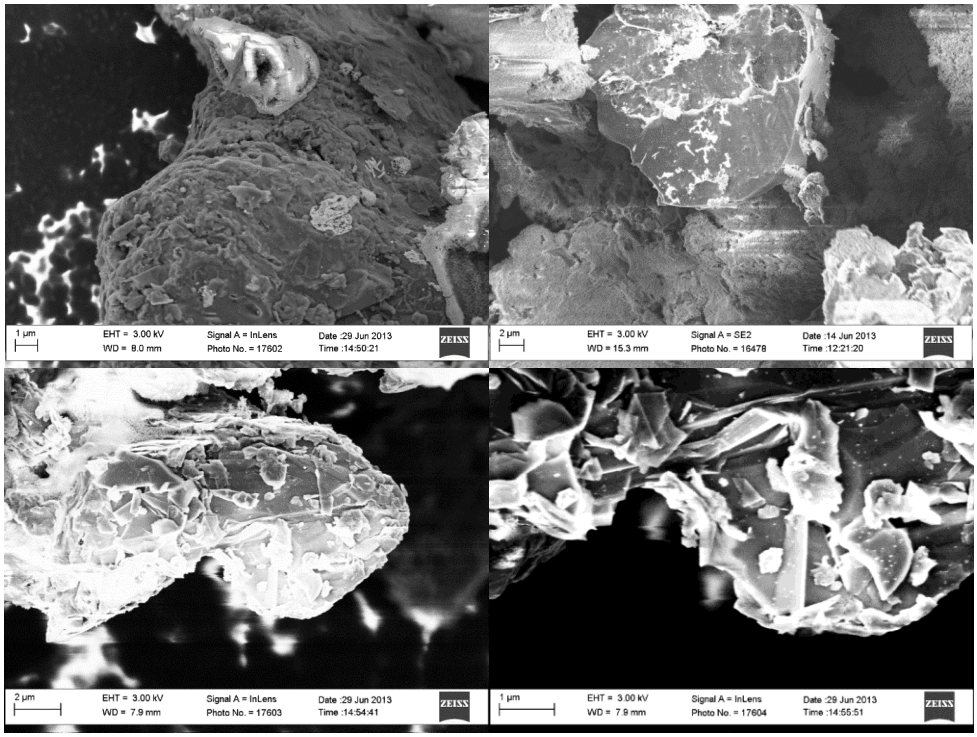

Figure A.4. SEM Images of 0.25h-bot at 3kV

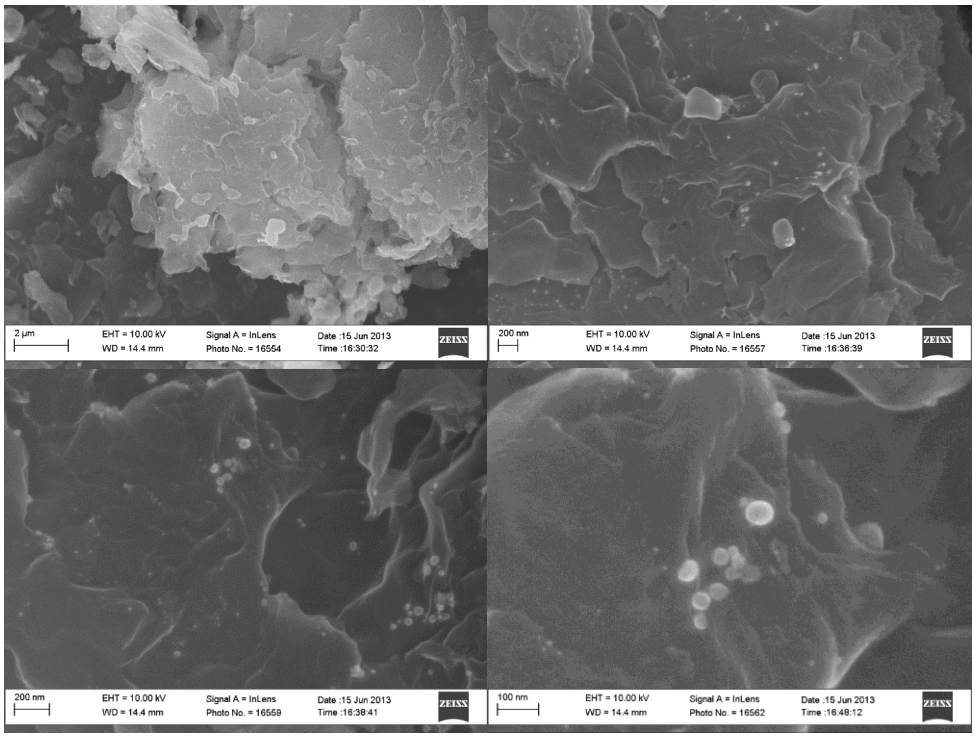

Figure A.5. SEM Images of 0.25h-H_2

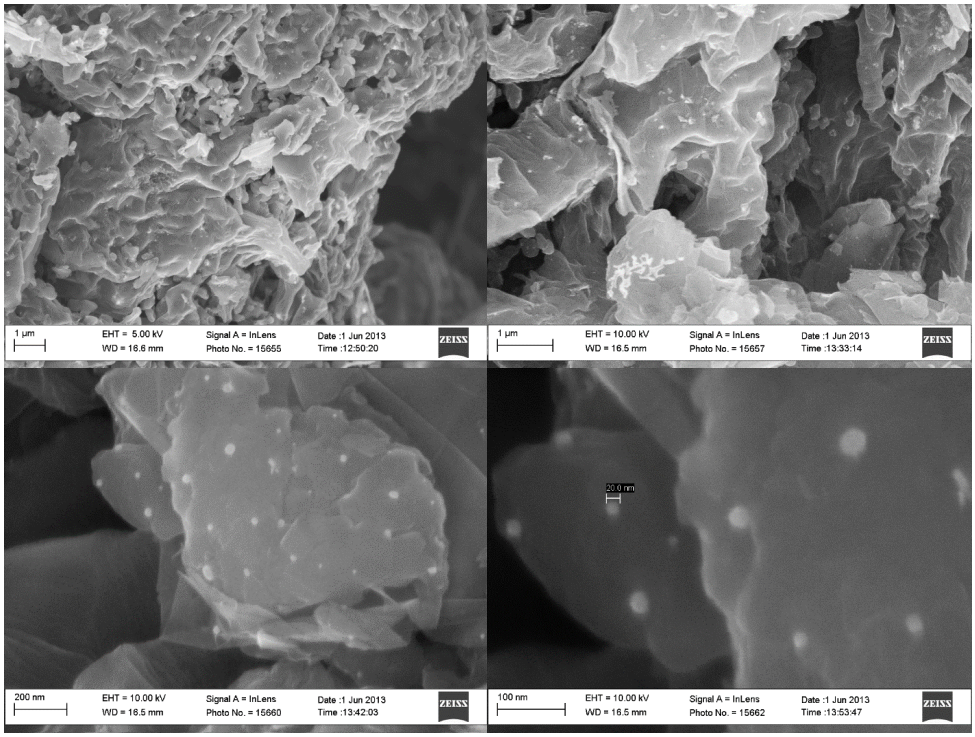

Figure A.6. SEM Images of 0.5h-top

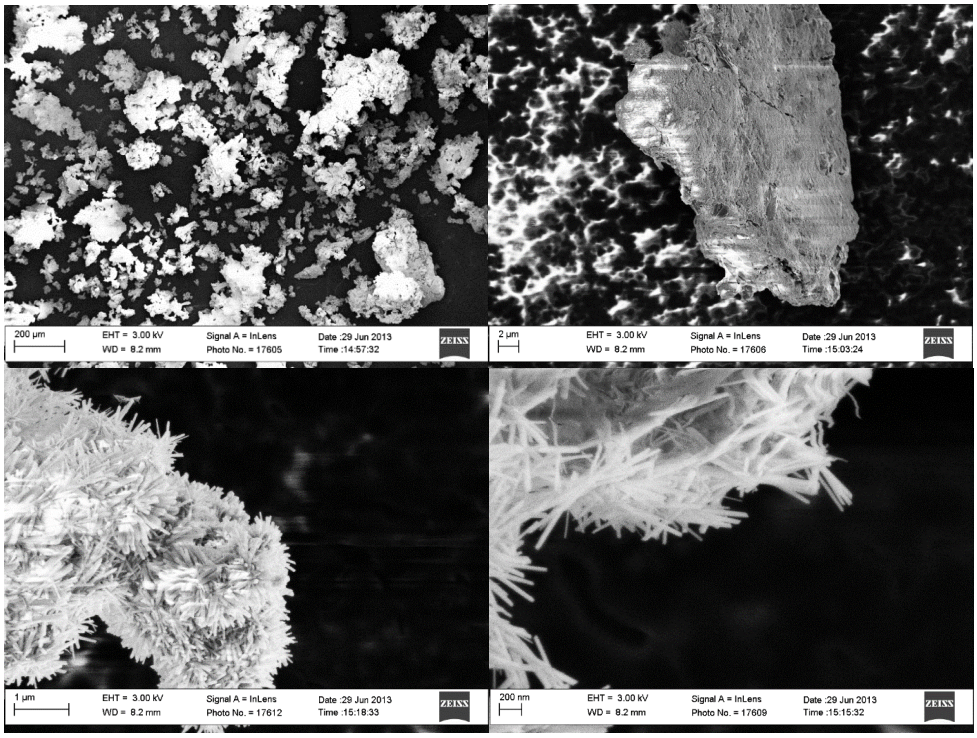

Figure A.7. SEM Images of 0.5h-bot

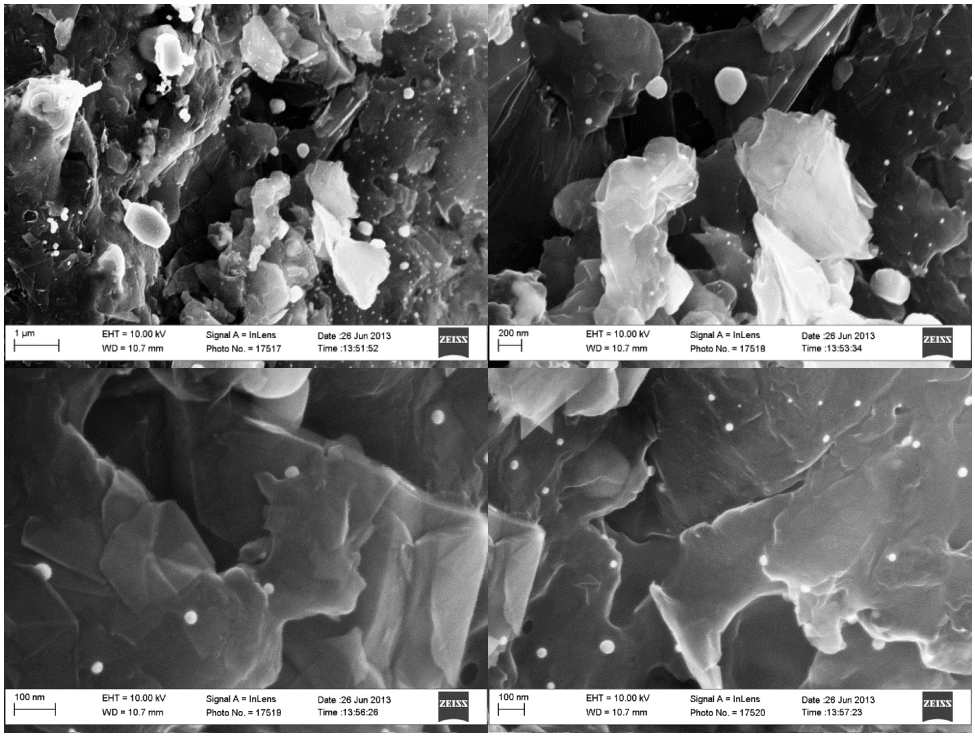

Figure A.8. SEM Images of 0.25h-H_2

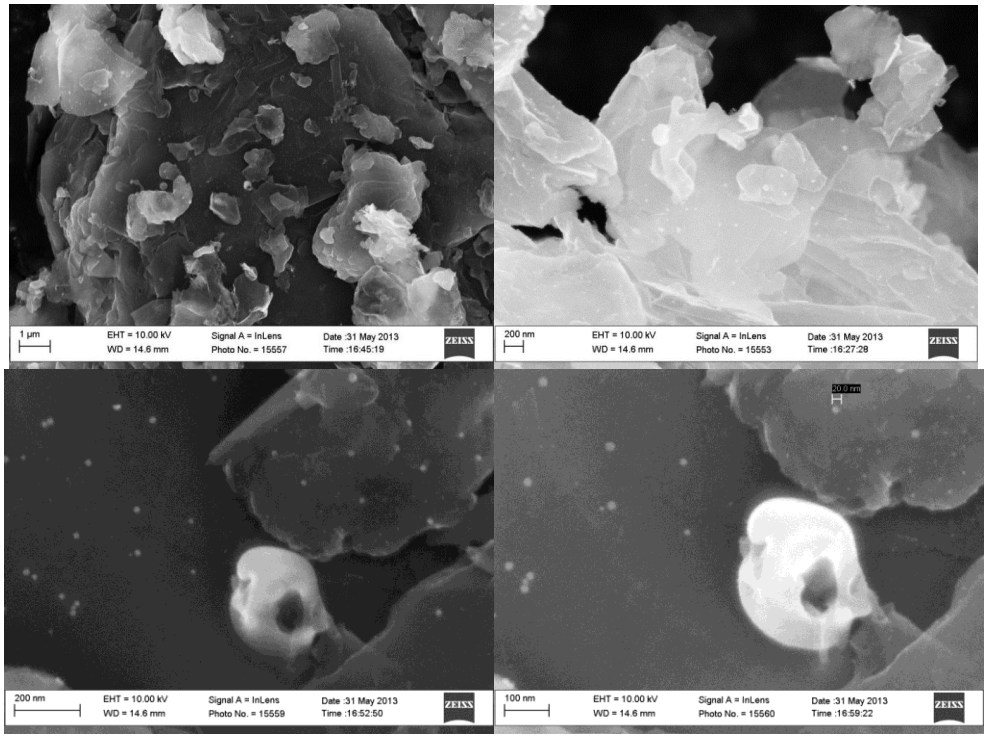

Figure A.9. SEM Images of 0.75h

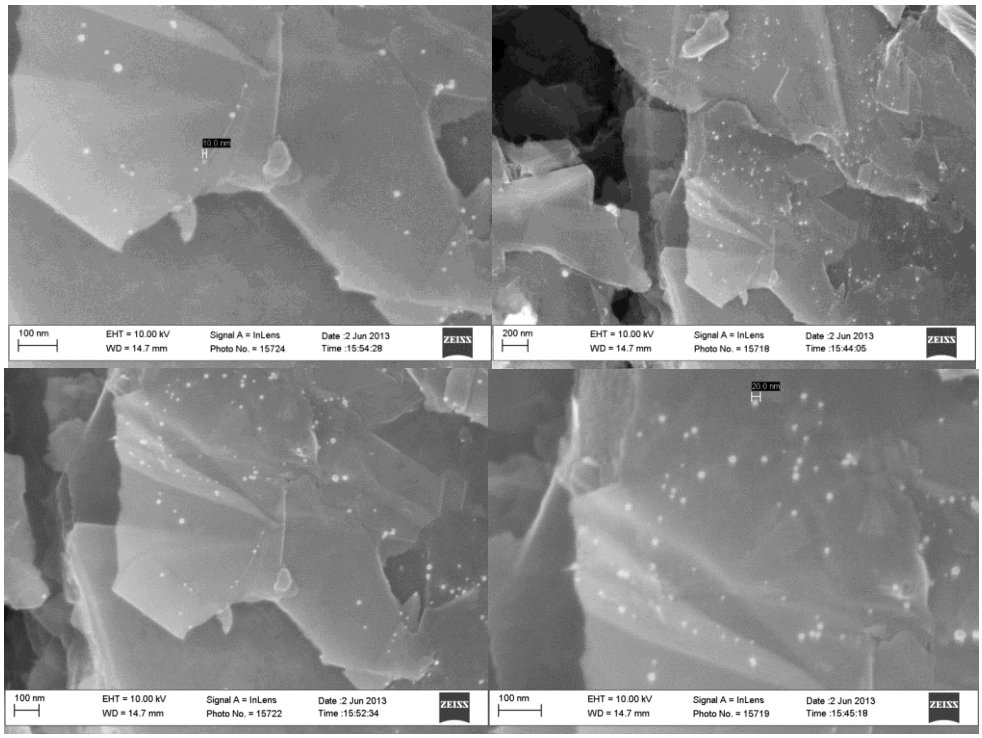

Figure A.10. SEM Images of 0.75h-H_2

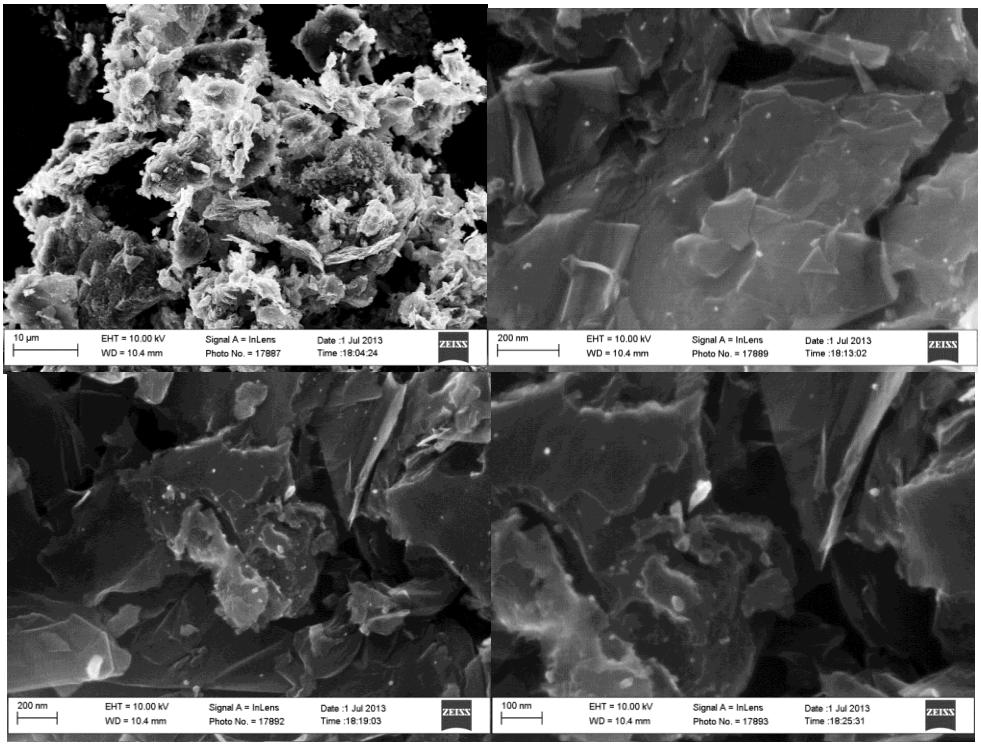

Figure A.11. SEM Images of 1.0h

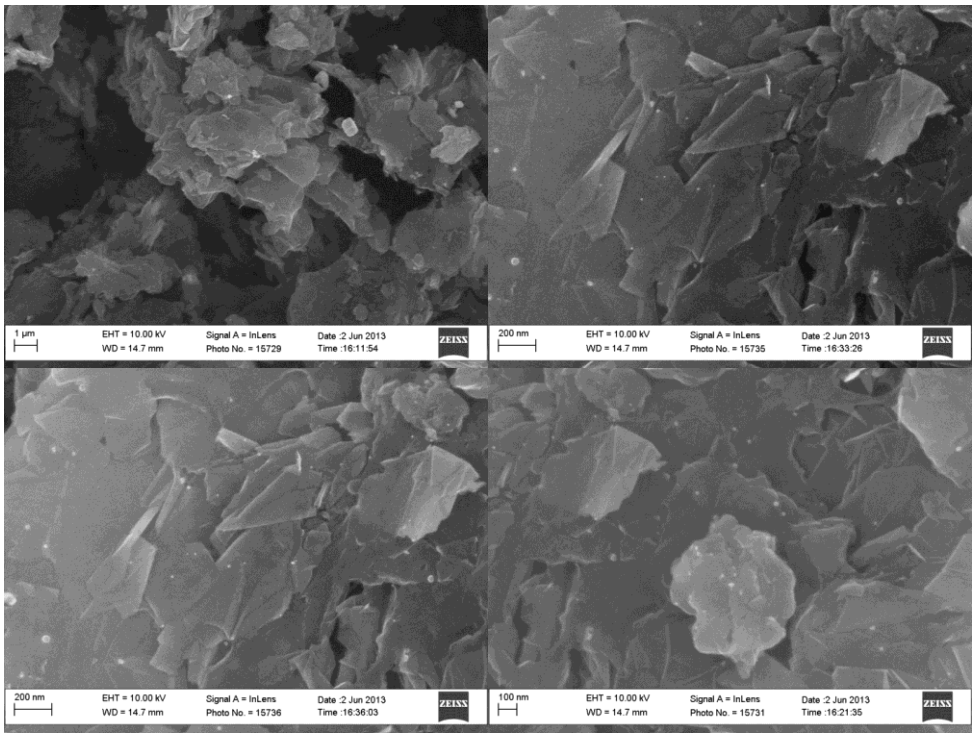

Figure A.12. SEM Images of 1.0h-H_2

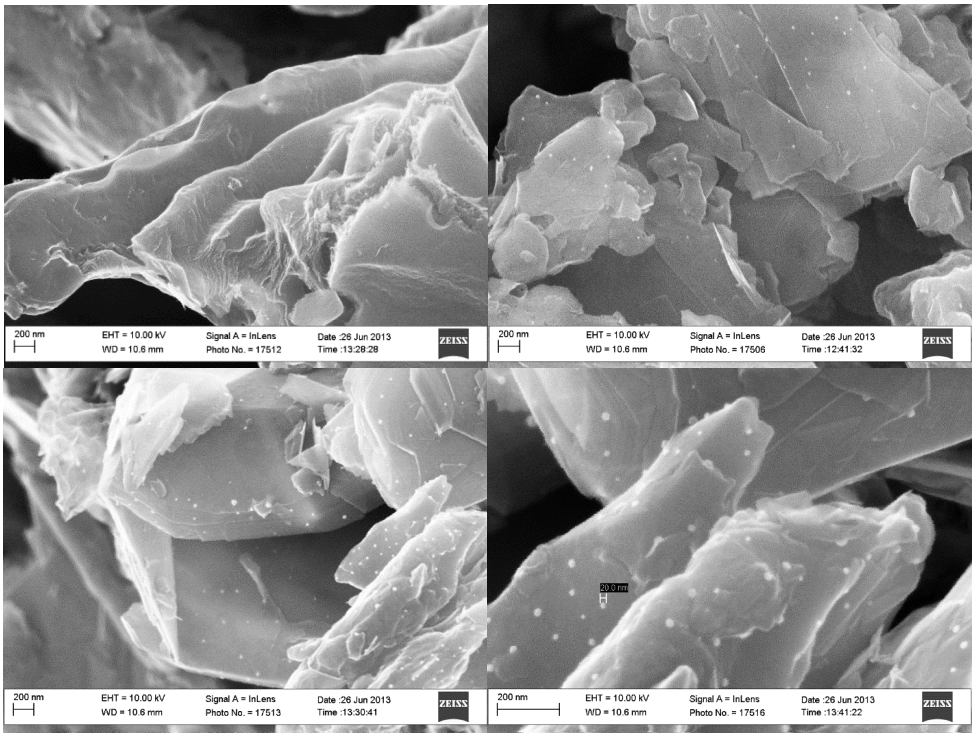

Figure A.13. SEM Images of 1.5h

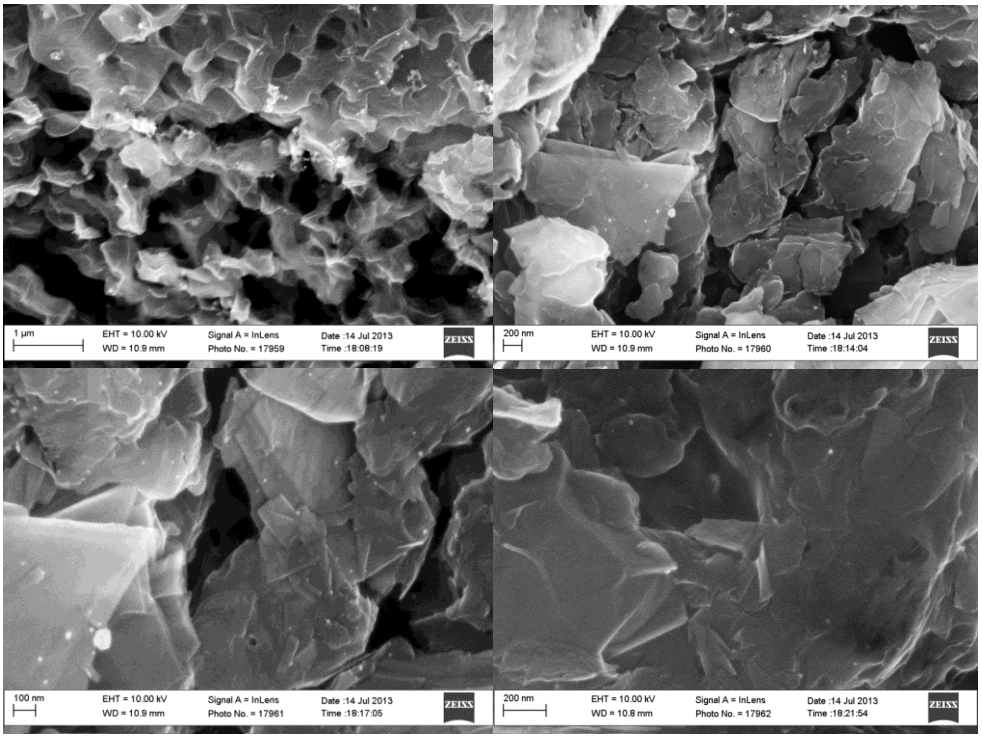

Figure A.14. SEM Images of 1.5h-H_2

Appendix B

EMBEDDED FE NANOPARTICLES IN FE3C-DERIVED CARBONS

B.1 Residual Metal in Annealed Fe_3C-derived Carbons

Metal removal was determined gravimetrically according to Equation (B.1):

$$X_{Fe_3C} = \frac{m_0 - m_f}{m_0} \frac{M_{Fe_3C}}{M_{Fe}} \quad \text{(B.1)}$$

Table B.1. Metal Removal for Annealed Fe3C-CDCs

Sample Name	Percent Metal Removed (%)[a]
Fe_3C	-
Fe_3C-CDC-200C-2h-H_2	73.6
Fe_3C-CDC-300C-2h-H_2	94.9
Fe_3C-CDC-400C-2h-H_2	95.5
Fe_3C-CDC-500C-2h-H_2	95.0

a) Calculated by Eq. (1)

B.2 Pore size distributions of annealed and unannealed Fe3C-CDCs

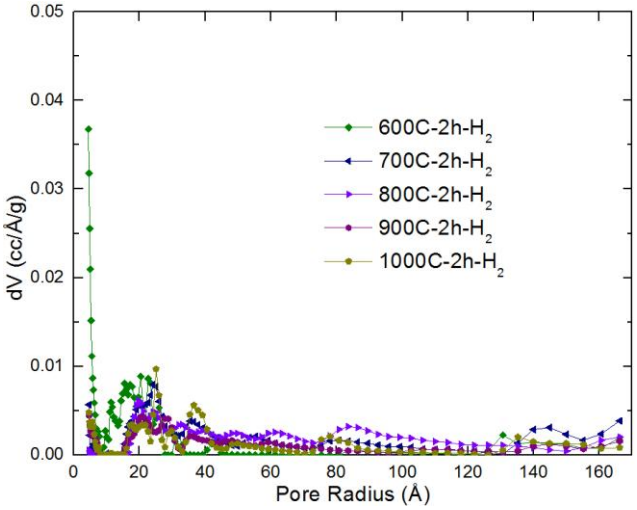

Figure B.1. Full Scale Pore Size Distributions for Fe_3C-CDCs Prepared at High Chlorination Temperatures

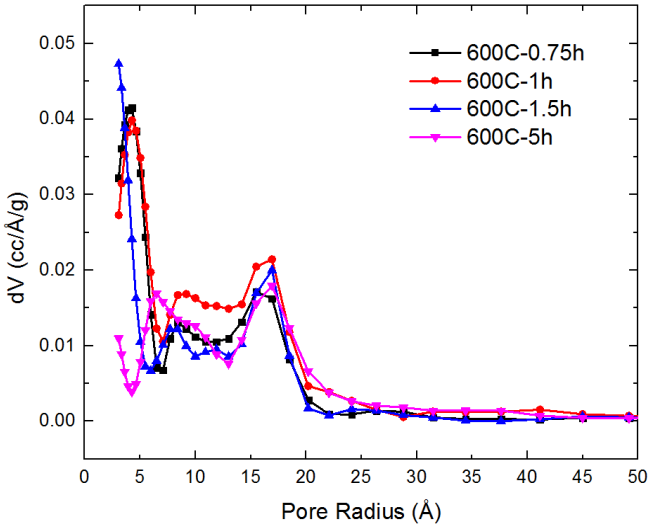

Figure B.2. Full Scale Pore Size Distributions for Unnannealed Fe_3C-CDCs

B.3 Supporting SEM Images for Annealed Fe3C-derived Carbons

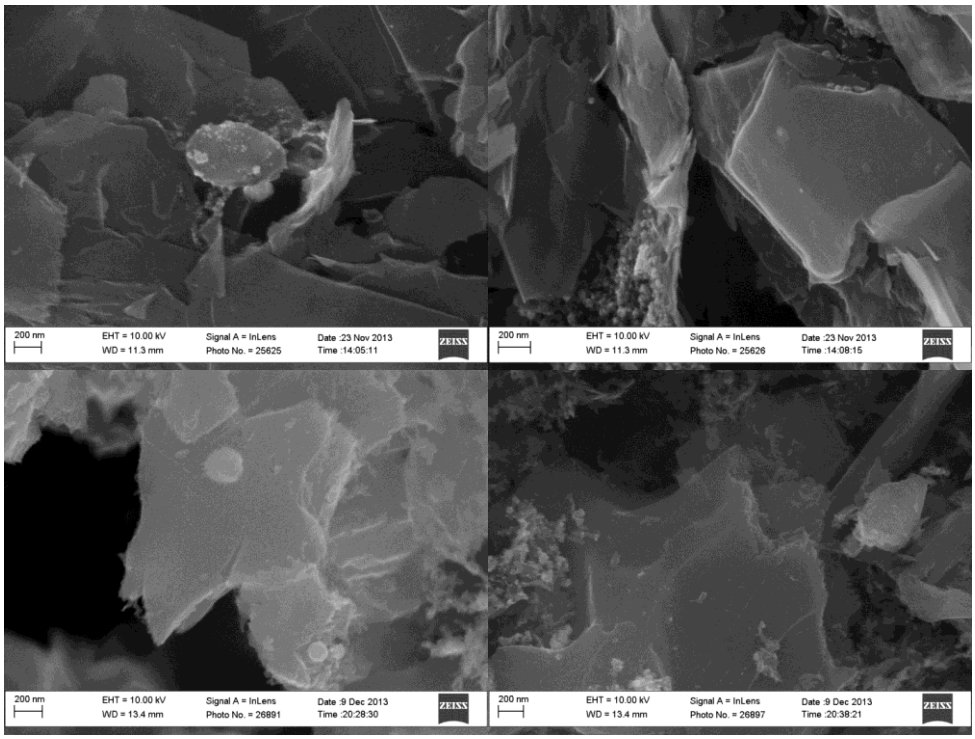

Figure B.3. SEM Images of 300C-2h-H_2

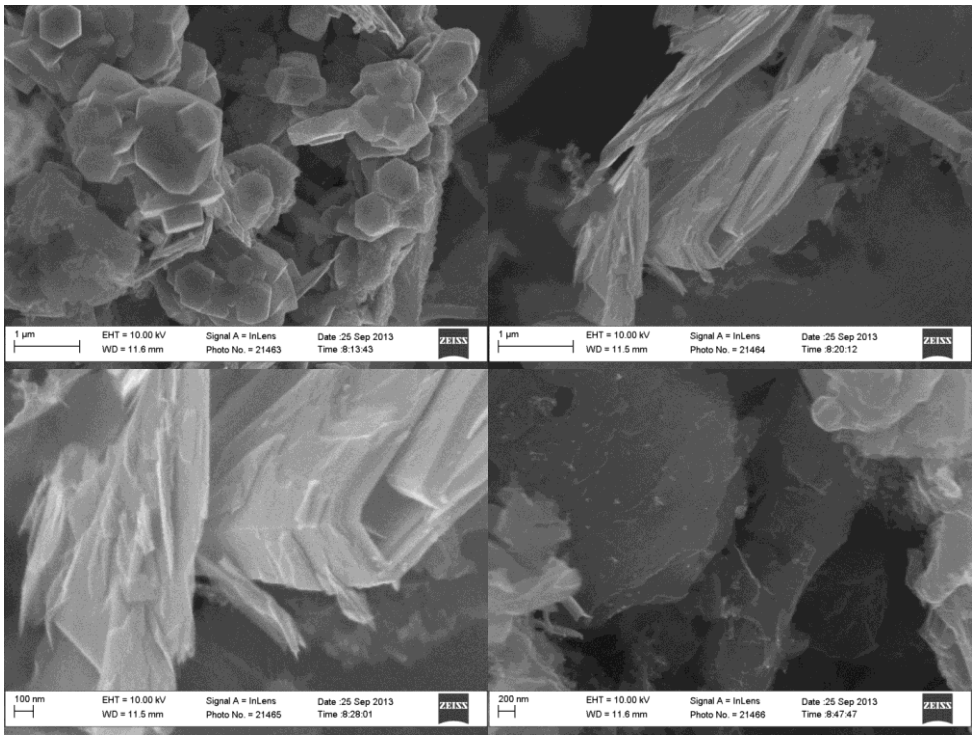

Figure B.4. SEM Images of 400C-2h-H_2

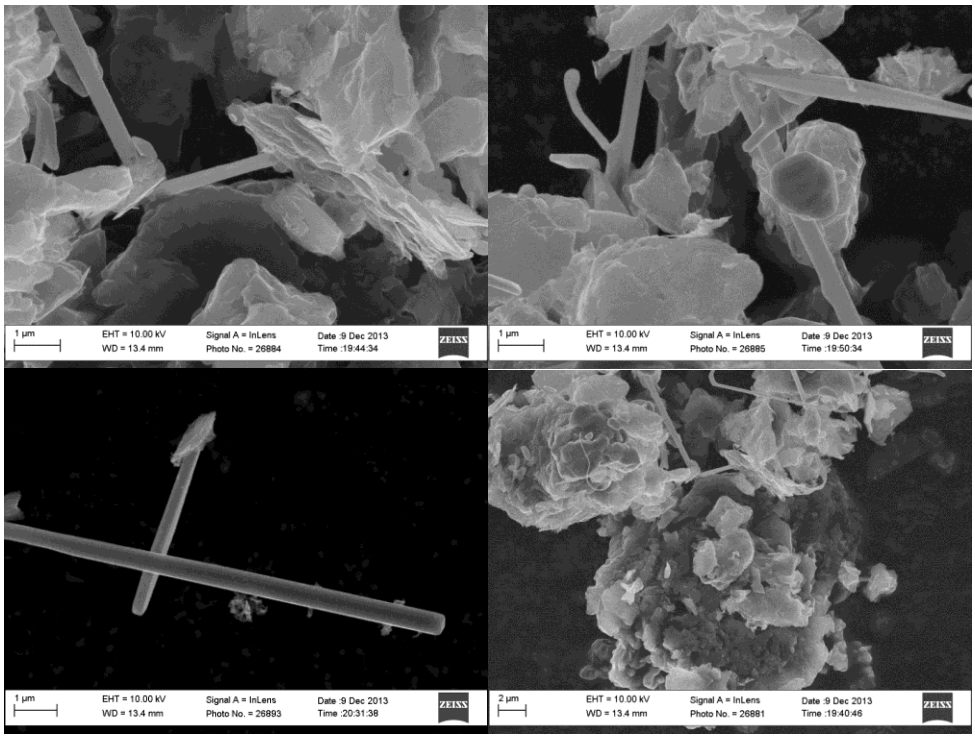

Figure B.5. SEM Images of 500C-2h-H_2

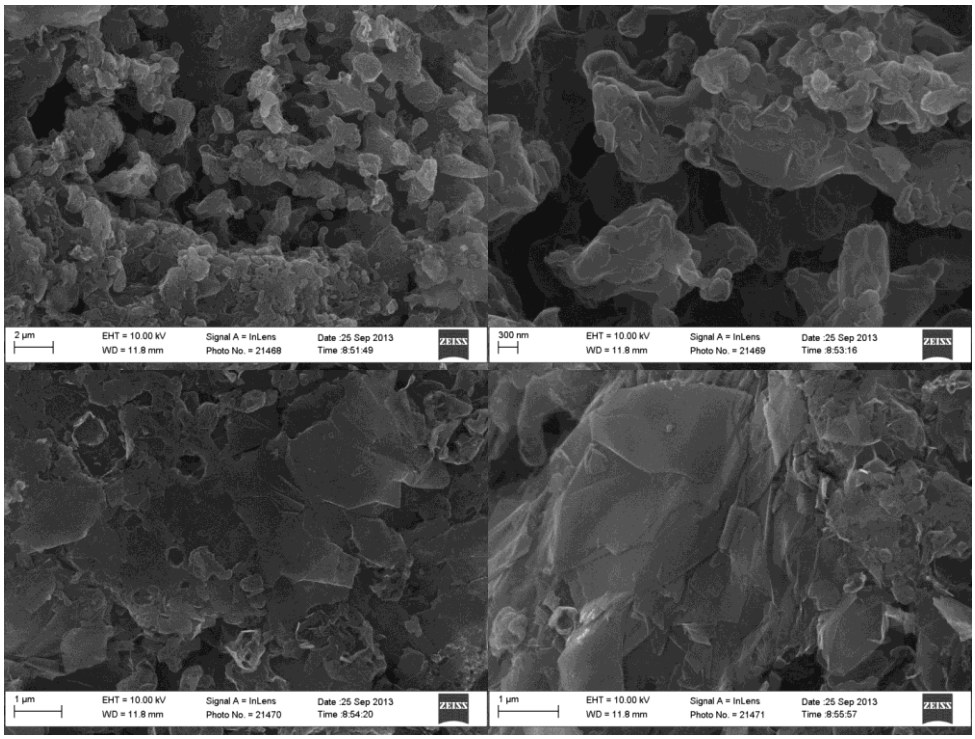

Figure B.6. SEM Images of 800C-2h-H_2

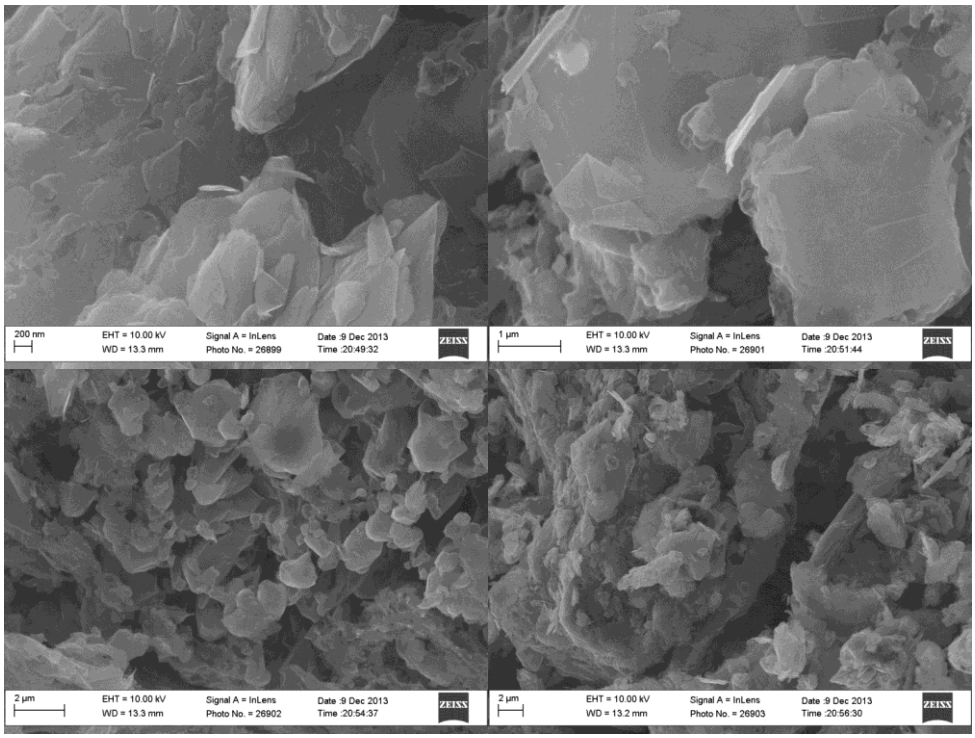

Figure B.7. SEM Images of 1000C-2h-H_2

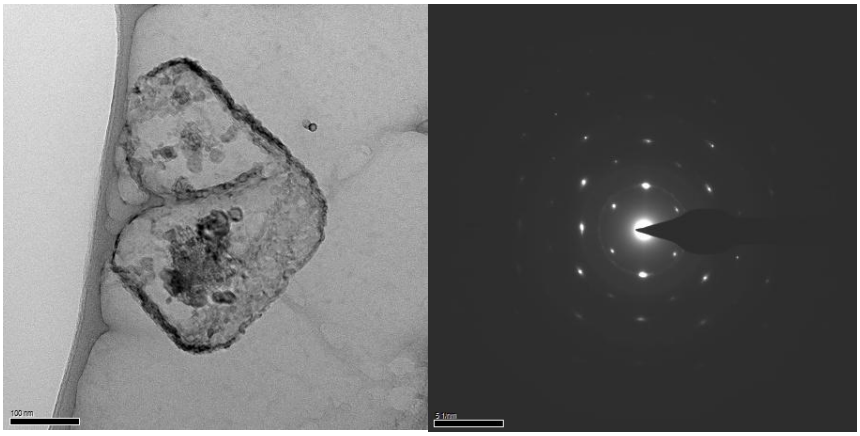

Figure B.8. HRTEM, and Diffraction Patterns of 200C-2h-H_2

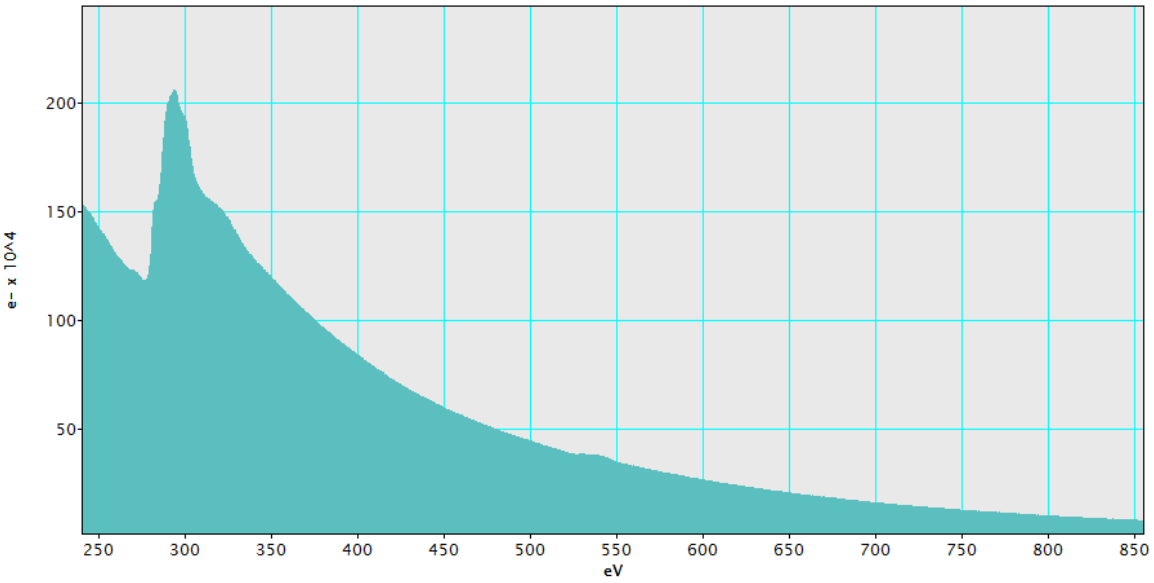

Figure B.9. EELS Spectra of 200C-2h-H_2

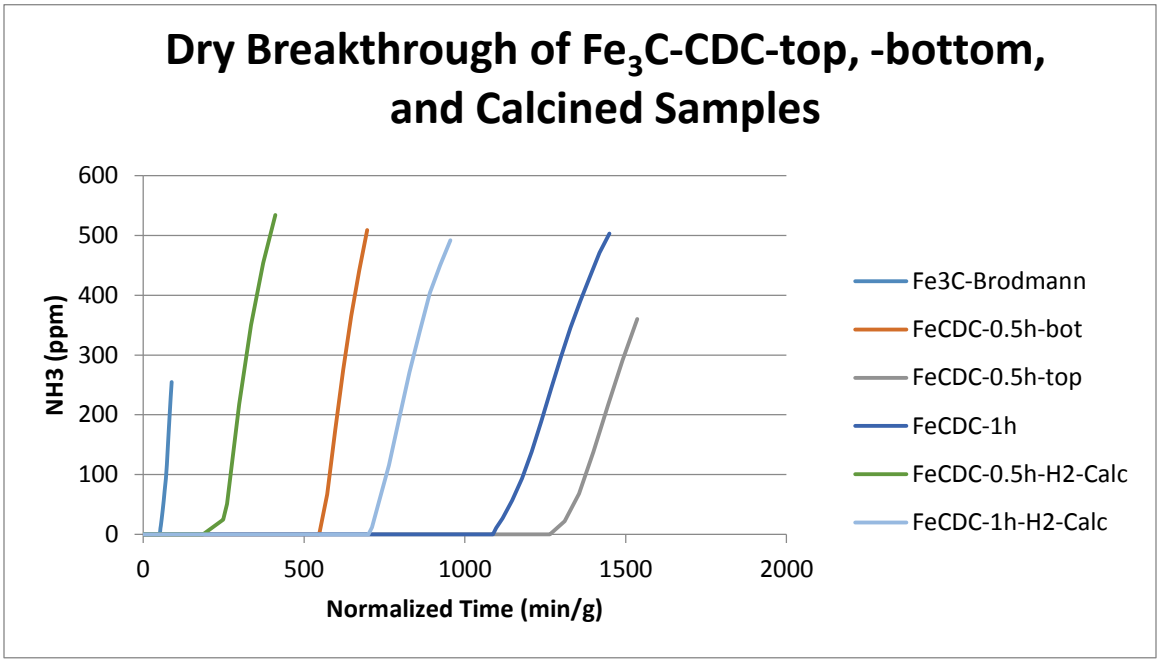

Figure B.10. Dry Breakthrough screening of Fe_3C-CDCs with $FeCl_2$, $FeCl_3$, and Fe_2O_3 active sites in a horizontal bed setup

Appendix C

SYNTHESIZED CO2C-DERIVED CARBONS

A series of Co_2C-CDCs were synthesized from a Co_2C precursor (99.9% American Elements). Synthesized Co_2C-CDCs at high temperature (1000^oC) are seen to be highly graphitized in XRD and have evidence of Co nanoparticles present in SEM. N_2 sorption experiments show remarkably low specific surface area (<20 m^2 g^{-1}), suggesting that high temperature samples consist of relatively non-porous graphite.

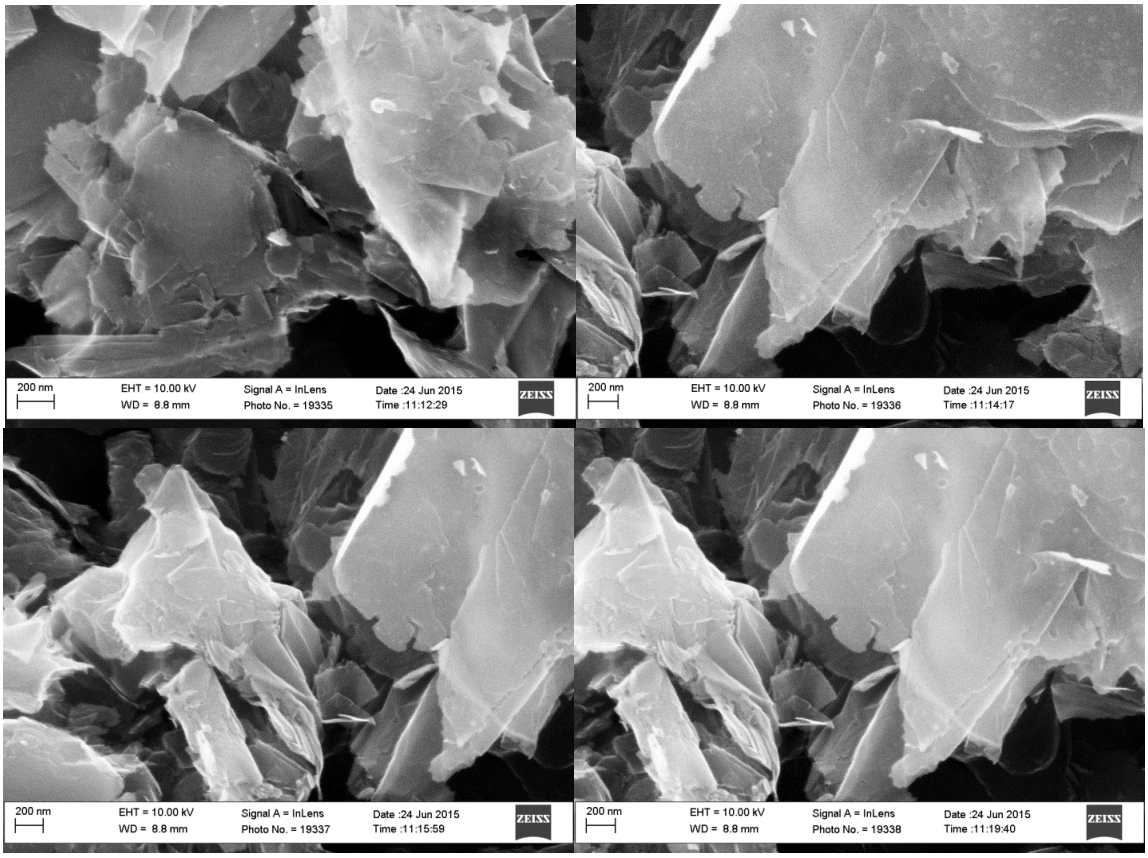

Figure C.1 – SEM Images of Co_2C-CDC-1000C-1h

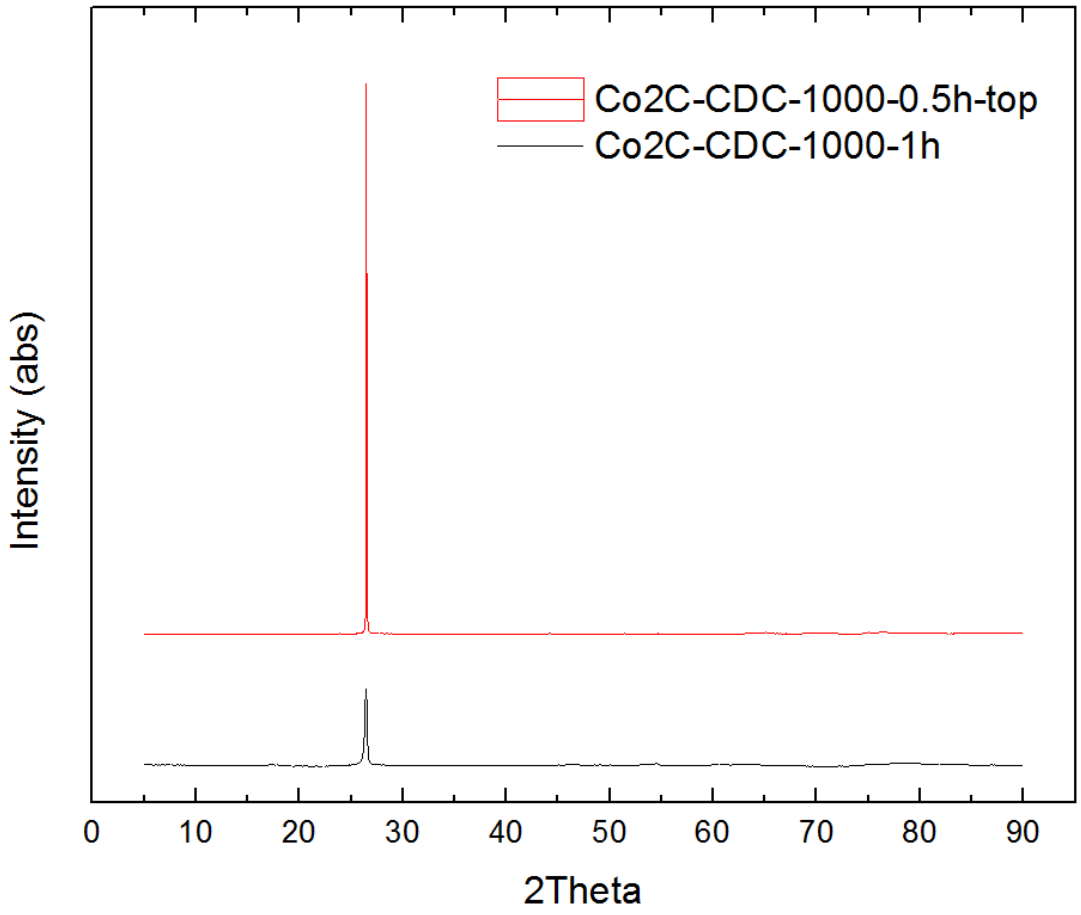

Figure C.2 – XRD of unannealed Co_2C-CDCs